

AD-A099 993

HUGHES RESEARCH LABS MALIBU CA

F/G 20/12

INP BY PLANAR REACTIVE DEPOSITION AND GAAS BY LOW PRESSURE META--ETC(U)

FEB 81 K ZANIO

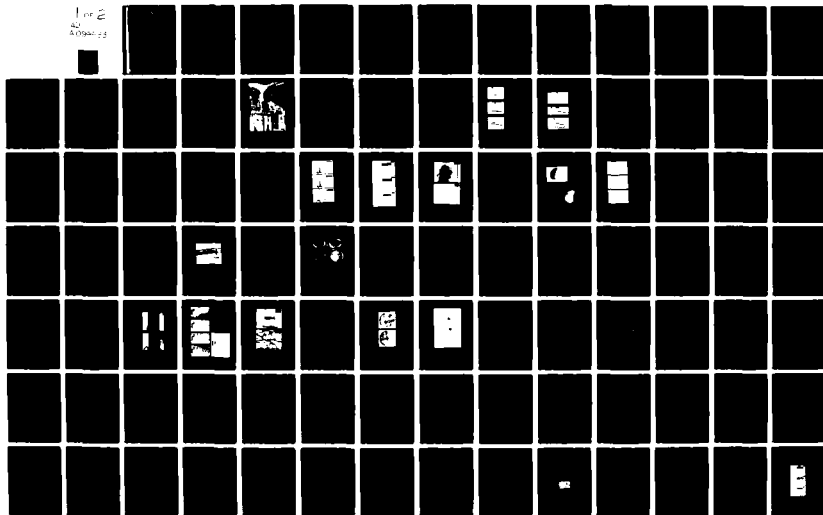
F44620-76-C-0133

UNCLASSIFIED

AFOSR-TR-81-0474

NL

1 of 2
42
A0999 993



LEVEL

12

AD A099993

**InP BY PLANAR REACTIVE DEPOSITION
AND GaAs BY LOW PRESSURE METAL
ORGANIC CHEMICAL VAPOR DEPOSITION**

K. Zanio

Hughes Research Laboratories
3011 Malibu Canyon Road
Malibu, CA 90265

February 1981

F44620-76-C-0133

Final Scientific Report

For period 1 June 1976 through 31 November 1980

Approved for public release; distribution unlimited.

DTIC
ELECTED
JUN 10 1981
C

AIR FORCE OFFICE OF SCIENTIFIC RESEARCH

Building 410
Bolling AFB, D.C. 20332

DTIC FILE COPY

Research sponsored by the Air Force Office of Scientific Research (AFSC). United States Air Force, under Contract F44620-76-C-0133. The United States Government is authorized to reproduce and distribute reprints for governmental purposes notwithstanding any copyright notation hereon.

UNCLASSIFIED

SECURITY CLASSIFICATION OF THIS PAGE (When Data Entered)

18 REPORT DOCUMENTATION PAGE		READ INSTRUCTIONS BEFORE COMPLETING FORM	
1. REPORT NUMBER AFOSR TR-81-0474	2. GOVT ACCESSION NO. AD-A099993	3. RECIPIENT'S CATALOG NUMBER (9)	
4. TITLE (and Subtitle) InP BY PLANAR REACTIVE DEPOSITION AND GaAs BY LOW PRESSURE METAL ORGANIC CHEMICAL VAPOR DEPOSITION.		5. DATE OF REPORT & PERIOD COVERED Final report 1 Jun 1976-30 Nov 1980	
6. AUTHOR(s) K./Zanio		7. CONTRACT OR GRANT NUMBER(s) F44620-76-C-0133	
8. PERFORMING ORGANIZATION NAME AND ADDRESS Hughes Research Laboratories 3011 Malibu Canyon Road Malibu, California 90265		9. PROGRAM ELEMENT, PROJECT, TASK AREA & WORK UNIT NUMBERS 6110296 2306/B1	
10. CONTROLLING OFFICE NAME AND ADDRESS Air Force Office of Scientific Research Building 410 Bolling AFB, D.C. 20332		11. REPORT DATE February 1981	
12. MONITORING AGENCY NAME & ADDRESS (if different from Controlling Office) 12147		13. NUMBER OF PAGES 159	
		14. SECURITY CLASS. (of this report) UNCLASSIFIED	
15. DISTRIBUTION STATEMENT (of this Report) Approved for public release; distribution unlimited.		16. DECLASSIFICATION DOWNGRADING SCHEDULE	
17. DISTRIBUTION STATEMENT (of the abstract entered in Block 20, if different from Report)			
18. SUPPLEMENTARY NOTES			
19. KEY WORDS (Continue on reverse side if necessary and identify by block number) Indium phosphide, InGaAsP, Microwave devices, Gallium arsenide, Molecular beam epitaxy, InGaAs, Low-pressure CVD, InGaP, Metal organic CVD,			
20. ABSTRACT (Continue on reverse side if necessary and identify by block number) The planar reactive deposition (PRD) technique was developed to grow InP thin films by vacuum evaporation in a H₂ reactive atmosphere. InP films with room temperature mobilities as high as 4062 cm²/Vsec and carrier concentrations (N_D-N_A) as low as 10¹⁶ cm⁻³ were grown on (100) semi-insulating substrates. N⁺ films with carrier concentration of a few times 10¹⁹ cm⁻³ were obtained using Sn doping. N⁺/N/N⁺ multi-layer structures, and large area (10 cm) epitaxial films were grown on			

DD FORM 1 JAN 73 1473 EDITION OF 1 NOV 65 IS OBSOLETE

UNCLASSIFIED

SECURITY CLASSIFICATION OF THIS PAGE (When Data Entered)

UNCLASSIFIED

SECURITY CLASSIFICATION OF THIS PAGE (When Data Entered)

InP substrates. Epitaxial films of InGaAs, InGaP and InGaAsP were grown by PRD, and lattice matched to InP and GaAs substrates. As an intermediate step to grow InP by low pressure metal organic chemical vapor deposition (LPMOCVD), GaAs was grown by LPMOCVD. Unintentionally doped p-type GaAs, with hole concentration as high as a few times 10^{20} cm^{-3} , was grown at the Ga-rich three-phase boundary. By undertaking growth away from the boundary, the hole concentration decreased, and ionized impurity concentrations ($N_A + N_D$) as low as 10^{16} cm^{-3} were obtained. Major background impurities for growth of InP by PRD and GaAs by LPMOCVD are carbon and oxygen. Growth of InP in a halide environment is recommended to obtain higher purity InP thin films by low cost vacuum technologies.

Accession For	
NTIS GRA&I	<input checked="checked" type="checkbox"/>
DTIC TAB	<input type="checkbox"/>
Unannounced	<input type="checkbox"/>
Justification	
By	
Distribution/	
Availability Codes	
Dist	Avail and/or Special

UNCLASSIFIED

SECURITY CLASSIFICATION OF THIS PAGE (When Data Entered)

FOREWORD

This report was prepared by Dr. Kenneth Zanio of Hughes Research Laboratories (Malibu) for the Air Force Office of Scientific Research under Contract F44620-76-C-0133. The contracting officer is Dr. Cole Litton at Wright-Patterson Air Force Base.

This program was undertaken by personnel in the Chemical Physics and Optical Physics Departments under the supervision of Dr. G.S. Picus, Mr. M. Braunstein, and Dr. R.L. Abrams. The program manager was Dr. Zanio. Principal investigators were Dr. Zanio and Dr. L. Fraas. Important contributions to the program were made by Messrs. F. Krajenbrink, K. Miller, P. Hoberg, H. Montano, and A. Timper.

AIR FORCE OFFICE OF SCIENTIFIC RESEARCH (AFSC)
NOTICE OF TRANSMITTAL TO DDC
This technical report has been reviewed and is
approved for public release IAW AFR 190-12 (7b).
Distribution is unlimited.
A. D. BLOSE
Technical Information Officer

SUMMARY OF RESEARCH OBJECTIVES

The following objectives were submitted in chronological order for the statement of work:

- (a) Prepare InP substrates for epitaxial deposition of InP
- (b) Optimize planar reactive deposition (PRD) growth parameters for InP epitaxy on InP substrates
- (c) Grow intentionally doped n-type epitaxial layers
- (d) Characterize InP epitaxial layers according to structural, electrical, and optical properties
- (e) Provide InP epitaxial films to AFOSR for evaluation by the Air Force
- (f) Upgrade and passivate the heat shield design in the PRD apparatus
- (g) Investigate the effects of gas purity by monitoring film quality with alternate gas sources
- (h) Undertake mass spectrographic analysis of the InP films
- (i) Grow n-type InP films via PRD having electron concentrations of $10^{16}/\text{cm}^3$ and less
- (j) Heavily dope the In source with Sn to achieve n^+ films
- (k) Grow an $n^+/n/n^+$ structure
- (l) Deliver an $n^+/n/n^+$ structure to AFOSR for evaluation
- (m) Grow InP films in a low-pressure system, in which In is supplied by evaporation, and phosphorus is supplied via the decomposition of phosphine
- (n) Grow InP films in a low-pressure system in which In and phosphorus are supplied in the gas phase via triethyl indium and phosphine
- (o) Grow InP films in a low-pressure system in which In and phosphorus are supplied in the gas phase via triethyl-indium and phosphorus/halogen mixtures, to investigate halogen effects on background impurities in films
- (p) Grow GaAs films on semi-insulating substances in a low-pressure system in which gallium and arsenic are supplied in the gas phase via trimethylgallium and arsine.

SIGNIFICANT ACCOMPLISHMENTS

- Developed the planar reactive deposition (PRD) technique to grow binary, ternary, and quaternary III-V thin films
- Grew InP films by PRD with room temperature mobilities ($\approx 4000 \text{ cm}^2/\text{Vsec}$) higher than those for films prepared by molecular beam epitaxy
- Prepared n^+ and InP films by PRD with carrier concentrations of a few times 10^{19} cm^{-3} using Sn doping
- Prepared $n^+/n/n^+$ InP multilayer structures on InP
- Prepared large-area (10 cm^2) epitaxial InP films on InP substrates
- Grew lattice matched InGaAs, InGaP, and InGaAsP films on III-V substrate by PRD
- Grew epitaxial layers of Ge on GaAs and Ge substrates at low temperature after modification of the PRD system with internal support
- Constructed a low-pressure metal-organic vapor deposition (LPMOCVD) system
- Prepared unintentionally doped p-type epitaxial GaAs by LPMOCVD, with carrier concentrations as high as several times 10^{20} cm^{-3}
- Prepared unintentionally doped p-type GaAs by LPMOCVD, with a total concentration of electrically active centers ($N_A + N_A$) as low as 10^{16} cm^{-3}
- Used our studies of GaAs defect chemistry to guide us in the direction of future InP thin film growth

TABLE OF CONTENTS

SECTION		PAGE
	LIST OF ILLUSTRATIONS	11
1	INTRODUCTION	15
2	HYBRID MBE/CVD PROCESSES	17
	A. Advantages	17
	B. Description of the Planar Reactive Deposition Process	20
	C. Description of Low Pressure Chemical Vapor Deposition Processes	27
3	FILMS PREPARED BY PLANAR REACTIVE DEPOSITION	35
	A. InP by PRD	35
	B. InGaAs, InGaP and InGaAsP by PRD	54
4	GaAs BY LPMOCVD	59
	A. Experimental Results	59
	B. Discussion	81
5	SUMMARY AND FUTURE WORK	87
	REFERENCES	91
	PRESENTATIONS PATENTS AND PAPERS	95
	APPENDICES	97

LIST OF ILLUSTRATIONS

FIGURE		PAGE
1	The source/substrate assemblies for (a) MBE, (b) PRD, and (c) vacuum CVD illustrate the progressively larger substrate coating capability allowable with gas phase sources	18
2	Planar reactive deposition system (foreground) used for the preparation of InP, InGaAs, InGaP, and InGaAsP and low pressure metal organic chemical vapor deposition system (upper left) used for the preparation of GaAs	21
3	Schematic of PRD source/substrate assembly.	22
4	Vacuum chamber top view for PRD system	23
5	Residual gas spectra.	25
6	Growth of III-V compounds by low-pressure metal-organic chemical vapor deposition in the left deposition position and by planar reactive deposition in the right deposition position	29
7	Schematic of low pressure MOCVD and PRD system sharing the same forepump	32
8	LPMOCVD reactor used to grow GaAs films at 550°C	33
9	Microprobe measurements	36
10	SEM photograph	37
11	SEM photographs of (top) smooth InP epitaxy on (100) InP and (bottom) shingled InP epitaxy on (111) InP for a substrate temperature of about 420°C	38
12	(a) SAD electron channeling	40
	(b) X-ray topograph of InP film on (100) InP substrate	40
13	X-ray Read photographs	41

FIGURE		PAGE
14	Multilayer $n^+/n/n^+$ structure of InP grown by PRD at 350°C on (100) InP substrate	48
15	Broad area epitaxial deposition of InP onto InP wafers	50
16	Unintentionally doped InP films prepared on InP substrates by vacuum technologies	51
17	SEM edge view of GaAs film on cleaved (100) GaAs substrate	62
18	SEM photographs at different positions of GaAs film prepared on (100) substrate at F_{AsH_3}/F_{TMGa} of one	63
19	SEM picture of epitaxial GaAs exhibiting a dull luster (top) and no luster (bottom) as viewed by the unaided eye	64
20	Electron diffraction channeling picture for 20 keV electrons in (top) epitaxial GaAs prepared by LPMOCVD and (bottom) semi-insulating (100) GaAs substrates.	66
21	X-ray Read photograph of GaAs film characteristic of Position 4 in Figure 18	67
22	Dependence of type and carrier concentration on mole fraction ratio of Ga and As for GaAs prepared by MOCVD	69
23	Room temperature hole mobility versus carrier concentration for unintentionally doped (open data points) and intentionally doped (solid data points) GaAs thin films prepared by vacuum technologies	70
24	Hole concentration versus reciprocal temperature for square (dashed) and cloverleaf (solid) Van der Pauw samples of GaAs prepared by LPMOCVD at F_{AsH_3}/F_{TMGa} of four	71
25	Hole mobility versus temperature for square (dashed) and cloverleaf (solid) Van der Pauw samples of GaAs prepared by LPMOCVD at F_{AsH_3}/F_{TMGa} of four	72

FIGURE		PAGE
26	SIMS analysis of GaAs substrate	74
27	SIMS data taken on the GaAs thin film prepared in Run 1 at $F_{\text{AsH}_3}/F_{\text{TMGa}} \approx 1$	75
28	SIMS data taken on the GaAs film prepared in Run 2 at $F_{\text{AsH}_3}/F_{\text{TMGa}} \approx 1$	76
29	SIMS data taken on the same GaAs film as in Figure 28 but at a different position	77
30	SIMS data taken in the GaAs film prepared in Run 4 at $F_{\text{AsH}_3}/F_{\text{TMGa}} \approx 4$	78
31	SIMS data taken of the GaAs sample prepared in Run 5 at $F_{\text{AsH}_3}/F_{\text{TMGa}} \approx 4$	79
32	Carbon and oxygen content versus $N^A + N^D$ for GaAs thin films prepared by MOCVD techniques and for a high "purity" film prepared by VPE.	82

SECTION 1

INTRODUCTION

Thin films of InP are promising for use in high-frequency microwave and transferred electron devices.¹⁻³ These devices require films that are of uniform and precise thickness, contain abrupt doping profiles, and are of high purity. The molecular beam epitaxy (MBE) process⁴ is an especially attractive approach to preparing films with these requirements. However, the transport properties of MBE films, especially InP, are not as good as those prepared by the chemical vapor deposition halide process⁵ and metal organics.⁶ In addition, MBE is an expensive approach; in part because an ultra-high-vacuum (UHV) growth environment is required, and also because only limited substrate coating areas are possible. One of the first objectives of this program was to use the planar reactive deposition (PRD)^{7,8} approach to prepare InP films with improved transport properties. This approach is also a vacuum-deposition technique, and has the potential for preparing films with the above requirements. With this approach, we can prepare films with gaseous sources, and in reactive atmospheres. The use of gaseous sources and reactive atmospheres in PRD are also means of improving the purity of the films. To date, InP films prepared by PRD, using PH_3 as the source of phosphorus, have a higher room temperature mobility⁹ than those prepared by MBE.^{4,10-12} The concept of adding reactive gaseous sources to improve the purity of films has been recently extended to GaAs.^{13,14} Calawa used AsH_3 as the source of arsenic in his MBE system, and obtained films with mobilities higher than those of all other MBE groups. Our concept of using reactive atmospheres to improve the transport properties of III-V films prepared by vacuum technologies has been reinforced.

During the first year of this program, Manasevit et al.¹⁵ had prepared InP films with good transport properties by metal-organic chemical vapor deposition (MOCVD) at atmospheric pressure. Unfortunately, undesirable intermediate reactions occur with this process resulting in

the formation of unwanted compounds.^{16,17} Provided that low carbon concentrations could be achieved, the growth of these films at low pressures and correspondingly lower temperatures might result in layers with significantly improved transport properties for high-speed devices. Therefore, we included additional tasks in the Statement of Work to prepare InP and GaAs by low-pressure (LP) MOCVD. During the course of this program, Thompson-CSF⁶ prepared InP films by LPMOCVD, with transport properties superior to those prepared by MBE and PRD. Our goal of preparing InP by LPMOCVD was never achieved. However, we did accomplish the intermediate steps of constructing a LPMOCVD system, preparing GaAs films, and examining the mechanisms of carbon incorporation.¹⁸ Unintentionally doped p-type GaAs films with concentrations of ionized impurities as low as 10^{16} cm^{-3} were prepared. Our studies of the defect chemistry in GaAs helped us determine the future direction for future InP thin film growth.

In Section 2 we will first discuss the advantages of growing thin films by various vacuum technologies. More specifically, we will describe the growth of InP, InGaAs, InGaP, and InGaAsP by PRD, Ge by low pressure CVD, and GaAs by LPMOCVD. We will then discuss the properties of our In-based films prepared by PRD, and GaAs films prepared by LPMOCVD in Section 3 and Section 4, respectively. The direction of future InP thin film work is discussed in Section 5.

SECTION 2

HYBRID MBE/CVD PROCESSES

A. ADVANTAGES

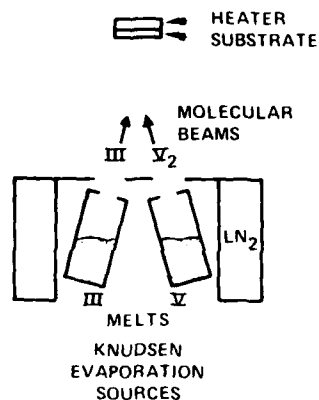
In this section, we describe two hybrid molecular beam epitaxy (MBE) chemical vapor deposition (CVD) processes, which we call planar reactive deposition (PRD) and vacuum CVD. In these two processes, as in the conventional MBE process, source and substrate assemblies operate inside vacuum enclosures. However, in PRD and vacuum CVD, gas-phase sources are used; and the unreacted and reacted by-product gases are pumped away by a turbomolecular pump. In PRD, some of the constituents are supplied by evaporation, while other constituents are supplied by gas phase sources. A hybrid MBE system, which uses AsH_3 as the source of arsenic, therefore, operates within this framework. In vacuum CVD, all of the constituents are supplied from gas phase sources. One advantage of using gas-phase sources is that hydrogen can be readily introduced, and tends to reduce oxygen and carbon incorporation; thereby relaxing, for the same low substrate temperatures, the UVH requirement associated with MBE. The other advantage of gas phase sources is an ability to coat larger substrate areas in PRD and vacuum CVD than in MBE. The source/substrate assembly schematics in Figure 1 illustrate these concepts.

In the preparation of III-V compounds with a conventional MBE system, the group III and group V molecular beams are supplied by evaporation from two spatially separated, thermally isolated Knudsen sources. An epitaxial film is grown on a heated substrate placed in the region where the beams intersect. Because the beam intersection area is limited, the substrate area is also limited (see Figure 1(a)).

The PRD system differs from MBE in that the group III and group V beams originate from the same source, which allows the deposition area to be scaled up in two dimensions. The use of a gas phase source improves

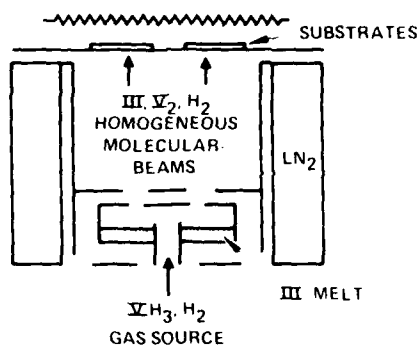
(a) MBE

RGP 10^{-8} TORR



(b) PRD

RGP 10^{-7} TORR



(c) VACUUM CVD

RGP 10^{-7} TORR

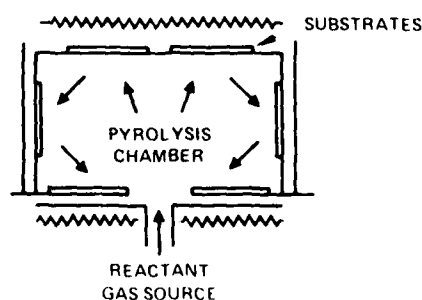


Figure 1.
The source/substrate assemblies for (a) MBE,
(b) PRD, and (c) vacuum CVD illustrate the
progressively larger substrate coating
capability allowable with gas phase sources.

film homogeneity (see Figure 1(b)). Thus, in PRD, the group III element is evaporated from a crucible just as in MBE. However, the group V element originates by introduction of the group V hydride gas into the group III source cavity. Since group V and group III vapors mix in the same source, a more homogeneous molecular beam originates from a single source, thus permitting uniform depositions over a larger area. In Section 3 we will discuss the properties of InP, InGaAs, InGaP, and InGaAsP prepared by this process.

The vacuum CVD process potentially allows even more scalability. This arises because the sticking coefficients for most gas-phase sources are not unity.²²⁻²⁴ When each reactant gas molecule undergoes multiple collisions before sticking, the substrates can be mounted around the perimeter and on the bottom, as well as the top of the deposition cavity (see Figure 1(c)). Conceivably, the substrates could even be stacked on shelves within the deposition cavity, as is done for low-pressure CVD polysilicon coatings.²⁵ Later in the same section we will discuss the preparation of epitaxial films by the pyrolysis of GeH_4 .^{20,21} Internal support was used to prepare Ge films. However, because the pyrolysis of GeH_4 was an intermediate step to prepare GaAs, we include it on this report.

When the reaction probability per collision for one of the gas phase reactants is unity, as in the growth of III-V films by MOCVD, the degree of scalability decreases. However, the benefits from operating at a reduced pressure may still justify growth by this process. It may be desirable to (1) reduce the interaction of the reactants in the vapor phase, (2) reduce the substrate temperature, and (3) reduce the degree of autodoping from the film. Reducing the substrate temperature reduces interdiffusion between the film and the substrate, and reduces contamination of the film from the environment. If the growth rate is kinetically limited by an interface between the vapor and the substrate, reducing the temperature may further enhance this kinetic limitation.

However, the kinetic limitation can be alleviated if the pressure is reduced. Also, in MOCVD growth the incorporation of high concentrations of carbon may be unacceptable.

Having discussed some of the potential advantages associated with gas-phase sources, we present in the following sections a more detailed description of the PRD and vacuum CVD equipment, as well as substrate preparation procedures used to obtain the epitaxial films described in Sections 3 and 4.

B. DESCRIPTION OF THE PLANAR REACTIVE DEPOSITION PROCESS

We have prepared InP, InGaAs, InGaP, and InGaAsP with the PRD process. A photograph of the PRD system is shown in Figure 2. It consists of a metal vacuum chamber that is pumped on by a turbomolecular pump located directly below it. Two PRD deposition units are located within the vacuum chamber. A cross section through the PRD unit is shown in Figure 3. The substrate is mounted above the source cavity, which is enclosed by a liquid nitrogen shroud. Heat shields are mounted within this shroud. In the preparation of InP, In metal is evaporated from a graphite crucible. A PH_3/H_2 gas mixture is then introduced into the crucible. The PH_3 gas decomposes in the In source cavity, and In vapor, P vapor, and H_2 gas stream onto the substrates. A schematic top view of the substrate plate, which rides on bearings, is shown in Figure 4. The vapor pressure of the In controls the film growth rate and is determined by the source temperature. Residual gases are exhausted at the pump port by the turbomolecular pump. Stoichiometric films are produced by adjusting the mass flow controller to allow an excess of P vapor in the inner growth chamber. In the growth of InGaAs, InGaP, and InGaAsP, both In and Ga are added to the Knudsen cell. In the growth of InGaAsP, a premixed ratio of AsH_3 and PH_3 was also introduced into the Knudsen cell.

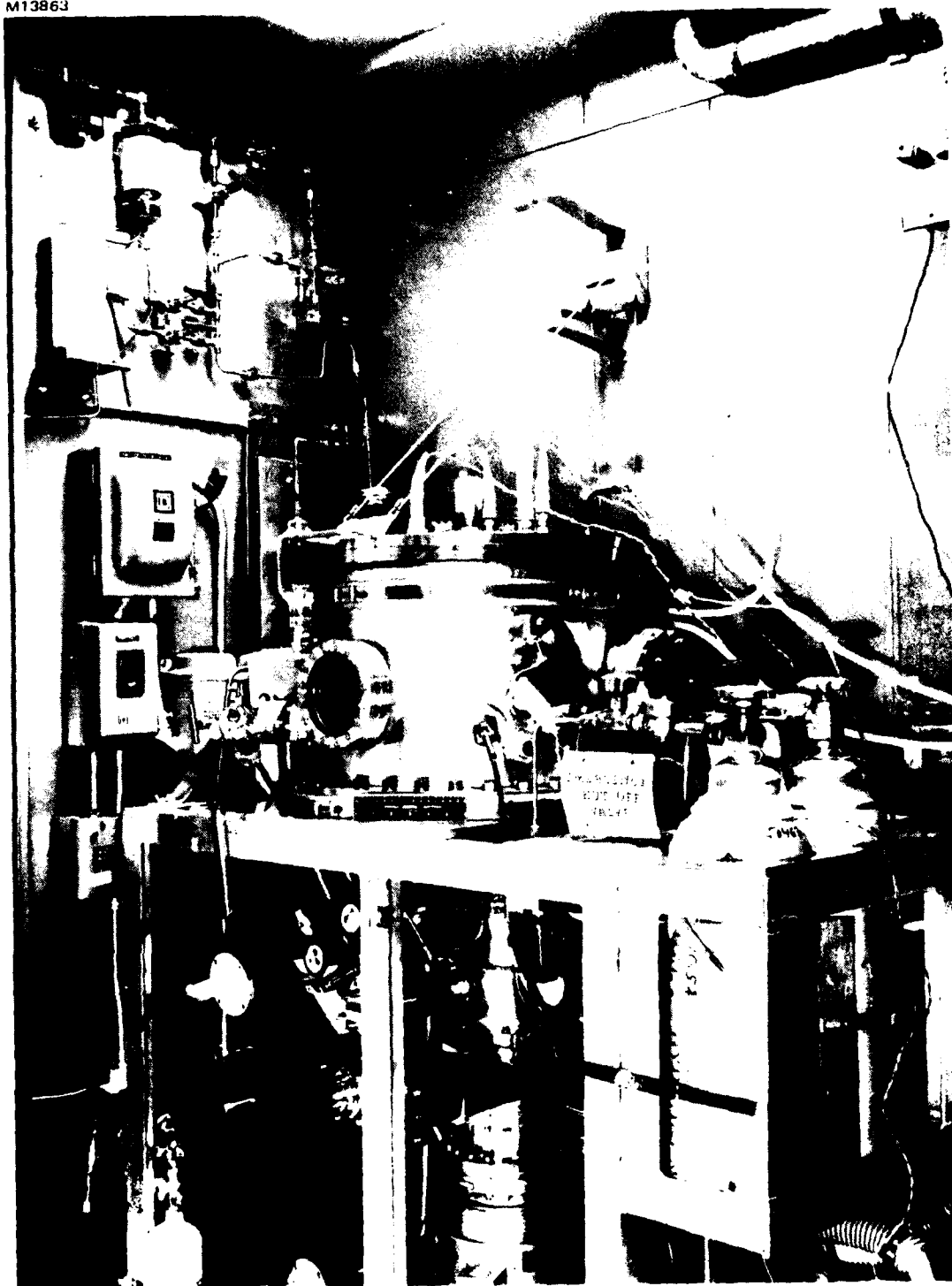


Figure 2. Planar reactive deposition system (foreground) used for the preparation of InP, InGaAs, InGaP and InGaAsP and low pressure metal organic chemical vapor deposition system (upper left) used for the preparation of GaAs.

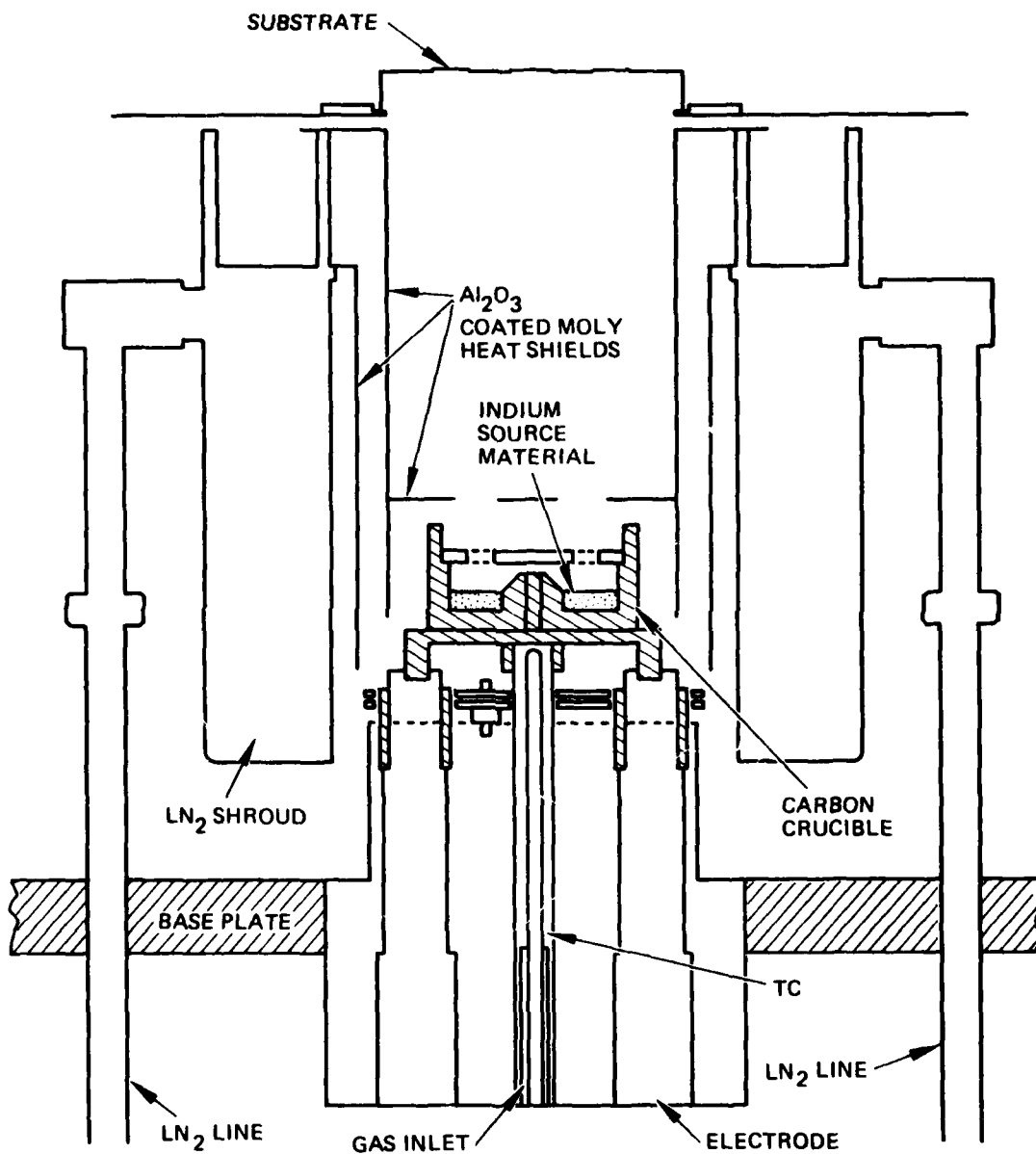


Figure 3. Schematic of PRD source/substrate assembly.

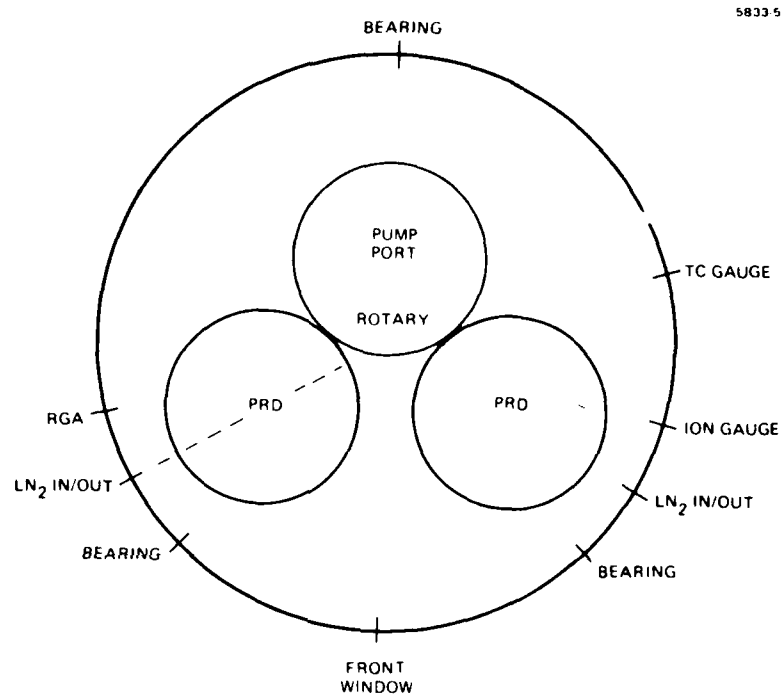
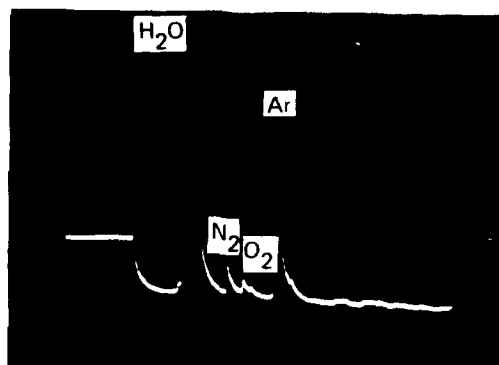


Figure 4. Vacuum chamber top view for PRD system.
The dashed line in this drawing represents
the cross section shown in Figure 3.

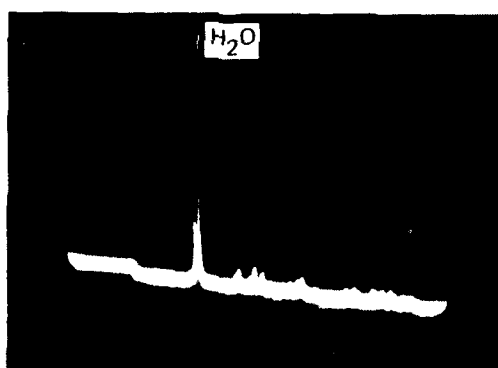
The PRD assembly is equipped with a residual gas analyzer (CVC Quad 1210, 0 to 100 amu). This permits identification of impurity gases before and after film deposition. Figure 5 shows spectra (a) during pumpdown after sample loading, (b) before filling with LN_2 , (c) after adding LN_2 to the shroud, (d) while throttling the gate valve to increase the background pressure of noncondensable gases, (e) during source outgassing, and (f) four hours after the run. After loading and pumping down the system, the total pressure is about 10^{-7} Torr. Adding LN_2 lowers the pressure of condensable gases, in this case primarily H_2O , by an order of magnitude. Note the decrease in H_2O peak intensity from (b) to (c). To help identify our background contaminants we throttled the gate valve while the chamber was filled with LN_2 . The intensities of the CO peak and another unknown peak corresponding to a higher mass increased. During outgassing the pressure then rose as a result of the release of H_2 and CO from the source. The horizontal and vertical gains for the RCA spectra were not all the same. Therefore, it could be misleading to respectively relate peak position and associate the partial pressure with areas under the peaks.

Growth procedures and substrate preparation are briefly described below. For this program, epitaxial InP films were grown on (100) semi-insulating and (100) and ($\overline{111}$) n-type InP substrates obtained from Cambridge Instruments, Metals Research Division. The saw-cut 1.5 in. diameter InP wafers are diced into 3/8 by 3/8 in. squares and then mounted with In on 1/4 in. high, 5/8 in. diameter cylindrical Mo blocks. A 5% bromine-in-methanol solution is applied to a lens paper pad on a glass plate. Polishing the samples by hand from 3 to 5 min yields an optically smooth surface with only a slight "orange peel" effect. The samples are then rinsed and stored in electronic-grade methanol. The samples, just before being loaded, are etched for 10 min in a 0.1% Br:methanol solution, and rinsed in methanol and 10 MS deionized water. The samples are then spun dry and set into the rotary substrate plate in the PRD chamber. After pumping down the vacuum chamber to the 10^{-7} Torr scale, LN_2 is added to the shroud. The source is turned up to 850°C



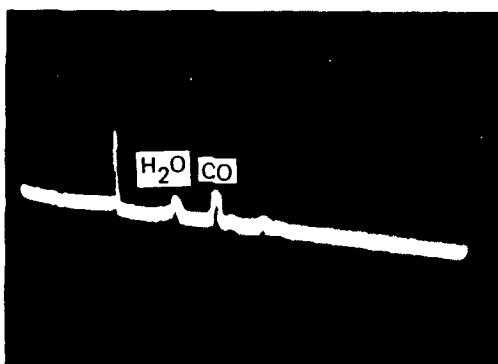
10642-7

- (a) 1×10^{-6} Torr
DURING PUMPDOWN



10642-8

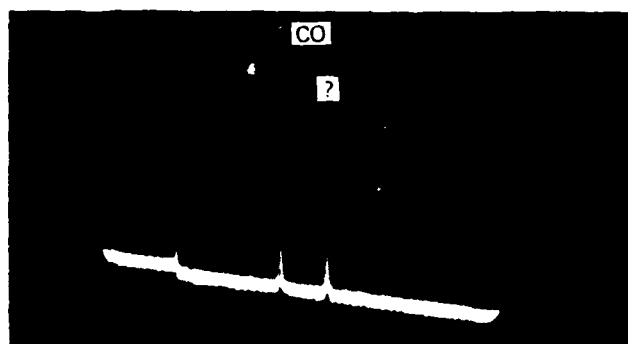
- (b) 9×10^{-8} Torr
BACKGROUND, No LN₂



10642-9

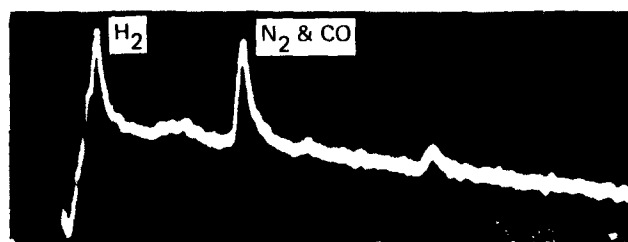
- (c) 9×10^{-9} Torr
BACKGROUND, WITH LN₂

Figure 5. Residual gas spectra outside LN₂ shrouds. (a) During pumpdown after sample loading. (b) Before filling with LN₂. (c) After filling with LN₂.



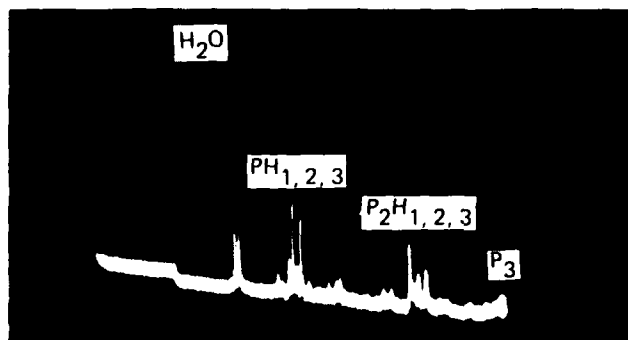
10642-10

- (d) 3×10^{-7} Torr
BACKGROUND, WITH LN_2 AND
GATE VALVE THROTTLED



10642-11

- (e) 7×10^{-8} Torr
DURING SOURCE
OUTGASSING



10642-12

- (f) 1.5×10^{-7} Torr
4 HOURS AFTER RUN

Figure 5. Residual gas spectra outside LN_2 shrouds. (d) After filling with LN_2 and throttling gate valve. (e) During source outgassing. (f) Four hours after run.

for outgassing, while the substrates are being preheated to 350°C in an adjacent position not over the source. The PH_3/H_2 gas mixture (either 10% or 50% PH_3 in H_2) is introduced, and the total gas flow rate is determined by a Tylan Corp. FC-260 mass flow controller. The flow rate is typically 10 std cm^3/min . After the source is outgassed for 60 min., it is turned down to 500°C and the substrates are rotated into position above the source. The InP substrates are then heated to 475°C for thermal cleaning in the presence of P vapor. The P vapor stabilizes the InP surface against In droplet formation¹⁶ and allows reproducible thermal cleaning. Finally, the substrate temperature is set to the desired deposition temperature and the source temperature is turned down to 500°C while the substrates are allowed to cool to 300°C before either rotating to the next deposition position or turning off the P vapor flux.

C. DESCRIPTION OF LOW PRESSURE CHEMICAL VAPOR DEPOSITION PROCESSES

Growth of InP by MOCVD at one atmosphere often results in the formation of a solid addition compound thought to have the composition $(\text{CH}_3\text{InPH})_x$.^{16,17} Growth at low pressure avoids the formation of unwanted intermediate reactions. Both Ge and GaAs thin films were grown by vacuum CVD. The growth of these films were intermediate steps for the growth of InP by metal organics.

One of the most important advantages of an all-CVD process is the flexibility in preparing ternary and quaternary multilayer structures. Although the composition profile of the group V elements may be varied through the control of the gas flow ratios in PRD, co-evaporation of the premixed group III reactants from the Knudsen cell in a fixed ratio limits the flexibility of the system. Introducing the group III reactants into the deposition system in the vapor phase as a metal organic permits the reactant composition profile to be controlled, hence permitting an unlimited number of layers with different compositions to be prepared.

1. Low-Pressure CVD Growth of Germanium

In the growth of Ge the carbon crucible was replaced by a 4-in. diameter, 6-in. high quartz cup with a sleeve at the bottom, through which GeH_4 entered the vacuum chamber. This cup is shown on the left-hand side of Figure 6. In this process both Ge and GaAs substrates are loaded into the system on the rotary substrate and placed over the quartz cup. After outgassing of the substrates and cup, CH_4 is introduced into the system to initiate growth. These studies were undertaken with internal funding and are discussed in more detail in Reference 20.

2. Low-Pressure MOCVD Growth of GaAs

In this process, the metal organic compound decomposes as it makes contact with the hot substrate, thus depositing the group III atom, and releasing methane, ethane, and unsaturated carbon-hydrogen molecules into the vapor phase. This step is similar to the decomposition of GeH_4 . However, it is different, in that with GeH_4 multiple collisions are required to completely decompose GeH_4 , whereas with the metal organic compounds only a single collision is required to do so.^{6,15,26} When a hydride, such as AsH_3 is introduced in the presence of excess Ga, GaAs is formed.

The next step in growing InP was to grow GaAs. GaAs is easier to grow because the metal organic compound does not react with the hydride in the vapor phase as it does in the growth of InP. A gas train including $(\text{CH}_3)_3\text{Ga}$ (TMGa) and $(\text{C}_2\text{H}_5)_3\text{In}$ sources was assembled and plumbed into the PRD system. (See left hand side of Figure 6.) The 10% mixture of arsine in hydrogen used in the growth was purchased from Scientific Gas Products. The metal organics were purchased from Alfa Ventron.

a. Growth Inside the PRD Chamber

The growth of GaAs was undertaken in the quartz chamber that was used to grow the Ge films. As a first step we calibrated the growth rate by depositing Ga on sapphire substrates. In the growth of

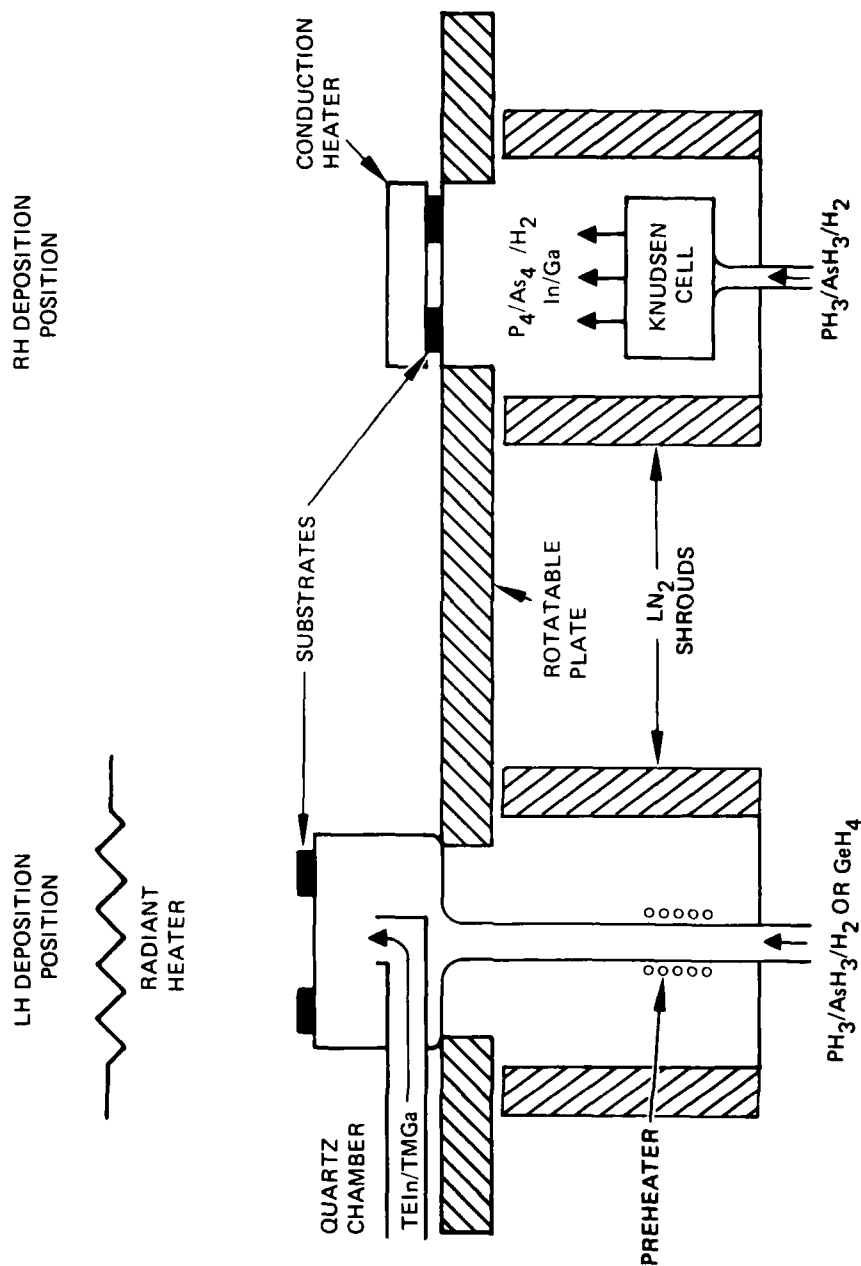


Figure 6. Growth of III-V compounds by low-pressure metal-organic chemical vapor deposition in the left deposition position and by planar reactive deposition in the right deposition position.

GaAs, the AsH_3 flowrate was first established. Then TMGa was bled into the system. The actual pressure during growth was not known because the thermocouple gauge was located outside of the quartz deposition chamber. Films were analyzed by a microprobe and were found to be stoichiometric within the accuracy of the microprobe.

The growth of the metal-organic compounds inside the PRD chamber was discontinued for several reasons. First, we intended to eventually grow the metal organic compounds in the presence of HCl. Chemical attack of the turbopump and the metal parts might occur with the present experimental arrangement. Second, the metal organics appeared to be a source of contamination in the right side PRD deposition chamber. Subsequent to the deposition of GaAs by metal organics, we prepared single-crystal epitaxial InP films by PRD in the alternate right side deposition position. The electrical properties of the InP films were poor. Although enough runs were not undertaken to ensure that the metal-organic deposition was a source of contamination, particulate matter in the PRD chamber in the form of flakes from the metal-organic film process were found. This discouraged undertaking both processing techniques in the same vacuum chamber. Besides the substrate plate, the quartz lamp heats other parts in the vacuum system, and metal-organic vapors decompose on contact with them. The quartz lamp eventually becomes coated itself. By heating the Mo substrate by conduction instead of radiation, some of these problems were solved. However, it was difficult to prevent embrittlement of the exposed heater filaments, which were required to heat the substrate plate by conduction up to 700°C .

The preparation of layers from metal organics would also interfere with our plans for preparing $n^+/n/n^+$ structures for this program and multilayer structures for other programs because the preparation of multilayer structures by PRD required both deposition positions. For these reasons we prepared GaAs, and intended to prepare InP in a similar quartz chamber located outside of the PRD vacuum chamber.

b. Growth Outside of the System

Figure 7 is a schematic of the PRD and revised LPMOCVD systems shown in Figure 2. Both systems share the forepump. A line connects the high-vacuum PRD chamber and the exhaust of the LPMOCVD chamber. In this system, the TMGa and 10% mixture of AsH_3 in hydrogen are bled into a vertical quartz reactor (Figure 8). These mixtures decompose and react to form GaAs on the (100) semi-insulating GaAs, sapphire substrates, and the quartz pedestal. The outer quartz jacket is coated with GaAs, to a lesser extent because its temperature is significantly lower than the substrate which was held at about 550°C . The substrates were radiatively heated by a coil located directly under the pedestal. Visible radiation from the heater allowed us to observe the coating of the sapphire and pedestal during growth. H_2 and the gaseous byproducts of the TMGa decomposition are pumped out through the opening between the outer quartz jacket and the concentric quartz pedestal by a Leybold Hereaus rotary vane pump, having a base pressure of about 10^{-4} Torr. A cold trap between the rotary vane pump and the system decreases oil backstreaming. A working pressure below 50 Torr is maintained by a needle valve located between the reactor and the cold trap, and is measured upstream from the reactor at the intersection of the H_2/PH_3 and TMGa lines. The actual pressure in the reactor was less than 50 Torr. A residual gas analyzer located between the turbomolecular pump and the exhaust of the reactor was used for leak checking. When the system was outgassed and leak-checked, the valve to the forepump was closed and the system was pumped on by the turbopump.

Before loading the substrates, the quartz pedestal is baked out in vacuum for 30 min. at 550°C . The remainder of the system is baked out at about 100°C . After the reactor is cooled to room temperature, the system is backfilled with N_2 , and the outer quartz jacket removed from the pedestal. Wafers of GaAs approximately 2 cm by 1 cm, and a sapphire disk approximately one centimeter on a side are placed on the pedestal. Previous to loading, the GaAs wafers are given a 10 sec 0.1% bromine-in-methanol etch and blown dry in dry N_2 . After closing the reactor, the

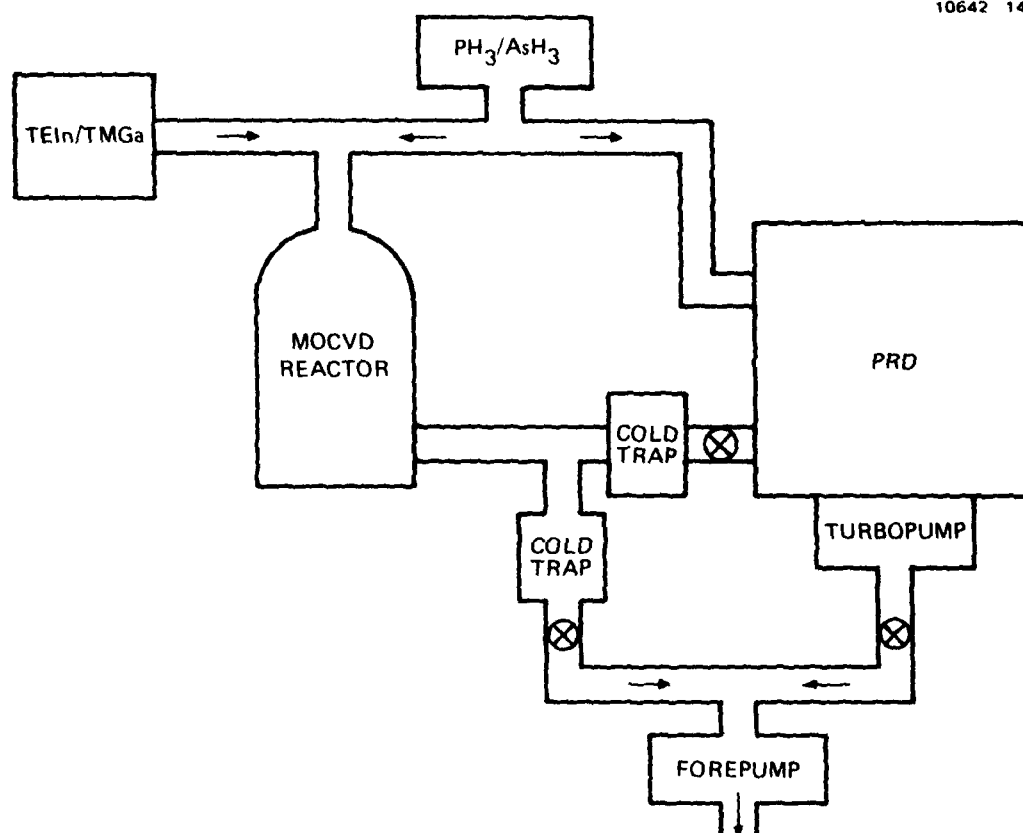


Figure 7. Schematic of low pressure MOCVD and PRD system sharing the same forepump.

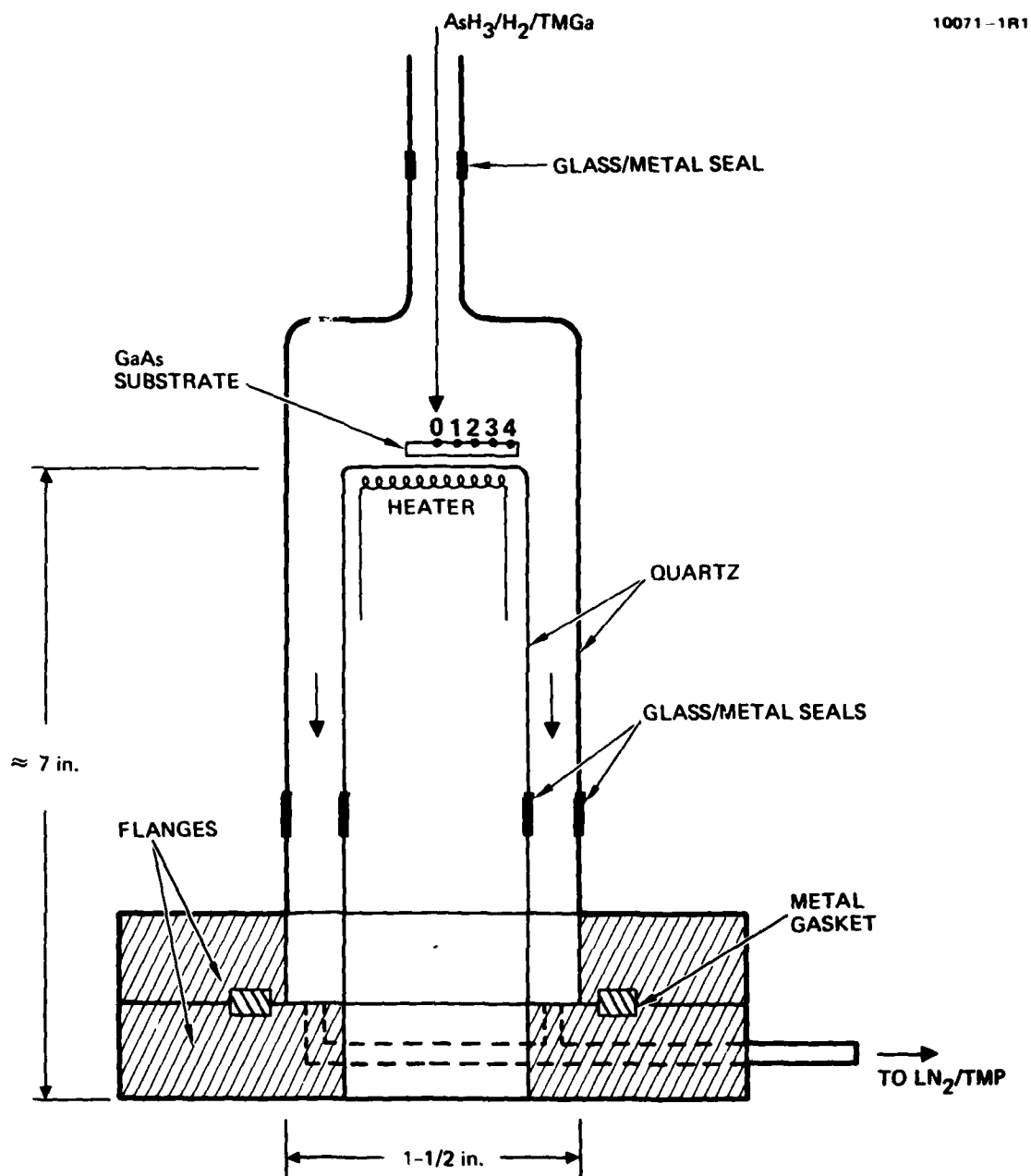


Figure 8. 1-PMOCVD reactor used to grow GaAs films at 550°C.

system is purged with AsH_3/H_2 and heated to the growth temperature. After about 20 min at 550°C , growth is initiated by introducing TMGa. The total flow rate is about 50 cc/min. After 10 min of growth, the pedestal and sapphire darken indicating coverage of the GaAs substrate. After one to three hours, growth is terminated by stopping the TMGa flow. The substrate temperature is reduced to room temperature before turning off the AsH_3 . To change the ratio of the AsH_3 flow to the TMGa flow ($F_{\text{AsH}_3}/F_{\text{TMGa}}$), the TMGa flow is varied by about a factor of three. The exact ratio is established by adjusting the AsH_3 flow rate. Runs at low $F_{\text{AsH}_3}/F_{\text{TMGa}}$ last about one hour. To obtain the same film thickness, runs at higher $F_{\text{AsH}_3}/F_{\text{TMGa}}$ last about three hours. That the film thickness was proportional to the TMGa flow rate is consistent with the literature. Before the first of the three runs at the higher flow rate ratio, the system was not baked out and the growth conditions were considered to be atypical.

SECTION 3

FILMS PREPARED BY PLANAR REACTIVE DEPOSITION

About 80 runs were undertaken by PRD in this program. The first 20 runs established the growth rates, the PH_3 flow rates, and the growth procedure discussed in Section 2. The next 10 runs were directed toward obtaining epitaxial films with good morphology. Films were intentionally doped with Sn in the next 10 runs to obtain n^+ doping. In the next 20 runs we obtained films with the best transport properties. In the last 20 runs we prepared $n^+/n/n^+$ structures, large area coatings, and ternary and quaternary layers.

A. InP BY PRD

1. Experimental Results

a. Crystal Perfection and Morphology

Microprobe measurements (Figure 9) were initially used to establish that stoichiometric films were obtained. Scanning electron microscope (SEM) pictures were simultaneously taken to examine the morphology. Figure 10 shows SEM pictures of InP films deposited on (100) InP and GaAs at about 420°C. A polycrystalline film deposited on a sapphire substrate at the same temperature is included for comparison. The best films on a (100) surface are optically smooth and free from defects when analyzed with an SEM. The quality of the epitaxial deposition depends on surface preparation. It was especially important to remove damage induced by sawing the wafers. Our preparation procedure is discussed in Section 2. Figure 11 shows SEM photographs of InP deposited onto (100) InP and $\overline{(111)}$ InP. The contrast between the smooth (100) and the typically shingled $\overline{(111)}$ surfaces is evident. These photographs are characteristic of InP films that have not been

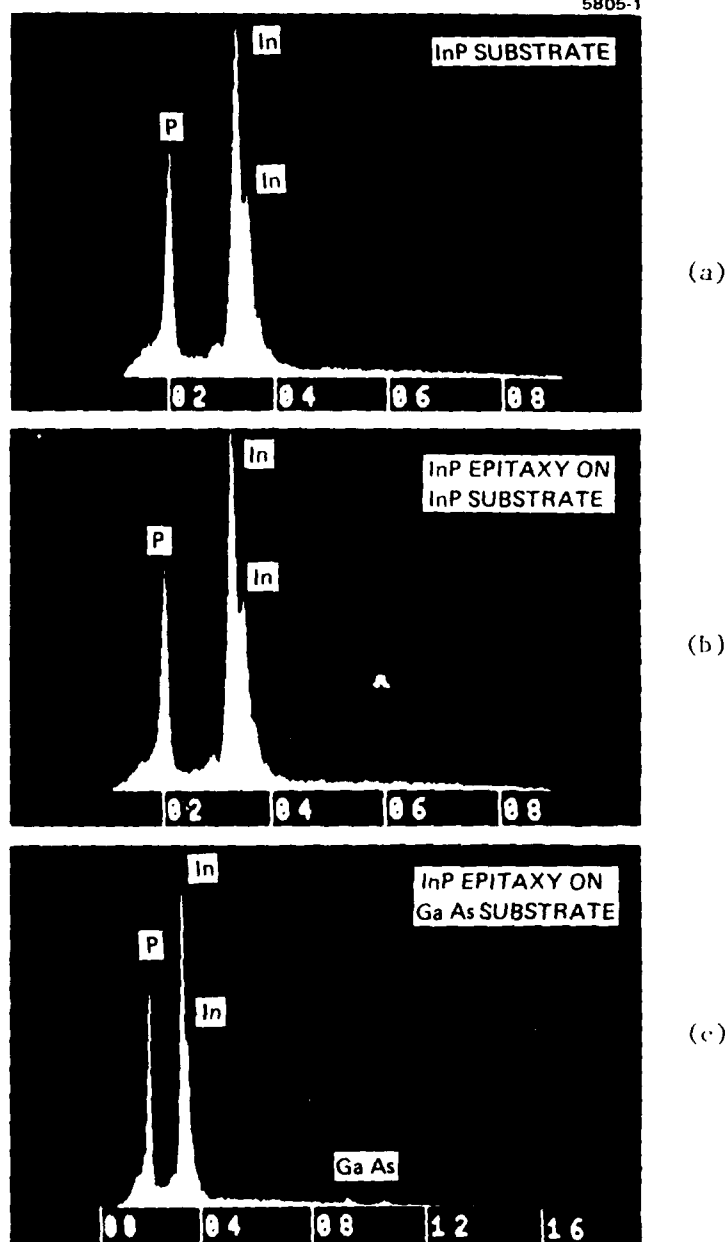


Figure 9.
Microprobe measurements. (a) An InP substrate.
(b) The epitaxial deposition of InP on the same
InP substrate. (c) The epitaxial deposition of
InP on a GaAs substrate.

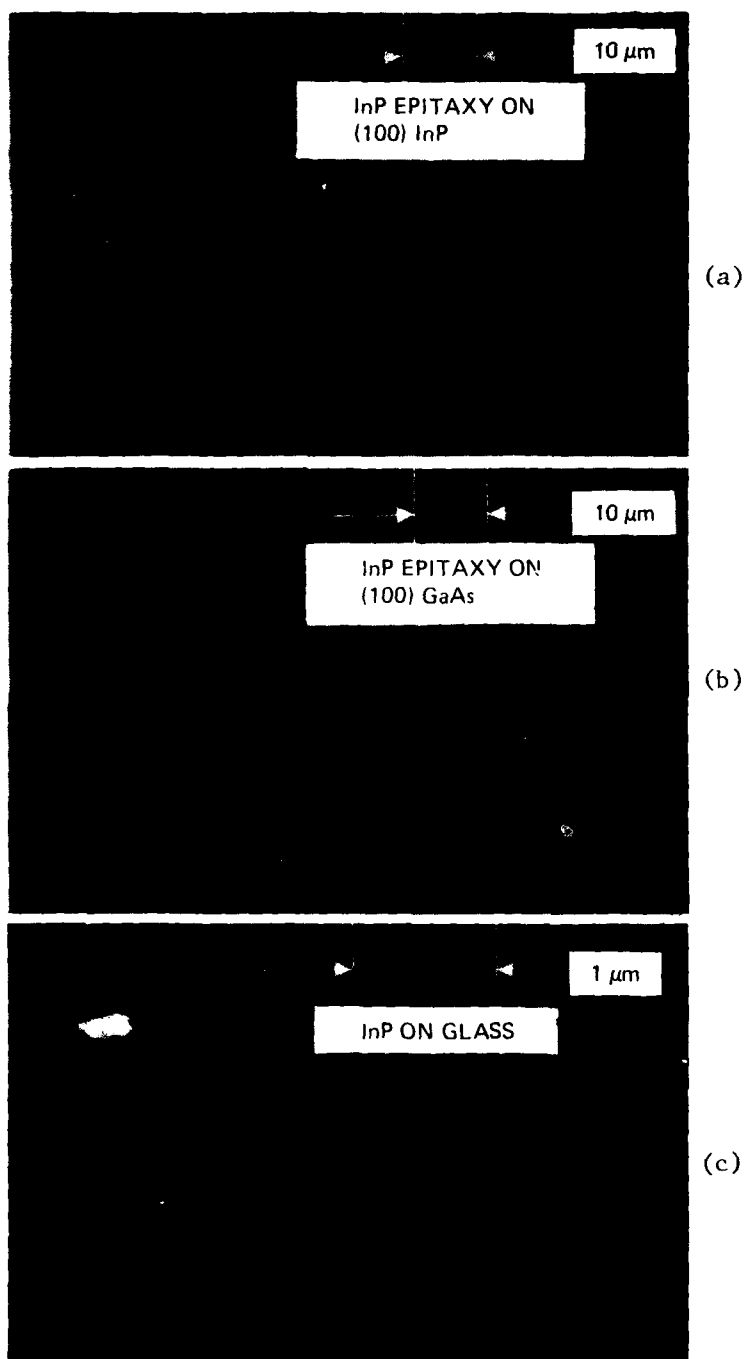


Figure 10.
SEM photograph. (a) Epitaxial deposition of InP on a (100) InP substrate. (b) Epitaxial deposition of InP on a (100) GaAs substrate. (c) deposition of InP on glass.

5900-2 R1

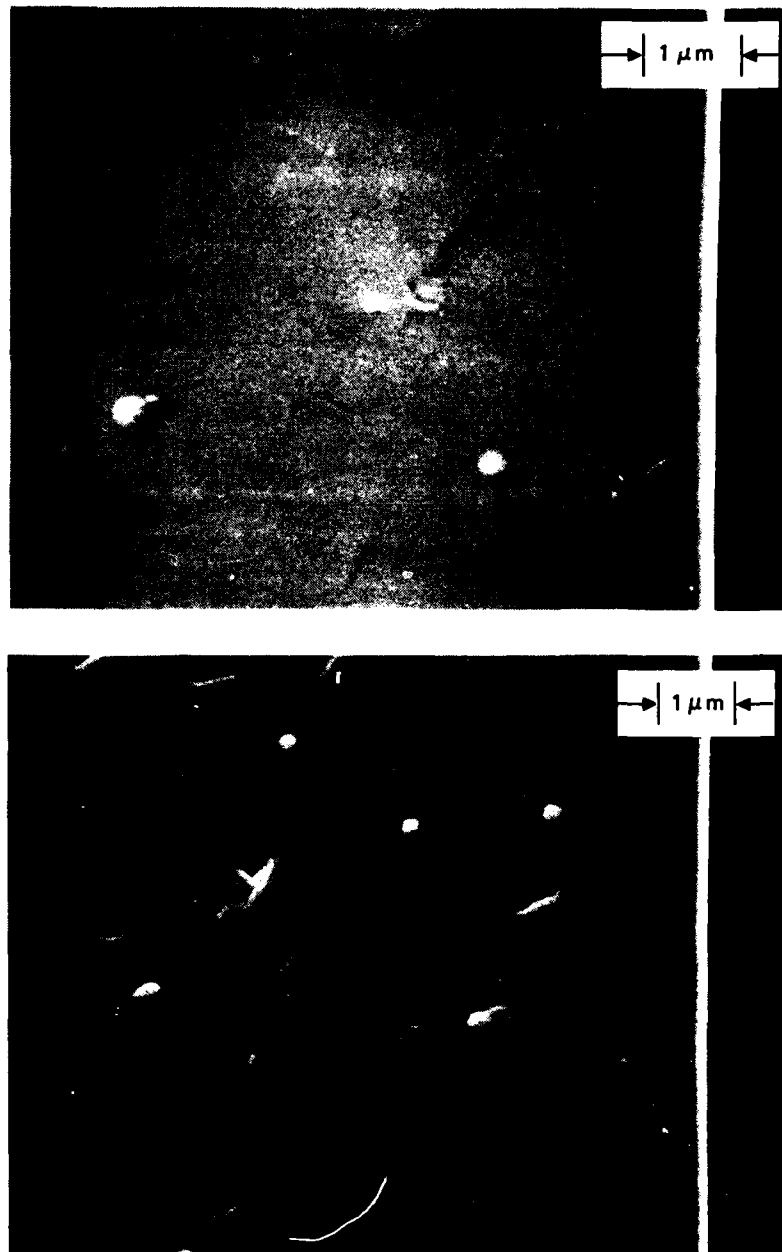


Figure 11. SEM photographs of (top) smooth InP epitaxy on (100) InP and (bottom) shingled InP epitaxy on (111) InP for a substrate temperature of about 420°C.

phosphorus stabilized, resulting in microprecipitates of In. These may be compared with Figure 10 where stabilization was used.

Selective area electron diffraction (SAD), x-ray Read and x-ray topographs were taken to further examine the crystalline perfection of the layers. Most of our films examined by SAD showed well-defined electron channeling patterns (Figure 12(a)) with no differences between the substrate and the layer. The x-ray Read camera delineated films of superior crystal perfection from those with poorer crystal perfection.

In a program for the Department of Energy under Contract XJ-9-8170-1, we examined crystal perfection at lower temperatures. It was more difficult to consistently obtain high-quality films at lower temperatures. At lower growth temperatures it was common to see the electron channeling pattern degrade, so that differences between the layer and the substrate became apparent. However, we did achieve epitaxy at a substrate temperature as low as 260°C. Figure 13(a) shows an x-ray Read photograph of an InP film grown on a sapphire substrate at 320°C. The rings are characteristic of the polycrystalline InP, the spots of the sapphire substrate. Figure 13(b) is a Read photograph of InP grown on a (100) semi-insulating InP substrate at 320°C during the same run. The spots are characteristic of the single-crystal epitaxial film and the single-crystal substrate. Rings characteristic of polycrystalline InP were not observed. In the next run, the substrate temperature was lowered to 260°C. Growth on the (100) InP substrate resulted in a Read photograph (Figure 13(c)) that is identical to Figure 13(b) and is characteristic of epitaxial growth.

Some of our better films were examined with x-ray topographs. Figure 12(b) shows a topograph of a layer (outlined by the circle) prepared at about 380°C and the substrate. The four artifacts at the periphery of the deposition are Hall contacts. The artifacts in the interior are caused by handling. Within the resolution of the technique, entire films were found to be free from low-angle grain boundaries, and were at least as good in quality as were the substrates.

10642-13

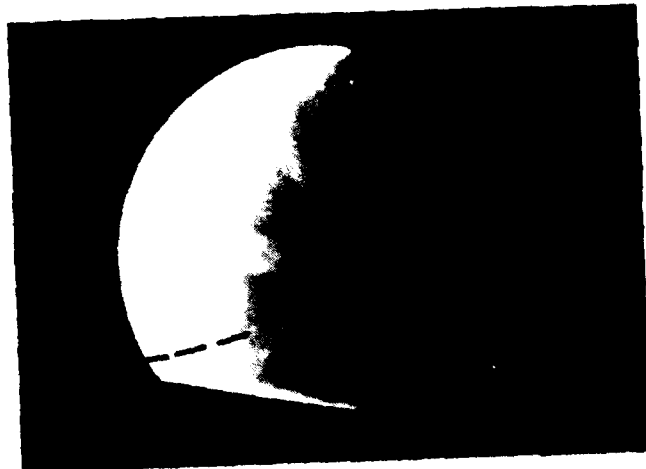
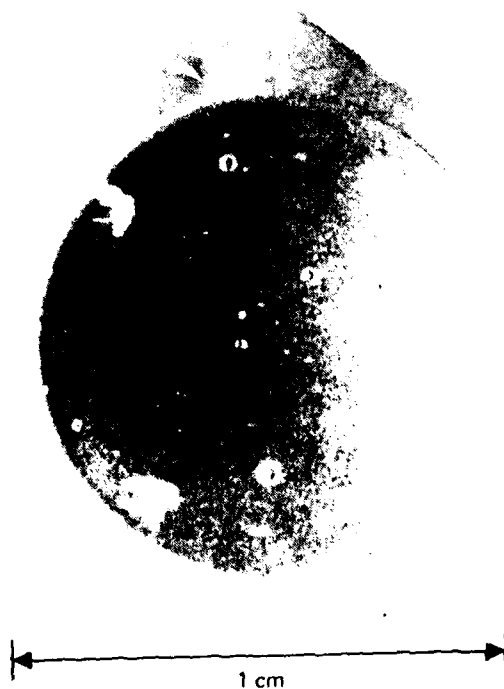
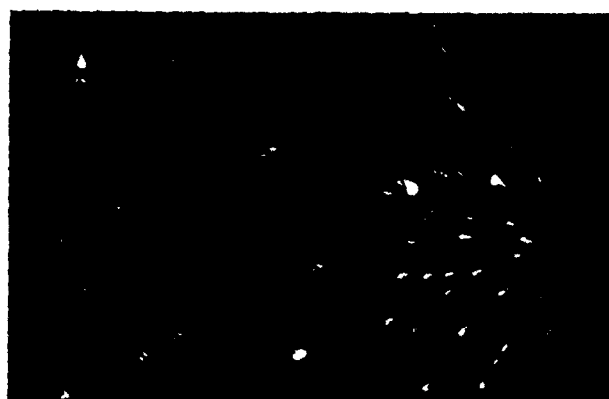


Figure 12(a).
SAD electron channeling
pattern.

7033-2

Figure 12(b).
X-ray topograph of InP
film on (100) InP
substrate.





(a) InP/SAPPHIRE
AT 320°C



(b) InP/(100)InP
AT 320 °C



(c) InP/(100)InP
AT 260°C

Figure 13. X-ray Raman photographs of (a) polycrystalline InP deposited on sapphire at 320°C. (b) Epitaxial InP deposited on (100) InP at 320°C. (c) Epitaxial InP deposited on (100) InP at 260°C.

b. Electrical Properties

Although the morphology and crystal perfection of the best layers in our early runs at a substrate temperature of about 380°C were excellent, the room temperature mobilities were only in the 1,000 to 2,000 cm^2/Vsec range, corresponding to a total impurity concentration about 10^{18} cm^{-3} . The carrier concentration did not freeze out, indicating a shallow center. Because of the poor mobilities and the high electron concentrations, we undertook an impurity analysis of our In and our film (to be discussed later) and modified our system.

The first design modification consisted of relocating the LN_2 shrouds. Previously, the LN_2 feedthroughs had entered the vacuum chamber through its side walls. Removing the shrouds for cleaning required removing the electrodes and the coolant water and PH_3 lines. Cleaning the shrouds had previously entailed considerable down time and disturbed the clean Knudsen-cell deposition region. Relocating the LN_2 shrouds simplified their cleaning, and by so doing, reduced down time.

The second machine modification consisted of upgrading the quality of the hot parts in the deposition region of the chamber to reduce the vapor pressure of the volatile impurities from those parts. The stainless-steel thermocouple sheath was replaced by a Mo thermocouple sheath. The Mo heat shields enclosing the Knudsen cell were coated with Al_2O_3 . The PH_3 ceramic inlet tubes to the Knudsen cells were replaced by BN. In addition, the apertures from the Knudsen cells were increased to permit lower source temperatures for the same deposition rates.

After modifying the system we obtained improved transport properties. Table 1 summarizes electrical data in successive runs for undoped n-type InP films prepared at 400°C after these modifications.⁹ Each run contained two deposition positions and four 1 cm^2 samples at each position. Mobilities ranged from about 2,000 cm^2/Vsec to

Table 1. Electrical Data for Undoped n-Type InP
Prepared by PRD

Run	Position	Van der Pauw Mobility, cm^2/Vsec		Electron Concentration, cm^{-3}	Thickness, μm
		Square Sample	Cloverleaf		
69	1	2,267	2,186	6.06×10^{16}	1
	2	1,667		1.07×10^{17}	1
	2- 3	2,393		4.97×10^{16}	1
	4	1,943		5.03×10^{16}	1
	1	2,652	2,430	9.91×10^{15}	1
	2	2,610		8.44×10^{15}	1
	3- 3	1,990		1.19×10^{16}	1
	4	2,207		9.35×10^{15}	1
70	1	1,292	2,026	2.33×10^{17}	1.3
	2	1,607		7.7×10^{16}	1.3
	2- 3	1,458		4.32×10^{17}	1.3
	4	1,553		6.35×10^{16}	1.3
	1	1,632	2,461	1.49×10^{16}	2.6
	2	1,455		4.55×10^{16}	2.6
	3- 3	2,905		1.06×10^{16}	2.6
	4	2,413		8.6×10^{15}	2.6
71	1	1,308	1,809	1.07×10^{17}	1.3
	2	1,420		8.18×10^{16}	1.3
	2- 3	1,528		8.67×10^{16}	1.3
	4	1,669		7.19×10^{16}	1.3
	1	3,010	4,062	1.43×10^{16}	2.6
	2	3,041		1.82×10^{16}	2.6
	3- 3	2,757		2.96×10^{16}	2.6
	4	2,524		2.43×10^{16}	2.6

T6296

4,000 cm^2/Vsec , corresponding to total impurity concentrations of $2 \times 10^{17} \text{ cm}^{-3}$ to $2 \times 10^{16} \text{ cm}^{-3}$. (The carrier concentrations in the table refer to the electron concentration and not to $N_A + N_D$, the total impurity content.) Undoped films prepared on (100) semi-insulating substrates were always n-type. The highest room temperature electron mobility was 4,062 cm^2/Vsec . This corresponds to a concentration of electrically active impurities of a few times 10^{16} cm^{-3} . The 77°K mobility for one of our better films, having a room-temperature mobility of $\sim 3,300 \text{ cm}^2/\text{Vsec}$, was 13,000 cm^2/Vsec . In our Hall measurements with the Van der Pauw technique, routine measurements with a circular film, and precise measurements with a cloverleaf film were made. The cloverleaf configuration generally gives a higher, but more correct, mobility. The precise reason for the improvement in the transport properties was not determined. However, it is related to upgrading the quality of the system.

Intentional n-type doping in the 10^{17} to 10^{19} cm^{-3} range was accomplished by adding Sn to the source. About 3 g of Sn in a 30 g source corresponded to doping concentration of 10^{18} cm^{-3} . P-type doping was also accomplished under Department of Energy Contract XJ-9-8170-1. With these films we prepared solar cells with AM2 efficiencies of 10%.⁹ These results are a further indication of the quality of the InP.

c. Impurity Analyses

Because of our initial low mobility results, we undertook a mass spectrographic analysis of our films. Table 2 is a mass spectrographic emission analysis of a 4- μm -thick InP film deposited onto a high-purity Si substrate. Films simultaneously deposited onto semi-insulating InP substrates for purposes of electrical evaluation indicated about 10 ppma of electrically active defects. Carbon and oxygen were detected as residuals in quantities less than 3 ppma. The main impurity in this film was sulfur at 6 ppma. We believe that this high concentration of sulfur is a result of residual contamination from an

Table 2. Mass Spectrographic Analysis of a 4- μ m-Thick Film of InP Deposited on Si by PRD

Element	Concentration, ppm	
	InP Film	Si Substrate
B	0.05	0.05
C ^R	3.0	5.1
O ^R	3.4	6.5
F	1.4	2.1
Mg	1.7	1.0
S	6.4	1.0
Cl	2.4	2.1
Ti	0.3	0.1
Cr ^R	0.2	0.4
Cu	1.0	0.4
Mn	1.5	2.0
Zn	0.1	0.05
Ba	1.5	Not detected
Fe	Not detected	Not detected
Mo	Not detected	Not detected
Ga ^R		
As ^R		
Be	Interfering lines	Interfering lines
N	Interfering lines	Interfering lines
Na	Interfering lines	Interfering lines
Sc	Interfering lines	Interfering lines
Co	Interfering lines	Interfering lines
Nb	Interfering lines	Interfering lines

R - Residual

6437

earlier run (DOE Contract XJ-9-8170-1) in which the CdS substrates were heated to an excessive temperature. Impurity concentrations on the order of 1 ppma in both the InP film and Si substrate were found for several elements. To check the accuracy of the analysis, similar films were sent to two vendors. There is some doubt as to the validity of the analysis because the results of the second vendor showed approximately 20 ppma of Fe, whereas the present analysis showed none. Iron could have been present because iron screws were used in the system. Since then, the screws have been replaced with Mo. Mass spectrographic analysis by both vendors showed less than 1 ppma of Mo. Our mass spectrographic analyses have not been entirely consistent. Further studies should be undertaken on a more comprehensive basis with thicker films. Generally, the mobilities of our films are higher than expected if the total impurity concentrations that were detected were electrically active.

We also examined the purity of alternate sources of In and PH_3 for use in preparing the InP. We compared the electrical properties of film prepared with 99.999% purity PH_3 from Scientific Gas Products, and 99.9995% purity PH_3 from Phoenix Research Corporation, but found no difference. Therefore, we turned our attention to the In. Indium purchased from the Indium Corporation of America is nominally 99.9999% pure. A mass spectrographic analysis of In was undertaken to verify its purity and to determine what impurities could possibly be incorporated into the film. Table 3 shows two mass spectrographic analyses of two different batches of In by two separate vendors, Quad Group and AccuLabs. There is a large discrepancy between vendors for the same batch. For example, Quad Group finds high concentrations of Al in both batches, whereas AccuLabs does not. We did not pursue an extensive evaluation of the impurity content of our InP films and In source material because accurate results would require an extensive study beyond the scope of this program. Instead, we improved the quality of the system.

Table 3. Mass Spectrographic Analyses (ppma) of Indium

Element	5245 Quad Group	5245 Accu- Labs	7169 Quad Group	7169 Accu- Labs
Ga		5.2		
Si	2.2	1.8	2.5	3.1
Pb				0.3
Th		0.2		0.4
Mg	0.9	0.1	0.7	0.9
Al	4.9	0.1	4.3	0.8
S	1.1		1.1	
K	2.6		1.9	
Co	1.2		0.7	
Ge	2.7		1.4	

6437

2. $N^+/N/N^+$ Structures

We prepared $n^+/n/n^+$ layers of InP on (100) n^+ InP substrates at 350°C. N^+ films were grown from a 10%Sn:90%In alloy contained within the left deposition unit. N-type films were grown from pure In contained within the right deposition unit. The three-layer structure was fabricated by rotating the substrates from left to right to left during the same vacuum pump down cycle. Subsequently, the substrates were cleaved and SEM pictures were taken. The edgewise picture of the structure in Figure 14 shows that each of the layers was about 2- μ m thick. The electrical properties of the layers in such a structure could not be determined. But, in a previous run, n and n^+ layers deposited on separate semi-insulating substrates showed carrier concentrations of about 2×10^{16} and $2 \times 10^{18} \text{ cm}^{-3}$, respectively. These studies demonstrate that multilayer structures can be prepared by PRD.

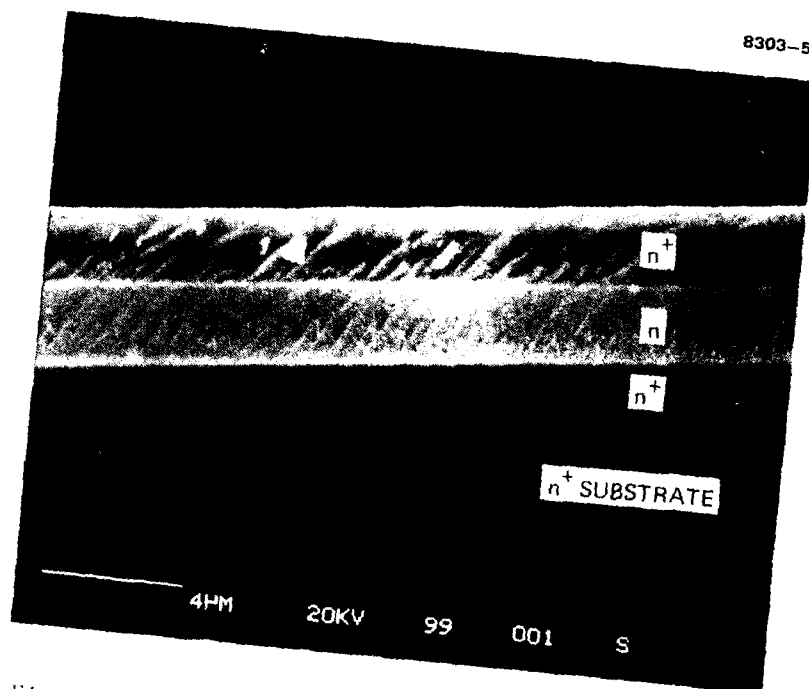


Figure 14. Multilayer $n^+/n/n^+$ structure of InP grown by PRD at 350°C on (100) InP substrate.

3. Large-Area Coatings

One advantage of the PRD approach is that the reactants are coevaporated from the same source. Consequently, it is easier to scale up the system for the deposition of large-area coatings having uniform thickness and composition. The dimensions of our PRD chambers permit deposition areas of 90 cm^2 . Normally, we prepared InP layers on 1 cm^2 substrates. During this program we deposited InP films on several 12 cm^2 InP substrates at 340°C (Figure 15). These large-area coatings were obtained with a 4-1/2-cm-diameter Knudsen cell, located 12 cm below the substrates. The reactants emanated from three holes, each 1/8 in. in diameter. An approximately $1 \mu\text{m}$ step, apparent at the corners of the InP wafers, and on the Mo disks, outlined the InP deposition. Our initial evaluation of these films showed them to be uniform in thickness ($\pm 0.2 \mu\text{m}$), and comparable in quality to layers prepared on smaller area substrates.

4. Discussion

We established reasonable control over the growth rates, uniformity, crystal perfection, and surface morphology of InP thin films prepared by PRD. Purity is the limiting factor in the development of this material for devices. Figure 16 shows the highest room temperature electron mobilities and the corresponding carrier concentration for unintentionally doped InP thin films prepared at different substrate temperatures by various vacuum thin-film technologies. Below a substrate temperature of 325°C , the transport properties of electrons are dominated by native defects. At higher temperatures, the electrical properties are probably dominated by impurities. Our highest mobilities

M12829



HUGHES
RESEARCH LABORATORIES

Figure 15. Broad area epitaxial deposition of InP onto InP wafers.

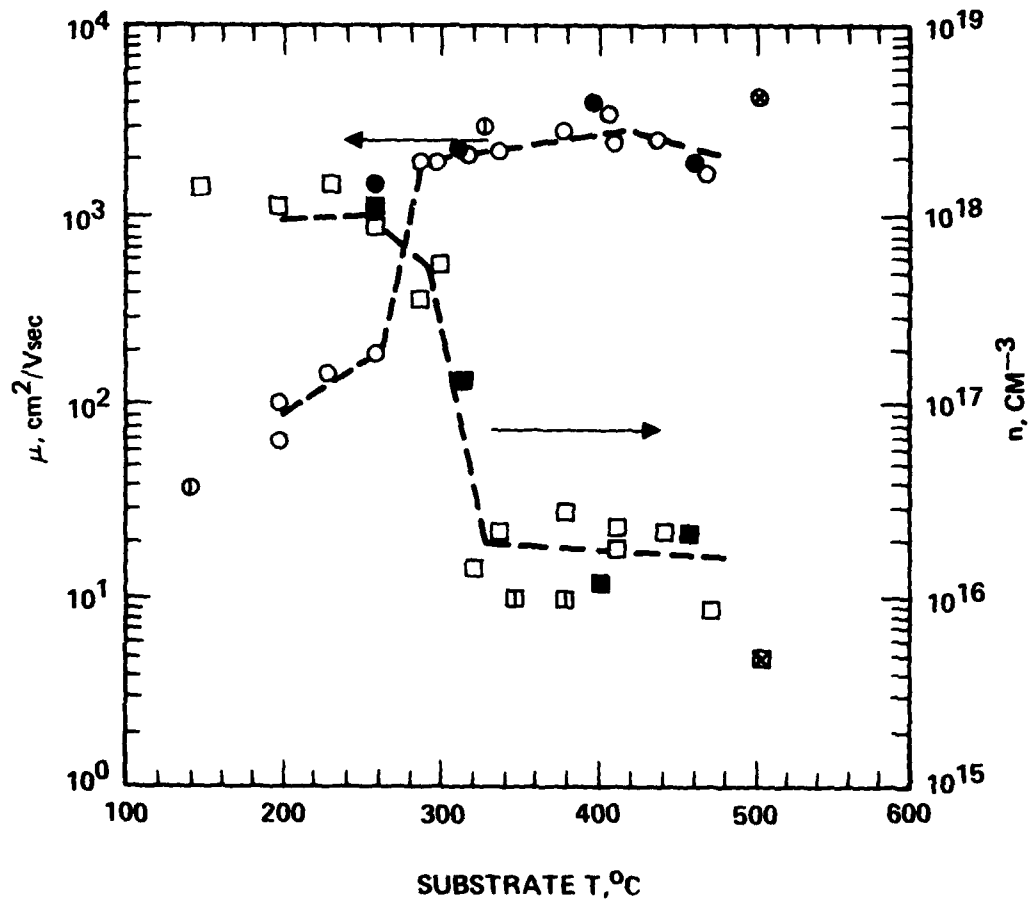


Figure 16. Unintentionally doped InP films prepared on InP substrates by vacuum technologies.

are plotted for several substrate temperatures. The highest mobility of a film prepared by PRD is better than that prepared by MBE. However, the mobility of InP prepared by LPMOCVD is even better. Only qualitative reasons can be given for these differences.

The environment of a molecular beam epitaxy system is certainly cleaner than that of a LPMOCVD system. If carbon is considered to be an electrically active impurity in InP, then the starting materials used in MBE are also cleaner than those in LPMOCVD. The fact that LPMOCVD has produced film of higher mobility than those by MBE would indicate that factors other than the purity of the starting materials and background cleanliness are more important. After certain limits on the purity of the starting material and background cleanliness have been established, further improvements in purity may only occur if the films are processed in a reactive atmosphere. Films prepared by LPMOCVD are prepared in a reactive atmosphere of H_2 . The purity of films prepared by LPMOCVD may be better than the purity of films prepared by PRD because of a significantly higher H_2 working pressure.

By varying the ratio of the flow rates of the group III metal organic compound and the group V hydride, the total concentration of electrically active impurities, $N_A + N_D$, may be minimized. This has been demonstrated with GaAs prepared by MOCVD. The effects of deviation from stoichiometry for the growth of InP by MOCVD, LPMOCVD, and MBE are not documented in the literature. During this program, we did not intentionally vary the ratio of the indium flux to the phosphine flow rate (F_{In}/F_{PH_3}) to minimize $N_A + N_D$. However, subsequent to our experimental results, we did attempt to make such a correlation between F_{In}/F_{PH_3} and the electrical data. We did not find a correlation, possibly due to several reasons.

First, in addition to In evaporated from the Knudsen cell, residual In was also evaporated from other hot regions near the source. Since the quantity of residual In incorporated into the film may have varied from run to run, the purity of In in the film may not have been constant. Second, it was necessary to alternate this study with another study which required volatile n- and p-type dopants in the system. Excessive

concentrations of residual dopants may have been in our system during our growth of unintentionally doped InP. Third, we had no assurance that the partial pressures of residual noncondensable dopant gases were reasonably constant. Because the system was not completely supported by this program, it was often cleaned resulting in different levels of C and O. At the ionization gauge outside of the deposition chamber, the CO and O₂ pressures varied over ranges up to 10⁻⁷ and 10⁻⁹ Torr, respectively.

As discussed earlier, we observed an increase in the mobilities after the system was modified. Although we obtained room temperature mobilities as high as 4000 cm²/Vsec, mobilities only in the 2000 to 3000 cm²/Vsec range are reproducible. Subsequent to the modification, we again used two different sources of PH₃; no correlation between the PH₃ source and electrical properties was found. As an alternate source of In, we intended to grow InP films using In from the decomposition of (C₂H₅)₃In. (C₂H₅)₃In was decomposed in the Knudsen cell, but InP films were not grown.

In order of decreasing importance, the residual gases and potential sources of contaminants in the system are: CO, O₂ and H₂O. CO and H₂O are observed during outgassing of the source and are present at high pressures during film deposition. Unfortunately, the mass spectrographic analyses were not sensitive enough to determine accurate concentrations of C and O. We have considered the vacuum growth of InP in the presence of PCl₃. Growth in the presence of the halides should eliminate O and reduce C by formation of the volatile Group IV tetrachlorides. To obtain InP film with improved transport properties it will be necessary to (1) modify the source to reduce the source of carbon, (2) undertake growth in a more reactive environment to further reduce the concentration of C and O, (3) introduce controlled concentrations of C and O to determine their effect on the transport properties of InP, and (4) establish the relationship between P_{PH_3}/F_{In} and the electrical properties.

B. InGaAs, InGaP AND InGaAsP

To extend the flexibility of the PRD system, we prepared and evaluated several ternary and quaternary compounds. Films were grown on sapphire to check their composition with a microprobe, and on semi-insulating (100) InP and GaAs substrates to check their degree of epitaxy with an x-ray Read camera, and to evaluate their electrical properties with Hall measurements. All films were grown at about 350°C. First, we attempted to grow GaP by replacing the In in the Knudsen cell with Ga. However, we grew InGaP. Although we had cleaned In from the parts in the deposition chamber which directly view the Knudsen cell, residual In located in remote parts of the deposition unit was reevaporated onto substrates. Because of the significantly lower vapor pressure of Ga, a much higher source temperature is required to attain reasonable Ga deposition rates. Consequently, because we underestimated the temperature of parts more remotely located from the Knudsen cell, the residual In was also deposited onto the substrate. In the intentional growth of GaP, the films contained a small percentage of In. Likewise, when GaAs was grown by incorporating an AsH₃ source, the films contained a small percentage of In. However, this source of In did not significantly affect the composition for alloys of high In content.

First, two runs were made to lattice match InGaP to GaAs substrates. InP substrates were also present in an adjacent deposition position. Using vapor pressure data of In and Ga, the appropriate In/Ga ratio was determined. Corresponding charges of In and Ga were then added to the Knudsen cell. In the first run, a 5% lattice mismatch was obtained between the film and the GaAs substrate. The epitaxial quality, as determined by the x-ray Read camera, was poor. After changing the In/Ga ratio, the second run resulted in a 0.3% lattice mismatch between the InGaP and GaAs. The x-ray Read camera found different lattice constants for films deposited on InP versus the GaAs substrates, possibly because the film in this run was only 0.7 μm thick, and the substrates induced different degrees of strain in the films. The calculated and measured

values of the lattice constants were in reasonable agreement. The calculated value was determined by measuring the composition by microprobe analysis of films prepared on sapphire substrates, and relating that composition to lattice constants from published data.

In a single run, we attempted to grow $\text{In}_{0.53}\text{Ga}_{0.47}\text{As}$ on lattice matched InP substrates. Microprobe analysis showed the group III constituent of these films to contain 47% In and 53% Ga. This corresponds to a 1.3% lattice mismatch.

A single run was also undertaken to lattice match InGaAsP on InP substrates. Surprisingly, only a 1.9% lattice mismatch was achieved. GaAs substrates were also included in this run. A 1.9% lattice mismatch was also achieved on the GaAs substrates. These lattice-matching studies are summarized in Table 4.

Hall measurements were made on these films, and are included in Table 4. All films were n-type. In the InGaP studies both the In/Ga ratio and the lattice constant of the substrate (i.e., InP or GaAs) were varied, offering a wider range of lattice matching. Electrical measurements of films showing good crystalline quality by x-ray Read analysis resulted in higher mobilities (i.e., $\mu_n > 1,000 \text{ cm}^2/\text{Vsec}$), whereas films containing polycrystalline components resulted in lower mobilities (i.e., $\mu_n < 400 \text{ cm}^2/\text{Vsec}$). The higher mobilities may have been limited by intrinsic defects introduced by the lattice mismatch.

Within the limits of the x-ray Read camera, x-ray analysis showed the quality of the higher mobility films to be comparable to that of the substrates. Although the lattice mismatch was the same for InGaAsP on GaAs and InP films, the mobility of the film deposited onto GaAs was higher. The reason for this is not known. However, the composition of the InGaAsP films was much closer to GaAs than to InP.

In summary, correlations between lattice mismatch and mobility were found. However, considering the limited extent of the study and possibility of impurity contamination, we are reluctant to interpret

the mobility data in more detail. We conclude that it is easy to lattice match ternary and quaternary III-V compounds on appropriate substrates to within 1% by PRD. With further refinements, and elimination of residual In in the deposition chamber, it is not unrealistic to expect to lattice match these films to within 0.1%.

Table 4. Characteristics of Epitaxial III-V Ternary and Quaternary Lay Prepared by PRD at 350°C

Deposition	Substrate	Thickness, μm	x	1-x	y	1-y	Lattice Constants A		Lattice Mismatch	Electron Mobility cm^2/Vsec
							CAL	X-Ray		
$\text{In}_x\text{Ga}_{1-x}\text{P}$	GaAs	0.68	0.41	0.59			5.69	5.65	0.3%	1,100
	InP							5.67		
$\text{In}_x\text{Ga}_{1-x}\text{As}$	InP	1.20	0.43	0.57			5.77	5.79	1.3%	1,401 1,060
$\text{In}_x\text{Ga}_{1-x}\text{As}_y\text{P}_{1-y}$	GaAs	1.20	0.38	0.62	0.92	0.08		5.76	1.9%	1,097
	InP								1.9%	580

SECTION 4

GaAs BY LPMOCVD

A. EXPERIMENTAL RESULTS

Of the 10 runs undertaken, 5 were made on sapphire substrates to establish growth conditions. Epitaxial films were deposited on semi-insulating (100) GaAs in the last five runs. In the first two runs on GaAs substrates, films were grown near the three-phase region, which consists of GaAs vapor coexisting with GaAs and Ga. In several preliminary runs on sapphire, GaAs was grown with large excesses of Ga. The AsH_3 to TMGa flow rate ratio ($F_{\text{AsH}_3}/F_{\text{TMGa}}$) was slightly increased to about 0.9. (For convenience, we shall refer to these growth conditions as a flow rate ratio of one.) Films were then prepared at a $F_{\text{AsH}_3}/F_{\text{TMGa}}$ of 3.7. (For convenience, we refer to growth at these conditions, as a flow rate ratio of four.) The crystal perfection of the films was examined by selective area electron diffraction (SAD), scanning electron microscope (SEM), x-ray Read, and x-ray topographs. The thickness of the layers were determined by SEM, staining cleaved sections, and sputter ion mass spectrometry (SIMS). The electrical properties were surveyed with hot probe and Hall measurements. The impurity content of the films was examined by SIMS. The extent of the evaluation of GaAs thin films prepared in each run are summarized in Table 5.

1. Crystal Perfection and Morphology

For the runs at $F_{\text{AsH}_3}/F_{\text{TMGa}}$ of one, a hillock formed near the center of the wafer where impingement of the gases occurred. Staining showed the hillocks to be about 30 μm thick. The top surfaces were about 6 μm thick near the hillock, tapering to about 3 μm at the edges. Coverage also occurred on the bottom of the wafers because of a slight bow in the pedestal.

Table 5. Characterization of MOCVD GaAs Films

Run	$\frac{F_{AsH_3}}{F_{TMGa}}$	SAD	SEM	EDAX	X-Ray Read	X-Ray Topograph	Staining	Hot probe	Hall	SIMS
1	One	W	W	W	2	-	S	W	3	2
2	One	W	W	T	1	-	S	W	2	1
3	Four	W	W	-	-	-	S	W	2	-
4	Four	W	W	-	1	1	S	W	3	1
5	Four	W	W	-	-	-	-	W	2	1

W - Entire wafer analyzed
 S - Section of wafer analyzed
 1,2,3,4 - Number of samples measured

Staining showed films on the bottom of the wafers to be about 2 μm thick. SIMS showed the films at the peripheral at the top and backside of the wafers to be about 3 μm thick. (In the following discussion refer to Figure 8 to determine positions on the wafer where the thin film was deposited.) Edgewise SEM pictures (Figure 17) of the cleaved structure showed the films to be about 50 μm and 5 μm thick at Positions 1 and 4, respectively. Films prepared at $F_{\text{AsH}_3}/F_{\text{TMGa}}$ of four did not contain hillocks, and were about 3 μm thick.³ SIMS results confirmed these thicknesses.

Scanning electron microscope pictures showed a wide range of surface features. Figure 18 shows SEM photographs of the GaAs thin film at different positions on the substrate in Figure 8. Within the hillock, and presumably in the direct stream of the gases (Position 0), a crusty GaAs deposit decorated with free Ga and black deposits, probably carbon, was found. The presence of Ga confirmed that growth occurred at the three phase boundary. The quality of the films improved at increasing distances away from the direct flow of the gases. At Position 1, the SEM shows only the crusty GaAs layer. Faceting is evident at Position 2. At Position 3, the onset of smooth layer growth was found. At Position 4, surfaces free from defects at magnifications up to 100,000x were found. The backside of the wafer from Run 2 was also examined. The quality of the layer was most typical of Position 4.

Films prepared at a $F_{\text{AsH}_3}/F_{\text{TMGa}}$ of four were faceted. In contrast to the highly reflecting surfaces obtained at a $F_{\text{AsH}_3}/F_{\text{TMGa}}$ of one, these layers were characterized by bands having alternate highly reflecting and moderately reflecting surfaces. The width of these bands was about 8 mm. Figure 19 shows typical SEM patterns of highly reflecting (top) and moderately reflecting (bottom) regions. The smoothest regions in the three runs at a $F_{\text{AsH}_3}/F_{\text{TMGa}}$ of four were rougher than the smoothest region for the samples prepared at $F_{\text{AsH}_3}/F_{\text{TMGa}}$, where higher TMGa flow rates were used. This is not

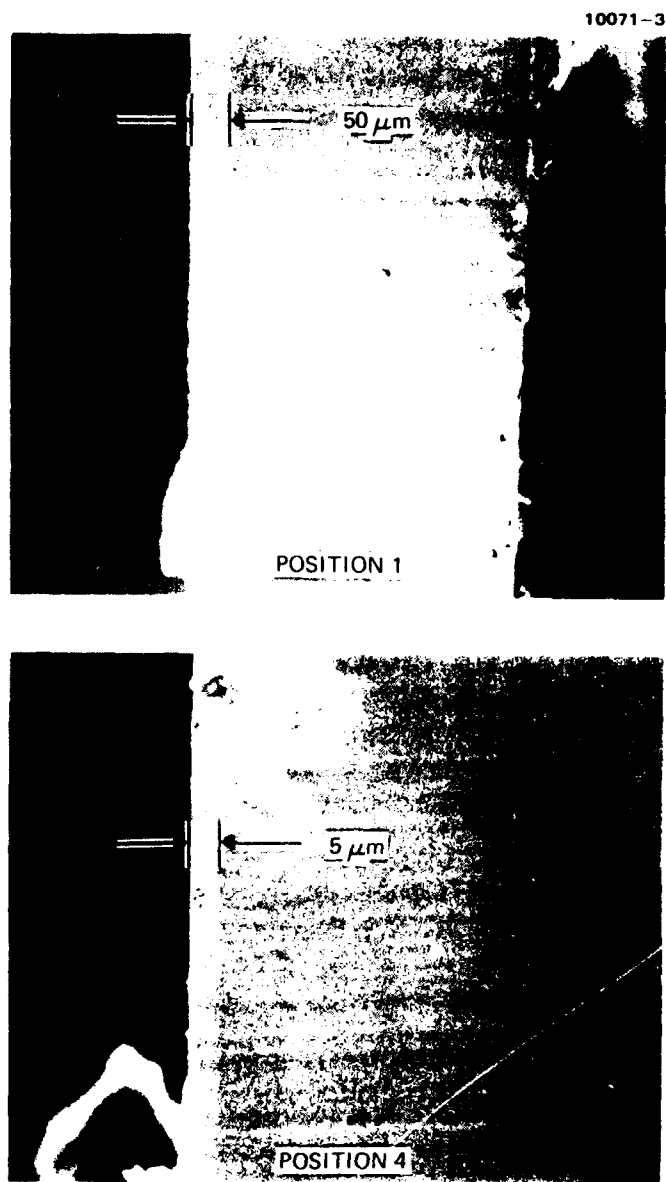


Figure 17. SEM edge view of GaAs film on cleaved (100) GaAs substrate.

10071-2

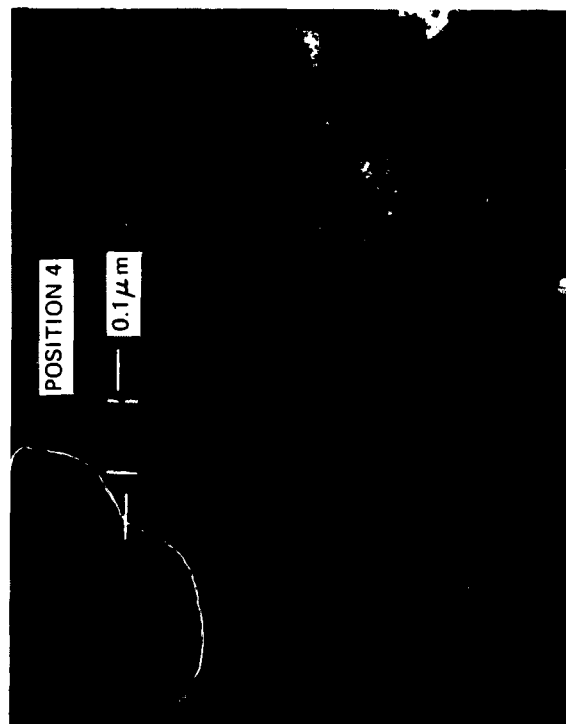
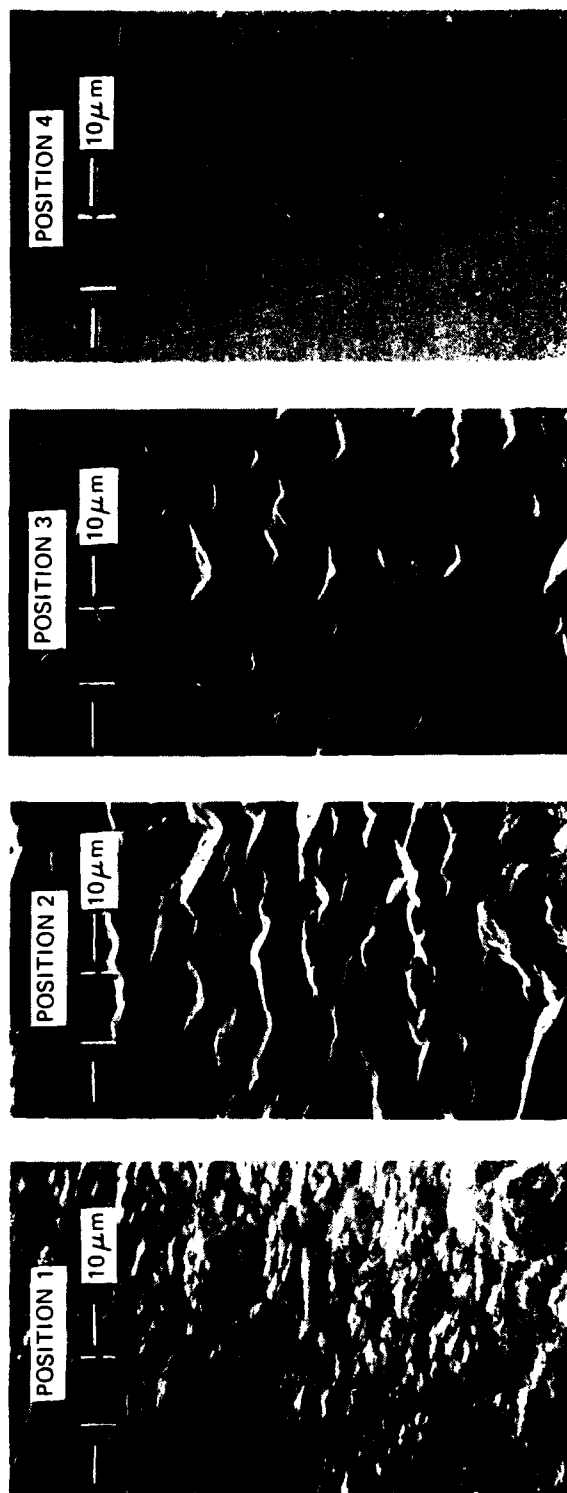


Figure 18.
SEM photographs at different positions of GaAs
film prepared on (100) substrate at $\text{FAsH}_3/\text{FTMGa}$
of one.

10429-1

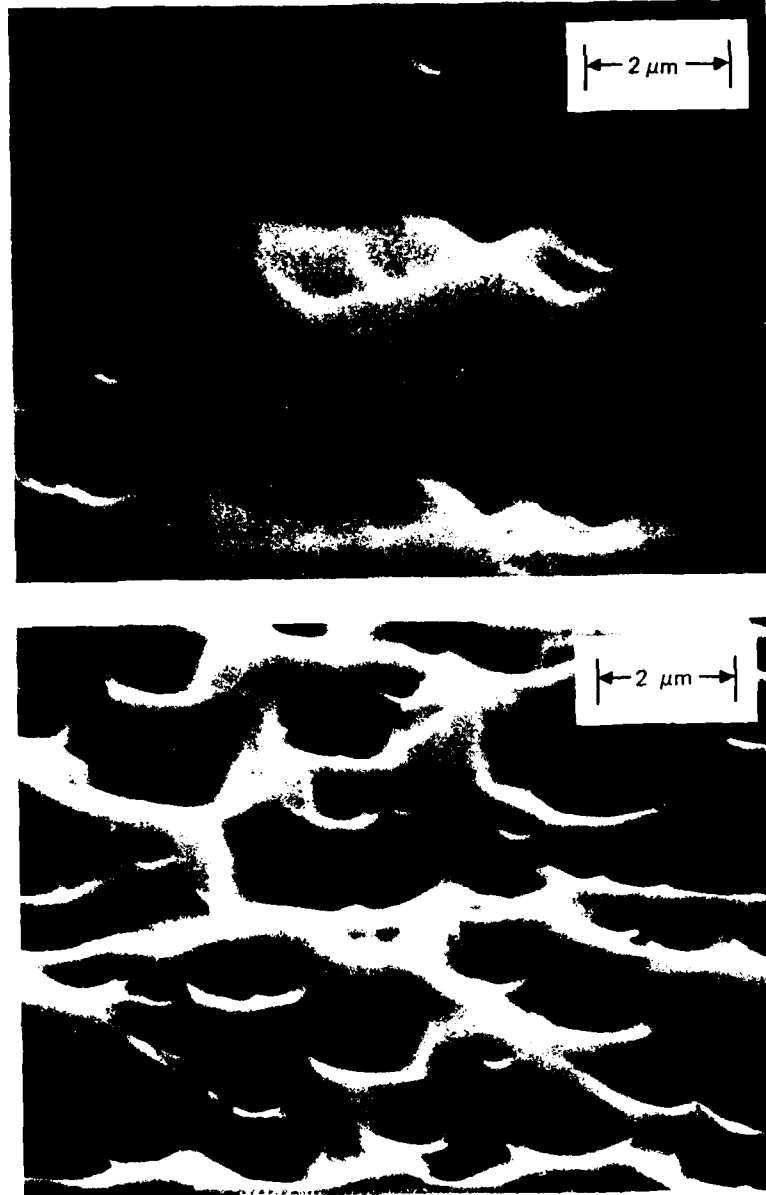


Figure 19. SEM picture of epitaxial GaAs exhibiting a dull luster (top) and no luster (bottom) as viewed by the unaided eye.

understood, but might be associated with differences in the crystallographic orientation, or the value of $F_{\text{AsH}_3}/F_{\text{TMGa}}$ used. The orientation of wafers used in these studies is $^{3(100)}$. A slight unintentional orientation toward (110) in the initial runs could have improved the morphology. It is possible that growth with excess Ga could result in a form of solvent growth with different surface kinetics.

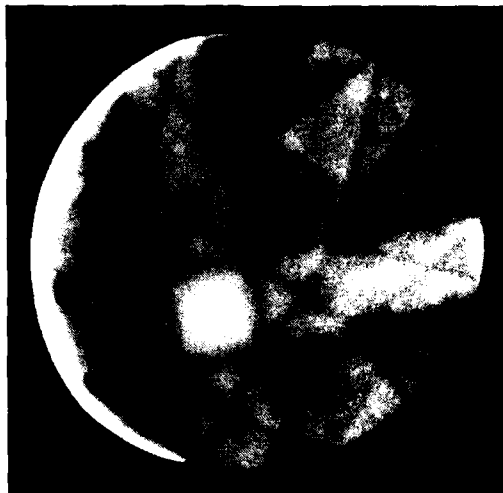
A survey of all the films with SAD indicated single-crystal epitaxy. Except at the hillocks, SAD showed uniform channeling patterns. Figure 20 shows electron channeling pictures of (top) the GaAs epitaxy prepared by LMOCVD, and (bottom) a semi-insulating GaAs wafer similar to one used as the substrate. No difference was apparent between the epitaxy and the substrate material. Also, there was no difference in channeling patterns across a wafer, among the five wafers, or between the wafers and substrates. Although the channeling pattern is not a precise tool for evaluating the quality of the layers, it did show that except for the hillocks, epitaxy had been achieved over the entire wafer and that an amorphous layer of significant thickness was not present.

X-ray Read pictures of regions characteristic of Position 2 showed both spots and rings, characteristic of both single-crystal and polycrystalline materials. X-ray Read pictures (Figure 21) at Position 4 and the bottom of the wafer showed only spots characteristic of single crystalline material. Even though faceting was present, x-ray Read pictures of films prepared as $F_{\text{AsH}_3}/F_{\text{TMGa}}$ of four show spots characteristic of single-crystal material. In an x-ray topograph of this material no defects were visible.

2. Electrical Properties

Van der Pauw measurements were made on 10 samples. At least two samples were measured from each of the four runs. These samples were

10291-1



10291-2

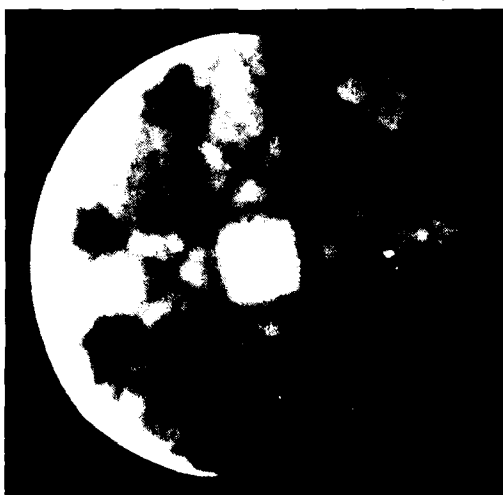


Figure 20.
Electron diffraction chan-
neling picture for 20 keV
electrons in (top) epitaxial
GaAs prepared by LPMOCVD
and (bottom) semi-insulating
(100) GaAs substrates.

10071-4

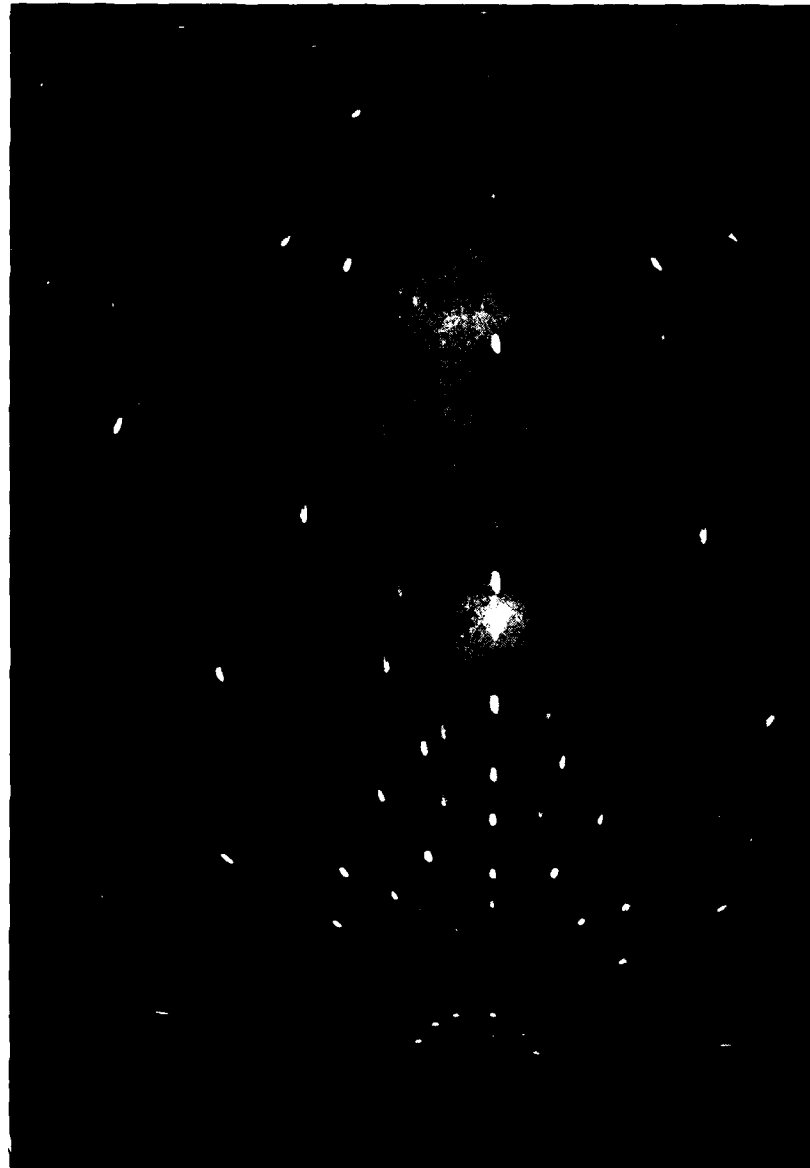


Figure 21. X-ray Read photograph of GaAs film characteristic of Position 4 in Figure 18.

characteristic of positions on the wafer having the best crystal perfection, and as little faceting as possible. Electrical data were plotted in two ways. First the hole concentration was plotted versus $F_{\text{AsH}_3}/F_{\text{TMGa}}$. Data in Figure 22 represents the average hole concentration for $F_{\text{AsH}_3}/F_{\text{TMGa}}$ at one and four. For the work of Seki et al. we have included two curves, each of these curves representing growth using a different metal organic source, and presumably a different concentration of residual impurities. The three phase boundary in this figure refers to our work. Because of differences between reactors it is not clear how far away from the three phase boundary the work of Seki et al. was undertaken. The room temperature hole mobility was also plotted, versus the hole concentration (Figure 23). Our data points represent the highest mobility for each of the four runs. Other p-type data from LPMOCVD were not available, so MBE data were used for a comparison. Solid and open data points are characteristic of intentionally and unintentionally doped material, respectively. The solid line is the envelope of the highest mobilities prepared by vacuum technologies. The extrapolation of a mobility of $450 \text{ cm}^2/\text{Vsec}$ at a hole concentration of 10^{14} cm^{-3} represents the best p-type material in GaAs.

Figure 24 and Figure 25 show respectively the hole concentration and mobility as a function of temperature for the highest mobility sample at $F_{\text{AsH}_3}/F_{\text{TMGa}}$ of four. These results were obtained from a Van der Pauw sample 7 mm on a square (dashed curve). The sample was then slotted to form a cloverleaf (solid curve). The total concentration of electrically active centers, $N_A + N_D$, from the cloverleaf sample is $2.4 \times 10^{16} \text{ cm}^{-3}$. There is reasonable uniformity across the sample. If we compare the square sample with the cloverleaf sample there is little difference in the shape of the mobility and concentration curves. The electrical measurements sample areas of 40 mm^2 and 10 mm^2 for the square and cloverleaf samples, respectively.

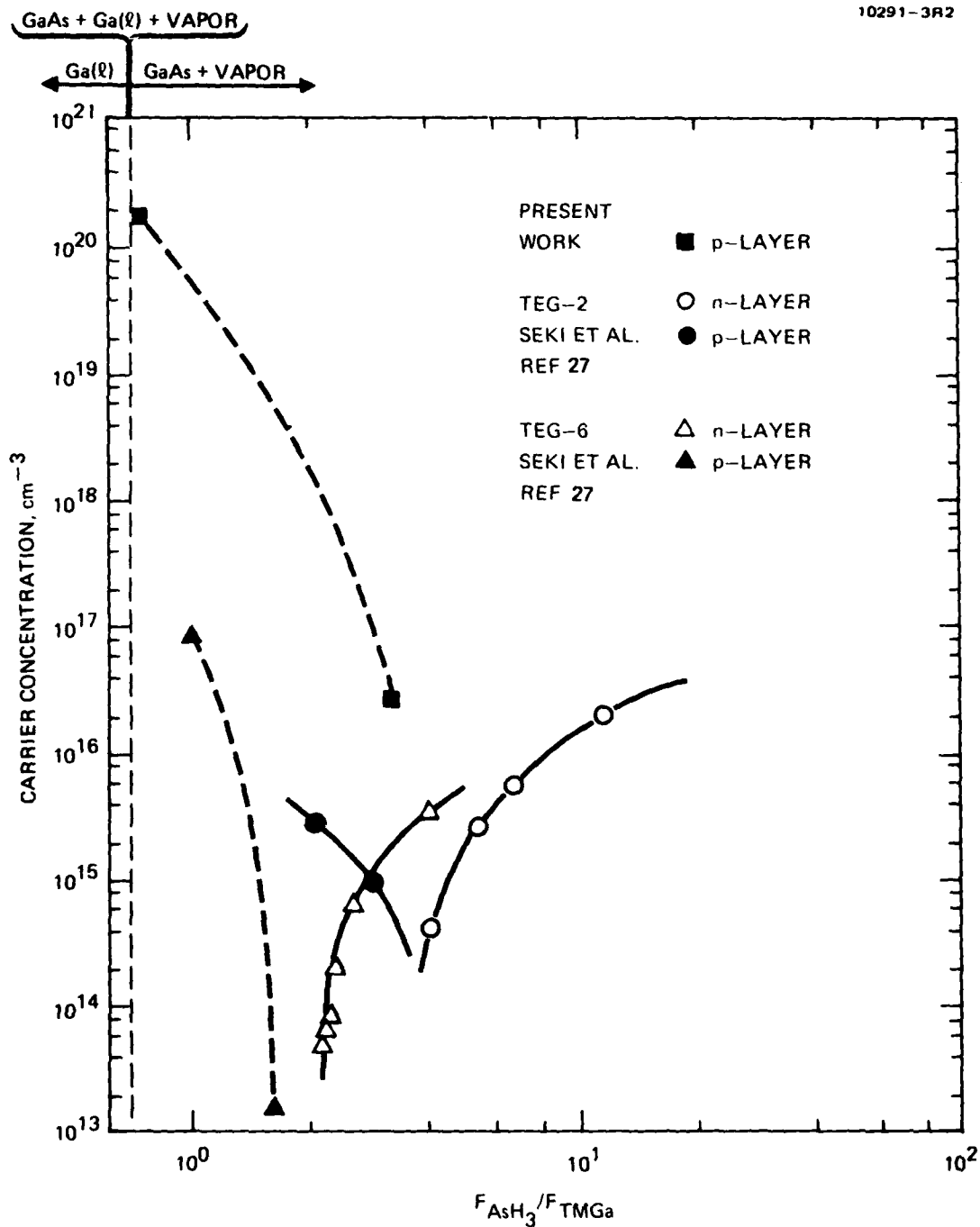


Figure 22. Dependence of type and carrier concentration on mole fraction ratio of Ga and As for GaAs prepared by MOCVD.

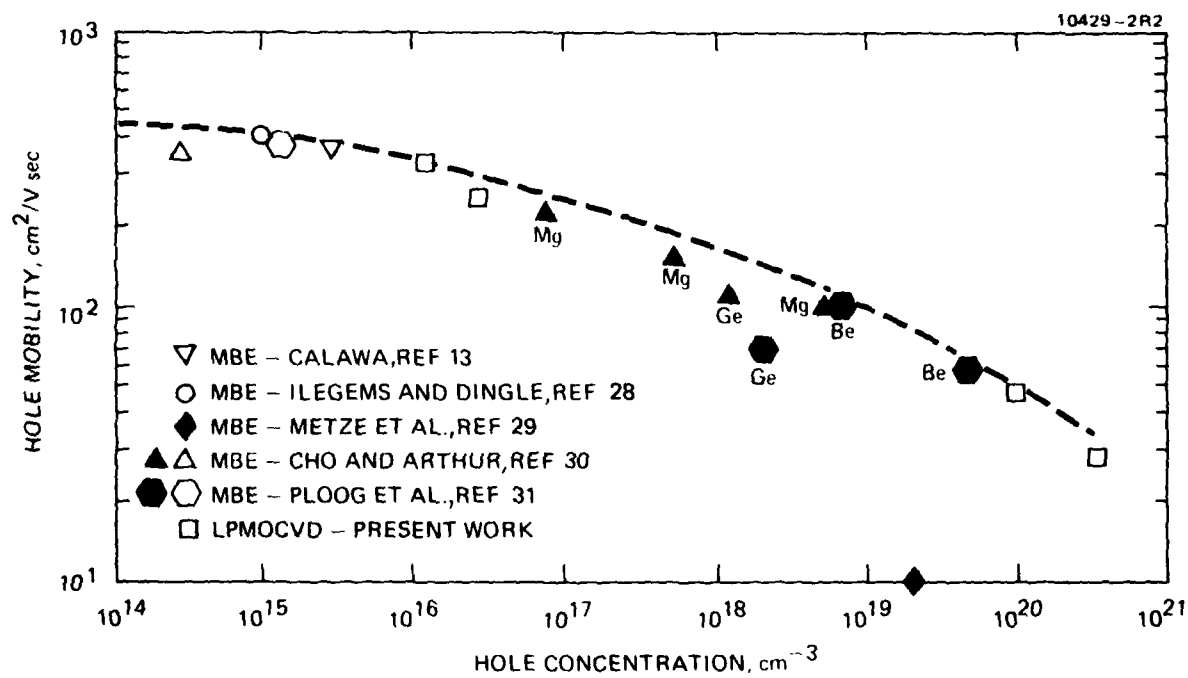


Figure 23. Room temperature hole mobility versus carrier concentration for unintentionally doped (open data points) and intentionally doped (solid data points) GaAs thin films prepared by vacuum technologies. These data and LPE data were used to construct an envelope (dashed line) of nearly uncompensated material.

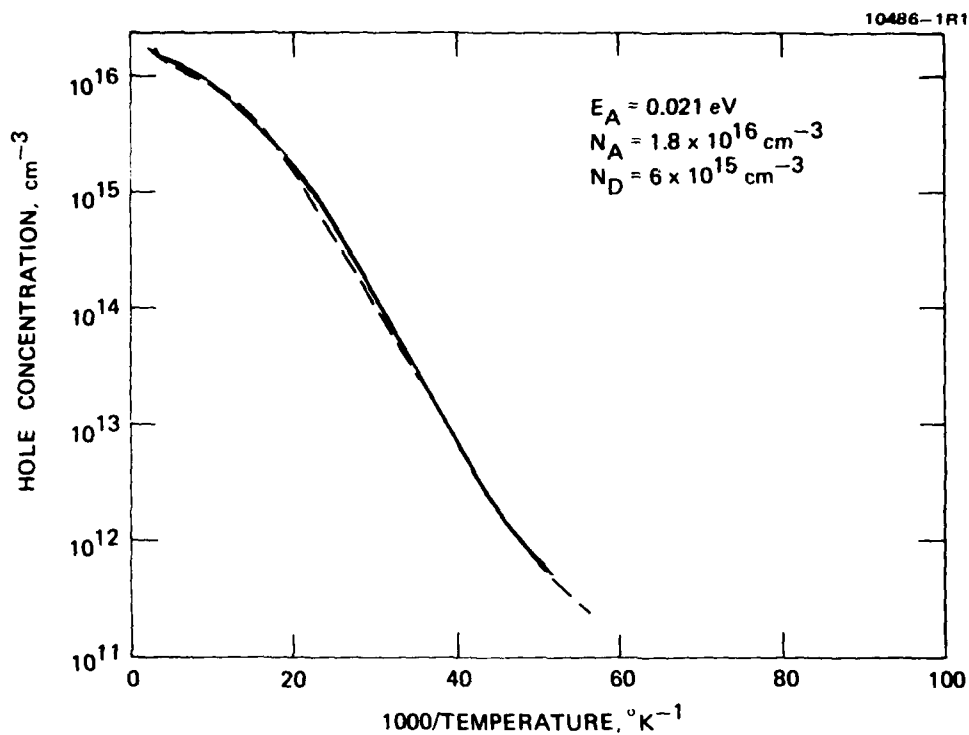


Figure 24. Hole concentration versus reciprocal temperature for square (dashed) and cloverleaf (solid) Van der Pauw samples of GaAs prepared by LPMOCVD at $F_{\text{AsH}_3}/F_{\text{TMGa}}$ of four.

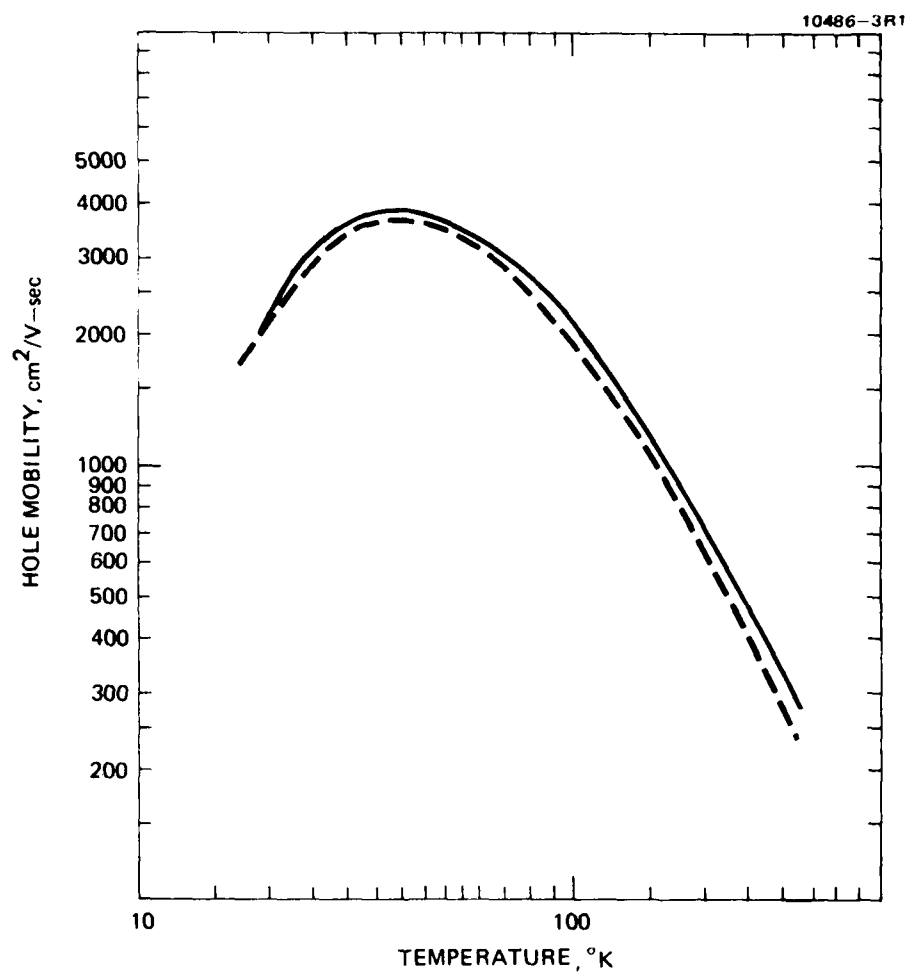


Figure 25. Hole mobility versus temperature for square (dashed) and cloverleaf (solid) Van der Pauw samples of GaAs prepared by LPMOCVD at $F_{\text{AsH}_3}/F_{\text{TMGa}}$ of four.

3. Impurity Analyses

SIMS profiles were taken of layers prepared at flow rate ratios of both one and four. Profiles were taken with a Cameca IMS-3f micro-analyzer (Charles Evans and Associates, San Mateo, California). Samples were sputtered using Cs^+ ion bombardment, while monitoring negative secondary ions. In Figures 26 through 29, samples were sputtered at 40 \AA/sec . In Figures 30 and 31, samples were sputtered at 115 \AA/sec . Profiles are displayed in terms of ion intensity only. Conversion of ion intensity in counts/second to concentration is accomplished with the following equation:

$$\text{Concentration (atoms/cm}^3\text{)} = \frac{\text{Ion Intensity} \times \text{Sensitivity Factor}}{4.8 \times 10^7 \text{ (counts/sec)}} \quad (1)$$

Sensitivity factors for different impurities are listed in Table 6.

Figure 26 is a SIMS analysis of the substrate, and probably represents background contamination from the SIMS system, especially for ^{16}O , ^{32}O , ^{12}C , and ^1H . Figures 27, 28 and 29 represent data taken at $F_{\text{AsH}_3}/F_{\text{TMGa}} = 1$. Figure 27 represents data taken in Run 1. Figures 28 and 29 represent data taken in Run 2 at different positions on the same sample. The peaks at about $3 \mu\text{m}$ represent the interface between the layer and the substrate. Charles Evans and Associates relate these peaks to differences in the sputtering rates at the interface, and not to spikes in the impurity profiles. Profiles for the two positions on the same sample, and for the second sample show similar distributions for most of the elements. In Figure 27 the ^1H distribution falls off rapidly from the surface. This is probably an instrumental effect, and not characteristic of the sample. The carbon distribution is uniform and well above background. From Equation 1, the carbon concentration is about $2 \times 10^{19} \text{ cm}^{-3}$. The oxygen profiles vary. In Figure 27 there is no oxygen above the background level of 10^{18} cm^{-3} . In Figure 28

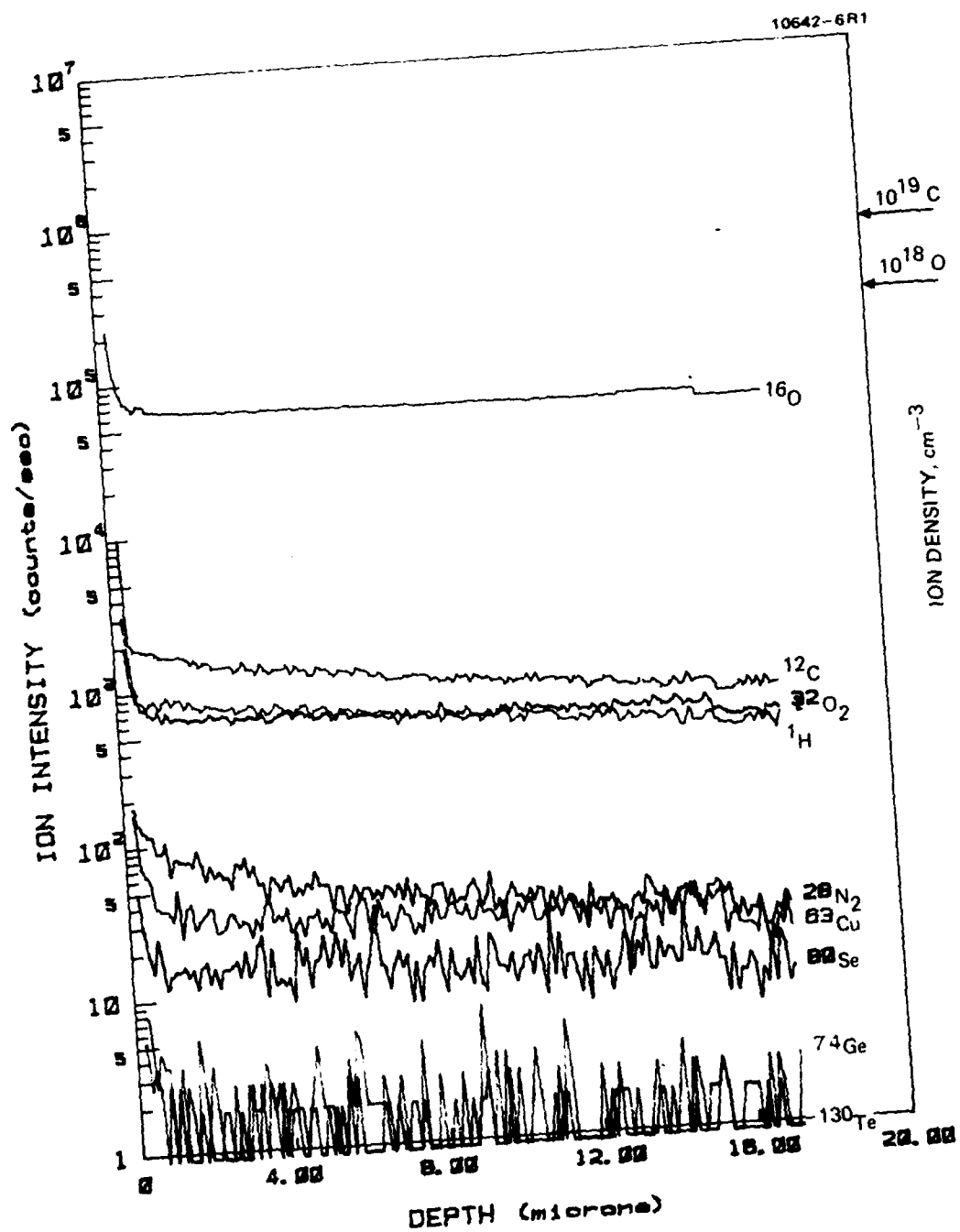


Figure 26. SIMS analysis of GaAs substrate.

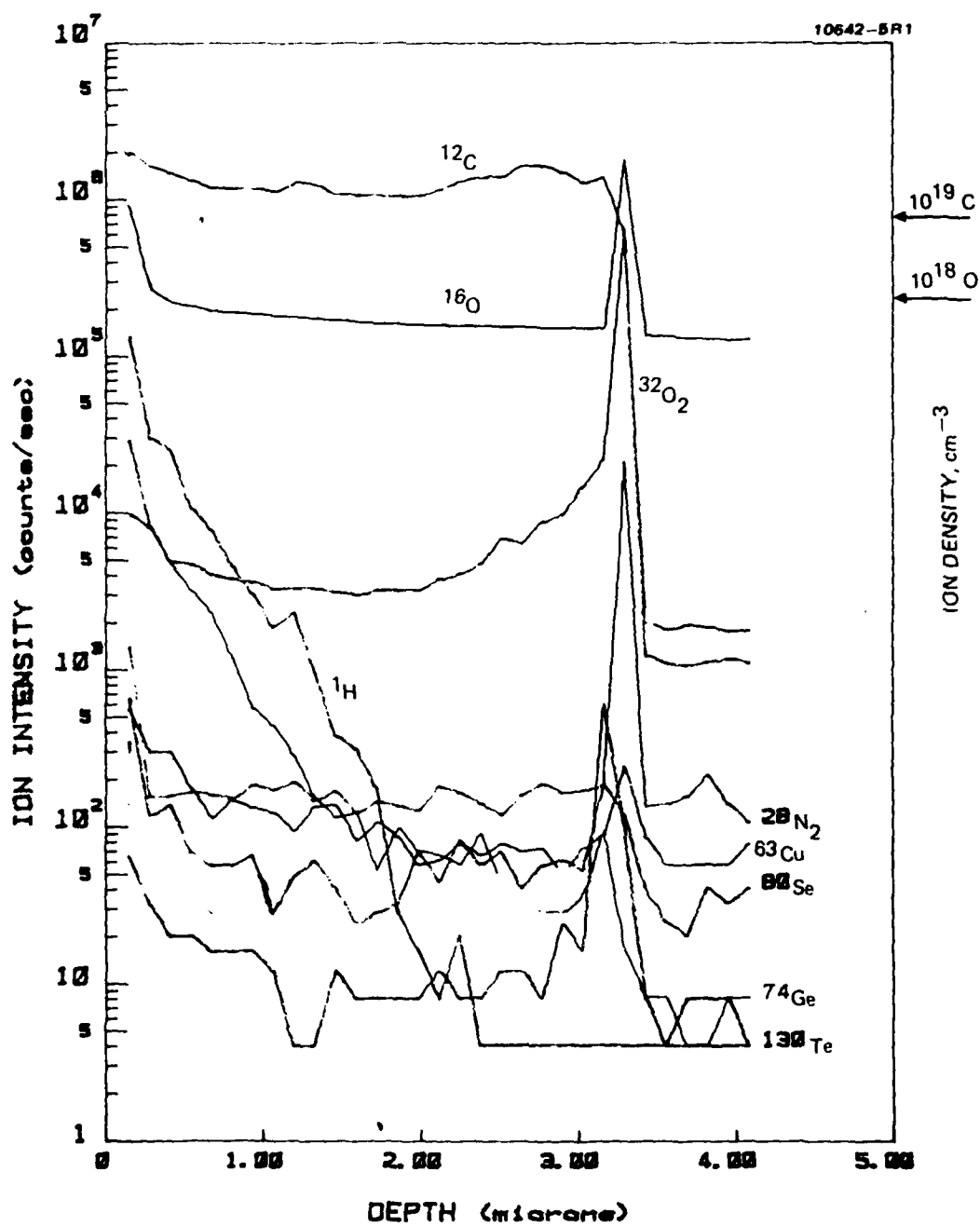


Figure 27. SIMS data taken on the GaAs thin film prepared in Run 1 at $F_{\text{AsH}_3}/F_{\text{TMGa}} \approx 1$.

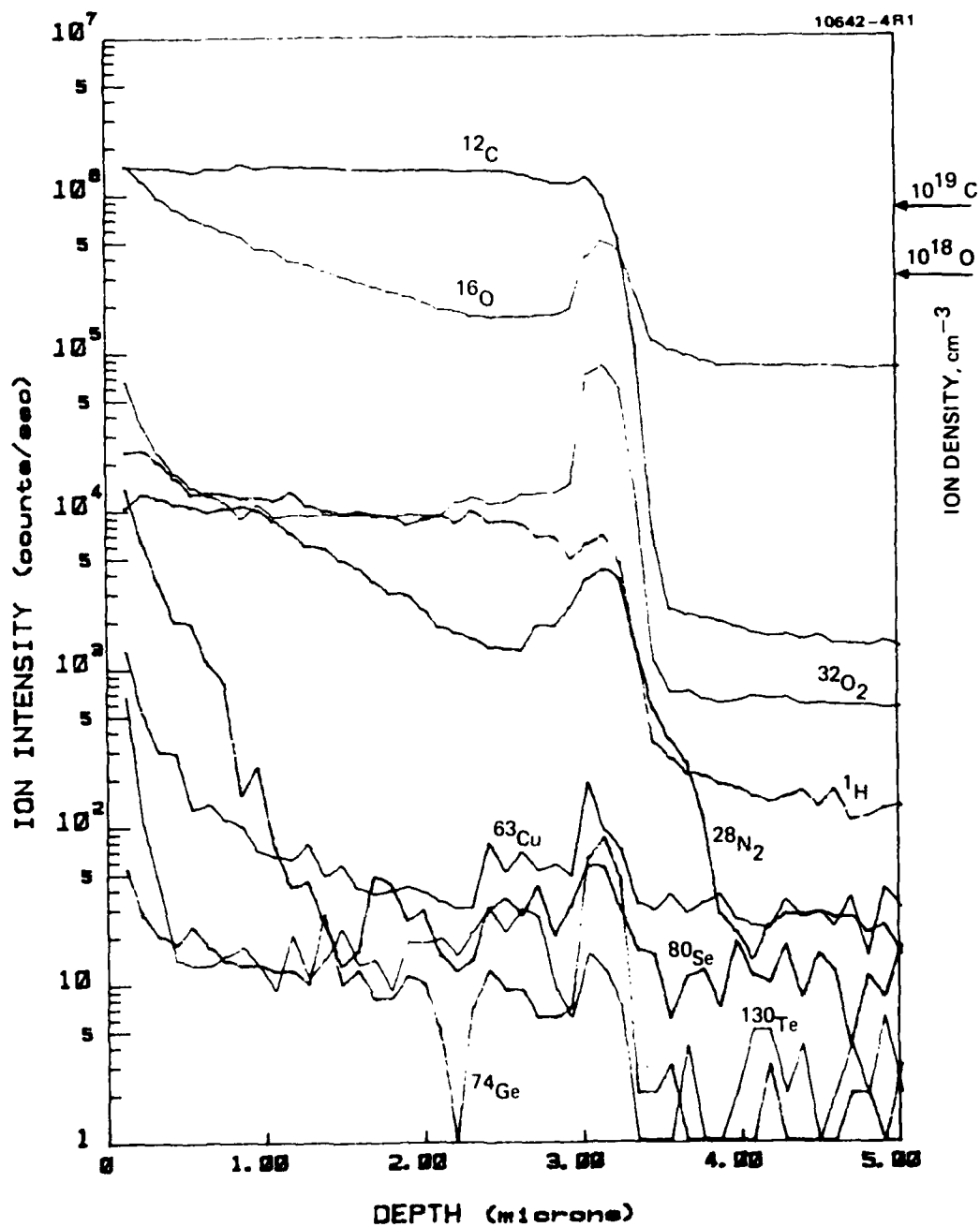


Figure 28. SIMS data taken of the GaAs film prepared in Run 2 at $F_{\text{AsH}_3}/F_{\text{TMGa}} \approx 1$.

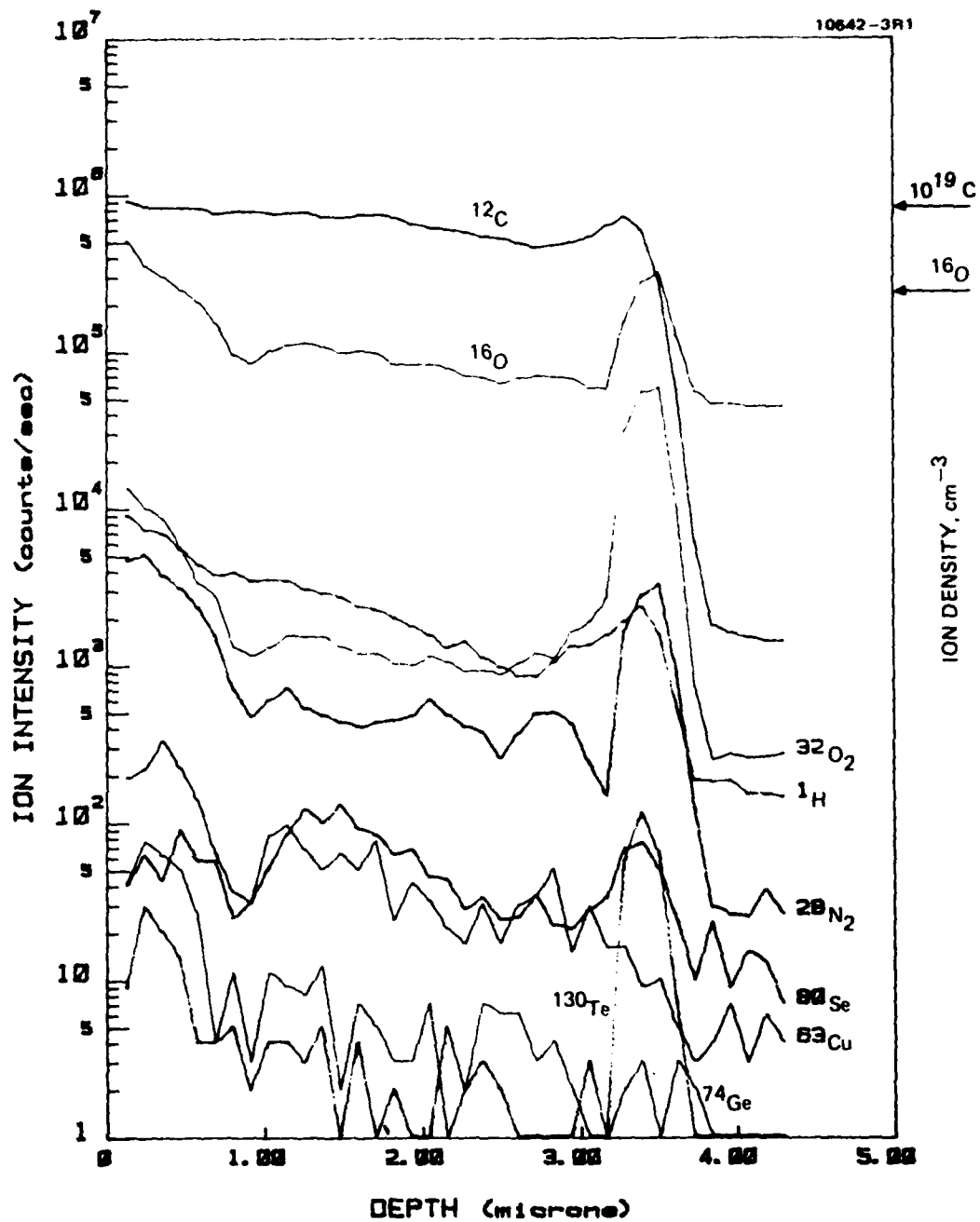


Figure 29. SIMS data taken on the same GaAs film as in Figure 28 but at a different position.

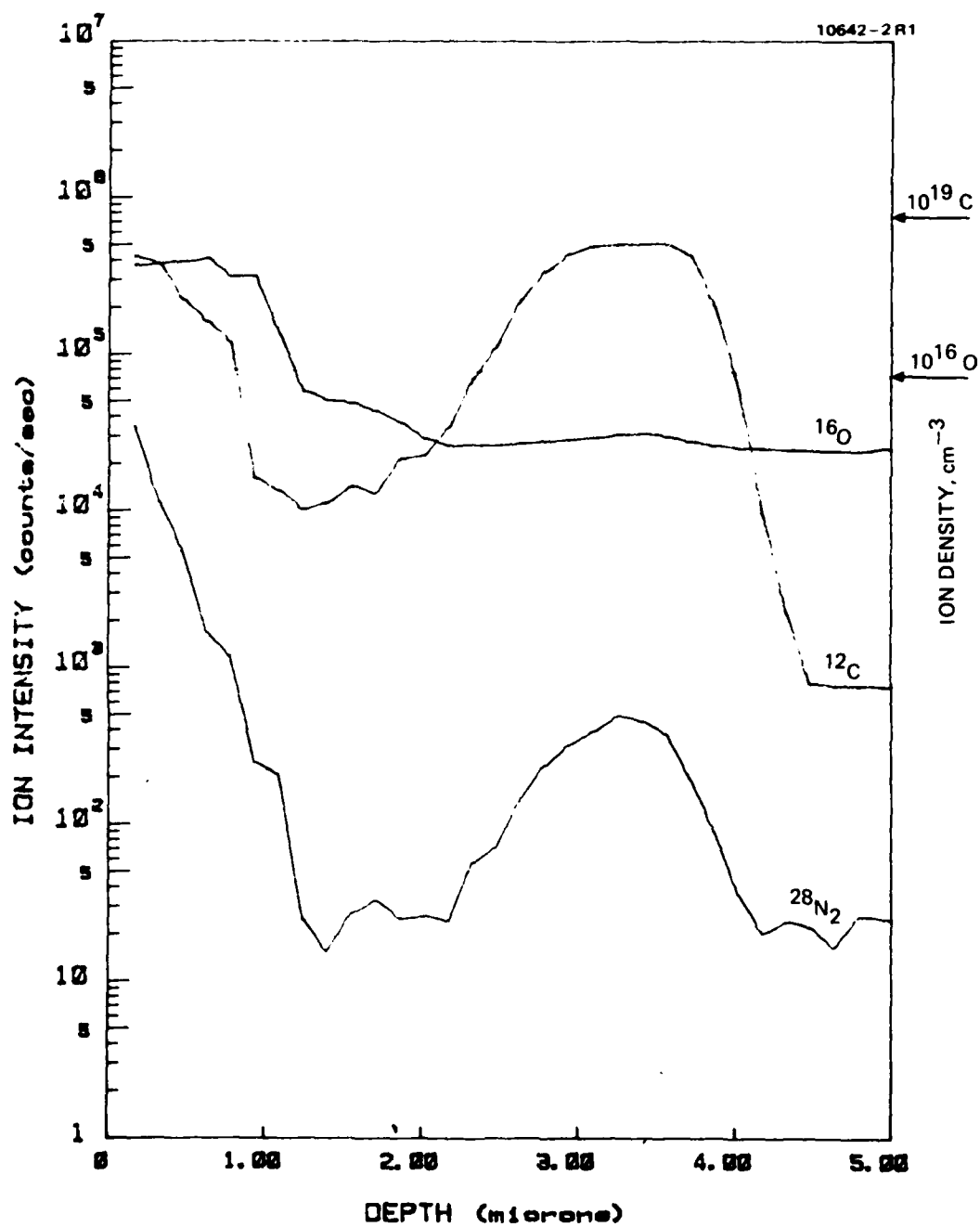


Figure 30. SIMS data taken in the GaAs film prepared in Run 4 at $F_{\text{AsH}_3}/F_{\text{TMGa}} \approx 4$.

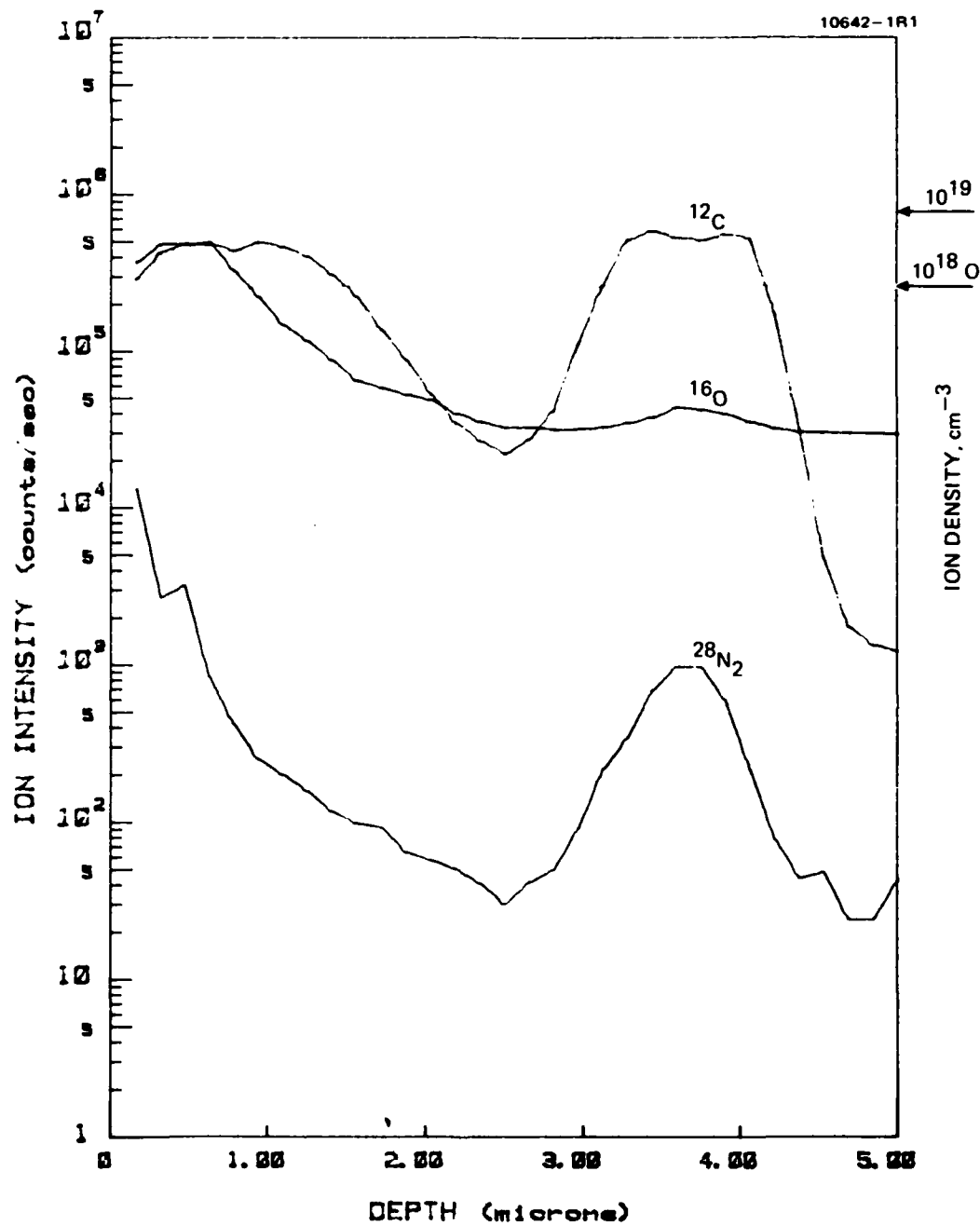


Figure 31. SIMS data taken of the GaAs sample prepared in Run 5 at $F_{\text{AsH}_3}/F_{\text{TMGa}} \approx 4$.

Table 6. Approximate Concentrations of Carbon
and Oxygen in GaAs Film as Determined by
SIMS Measurements

Element	Sensitivity Factor	Background, (Atoms/cm ³)	Impurity Concentrations (Atoms/cm ³)	
			$F_{\text{AsH}_3}/F_{\text{TMGa}} = 1$	$F_{\text{AsH}_3}/F_{\text{TMGa}} = 4$
¹² C	5.5×10^{20}	2×10^{17}	1.5×10^{19}	10^{17} to 5×10^{18}
¹⁶ O	1.4×10^{20}	1×10^{17}	5×10^{17} to 4×10^{18}	10^{17} to 10^{18}
²⁸ Si (²⁸ N ₂)	4.6×10^{21}	5×10^{15}	—	—
³² S (³² O ₂)	1.3×10^{20}	2×10^{15}	—	—
⁸⁰ Se	7.8×10^{20}	$\approx 10^{14}$	—	—
¹³⁰ Te	1.5×10^{21}	$\approx 10^{14}$	—	—
⁷⁴ Ge	—	—	—	—
¹ H	—	—	—	—
⁶³ Cu	—	—	—	—

there is about $3 \times 10^{18} \text{ cm}^{-3}$ oxygen at the surface. The oxygen content decreases to near background at the interface. The ^{32}S profiles are similar to the ^{16}O profiles, and most likely are ^{32}O . There are differences in the ^{16}O profiles between the two positions in the same sample. This is surprising, considering that the separation between these two positions is only a few mm apart, and that the carbon distribution is uniform. SIMS data correspond to about 10^{16} cm^{-3} Si. This signal is most likely caused by N_2 . Concentrations of other impurities significantly above background were not apparent. Figures 30 and 31 correspond to data taken at a $F_{\text{AsH}_3}/F_{\text{TMGa}}$ of four. In this case, the peak in the carbon distribution is real and represents a high concentration of carbon at the interface. SIMS and Hall data were taken on the same samples to make the correlation between electrical properties and impurity content more valid.

B. DISCUSSION

High concentrations of carbon and oxygen are present in our films and are common in unintentionally doped GaAs films prepared by MOCVD. Figure 32 shows a plot of the carbon and oxygen content of films prepared by MOCVD techniques^{27,32,33} versus $N_A + N_D$. The high purity VPE work of Wolfe et al.³⁷ is included for comparison. Where $N_A + N_D$ was not available it was estimated from mobility data.³⁸ The type of the material, either n or p, is indicated above the set of each data. It is common for a large fraction of these impurities to be electrically neutral. If all the impurities were active, then the data would lie close to the solid line which represents a one to one correspondence between electrical activity and impurity content. A smooth dashed line is drawn through the carbon data points. The carbon content increases with $N_A + N_D$, and appears to saturate at about 10^{19} cm^{-3} , the assumed solubility limit.

Because the carbon concentration is generally higher than the oxygen concentration, it should be the component which dominates the defect chemistry. In the higher purity GaAs the carbon content is significantly

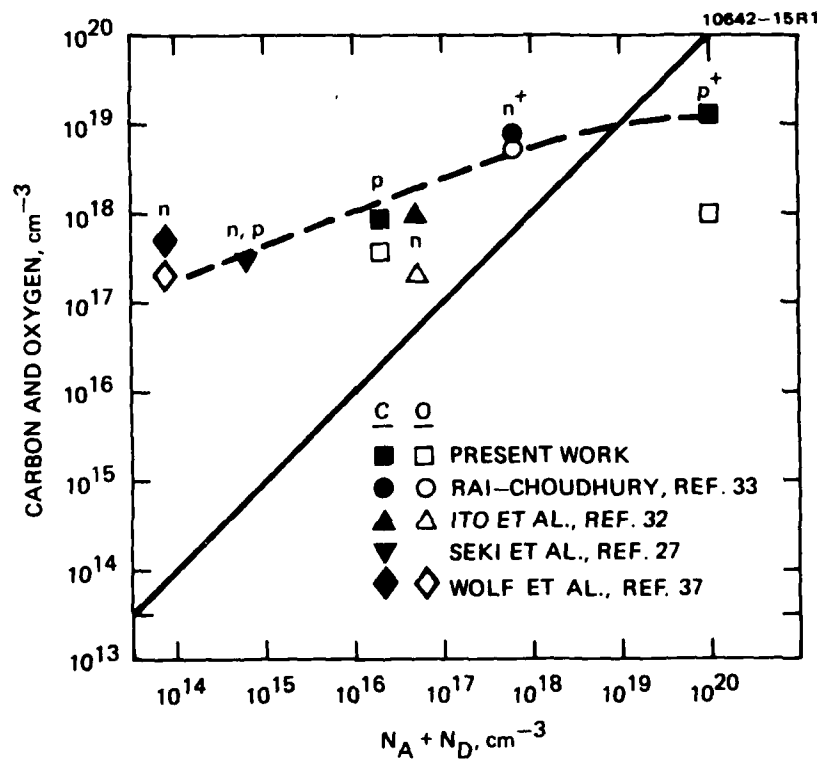


Figure 32. Carbon and oxygen content versus $N_A + N_D$ for GaAs thin films prepared by MOCVD techniques and for a high "purity" film prepared by VPE (Ref. 37).

higher than $N_A + N_D$. This is due in part to the uniqueness of the GaAs lattice. GaAs is highly covalent, and the tetrahedral covalent radii³⁴ of Ga and As are identical. Because the sublattices are nearly equivalent carbon has little preference for substituting on either Ga sites (C_{Ga}) or As sites (C_{As}). When one of the carbon atoms is incorporated on one of the sublattices as a charged defect, for example C_{Ga}^+ as a donor on the Ga sublattice, an additional carbon atom is attracted to the As sublattice as an oppositely charged acceptor C_{As}^- to form the neutral center (C_{Ga}, C_{As}). (C_{Ga}, C_{As}) should be present in high concentrations because C_{Ga} and C_{As} are oppositely charged, their sites are nearly equivalent, and they are nearest neighbors.

The carbon concentration is generally up to a factor of ten larger than the oxygen concentration.^{27,32,33,37} Near the stoichiometric composition in our material, it is about a factor of three larger. A fraction of the carbon on As sites compensates oxygen, which is presumed to also occupy As sites as donors and form neutral complexes. An even smaller fraction of carbon and oxygen atoms will form isolated electrically active defects. The concentrations of various native defects make small adjustments to further reduce the concentration of isolated electrically active impurities. The predominant native defects assumed here are the isolated defects, Ga on an As site (Ga_{As}) and As on Ga site (As_{Ga}), and the antistructure complex (Ga_{As}, As_{Ga}). Up to $5 \times 10^{19} \text{ cm}^{-3}$ antistructure defects^{34,35,36} have been tentatively identified in GaAs.

As a result of these interactions $N_A + N_D$ will be less than the total carbon and oxygen concentrations. Also small decreases in the impurity content result in large decreases in $N_A + N_D$. As the impurity concentration decreases the concentrations of neutral complexes and isolated carbon and oxygen atoms also decrease. As the concentrations of isolated carbon and oxygen atoms approach the equilibrium concentration of native defects, the native defects are more readily able to precisely compensate a greater fraction of the isolated impurity atoms. Because of the formation of neutral complexes, it is not clear as to the nature of the dominant residual acceptor or donor in GaAs. From Hall measurements on our p-type material prepared at a F_{AsH_3}/F_{TMGa} of four (Figure 24) we measured

an activation energy of 0.021 eV. This value is similar to that found in unintentionally doped p-type material and has been associated with carbon.

At large deviations from stoichiometry $N_A + N_D$ is much larger than the impurity concentration. Under these conditions most of our carbon is probably electrically active and is located on As sites. The isolated antisite defect is the majority native defect and dominates the electrical properties. Our concentration of antisite defects and holes are about 10^{20} cm^{-3} and much larger than normally considered. Higher concentration of native defects are more likely than usual if (1) we consider the antisite defect with its lower energy of formation rather than the vacancy as the majority native defect, and (2) our growth process is kinetically limited resulting in a concentration of native defects which is significantly higher than expected at thermodynamic equilibrium. In support of our high hole concentrations, Metze et al.²⁹ reported hole concentrations of $3 \times 10^{19} \text{ cm}^{-3}$ with corresponding mobilities of $10 \text{ cm}^2/\text{Vsec}$ (Figure 23). They also reported hole concentrations of up to $3 \times 10^{20} \text{ cm}^{-3}$. However, mobilities were not reported for the higher hole concentration and are presumed not to be higher than $10 \text{ cm}^2/\text{Vsec}$. Subsequent to the completion of our experimental work, Ploog et al.³¹ reported mobilities of about $50 \text{ cm}^2/\text{Vsec}$ for Be-doped material having a hole concentration of $5 \times 10^{19} \text{ cm}^{-3}$. The data of Ploog et al. fall near the envelope of high mobility material and lend support to our data. Our crystal perfection is remarkable for such high hole concentrations. Both our films and the films prepared by Metze et al. showed single-crystal channeling patterns when examined by SAD. X-ray Read pictures of our layers generally were composed of rings (polycrystalline material) and spots (single-crystal material). The latter feature may be primarily from the substrate. However, selected regions of our highly degenerate material showed only spots.

In Figure 32 $N_A + N_D$ increases with the availability of carbon. This behavior is consistent with the amphoteric impurity share model²⁷ in which the amphoteric impurities are shared between Ga and As sites, and their concentration is proportional to the concentration of

available vacancies. In our electrical data and the one atmosphere MOCVD work of Seki et al.²⁷ (Figure 22) the carrier concentration $|N_A - N_D|$ increases with deviation from the stoichiometric composition. However, there is not a one to one correspondence between the impurity content and either $|N_A - N_D|$ or $N_A + N_D$ because near the stoichiometric composition a large fraction of the carbon is electrically inactive, and at extreme deviations from stoichiometry native defects dominate the electrical activity. To decrease $N_A + N_D$ and improve the "purity" it is important to reduce the impurity content. However, the final $N_A + N_D$ and "purity" is more dependent on how impurities are incorporated and their relative concentrations.

SECTION 5

SUMMARY AND FUTURE WORK

In this program we initiated novel vacuum growth techniques which we hope will lead to the preparation of thin films of InP for higher performance microwave and millimeter-wave devices. We developed the PRD process and with it prepared films with room temperature electron mobilities (Table 7) higher than reported by all MBE groups. We believe the superior transport properties of our films were a result of growth in a reactive atmosphere. This concept was recently reinforced in the preparation of GaAs by Calawa¹⁴. Using AsH₃ as the source of As, GaAs was prepared with mobilities higher than other MBE groups. We also constructed a LPMOCVD system with the intent of preparing InP. Although we did not prepare InP, we did prepare GaAs.

The "purity" (i.e., $N_A + N_D$) of our films prepared by PRD must be improved by about a factor of ten before material is suitable for high speed devices. The transport properties of our InP films are probably limited by the presence of C and O. Mass spectrographic analyses of our films for C and O showed a concentration of less than 10^{17} cm^{-3} . The residual gas analyzer indicated our graphite crucible to be the source of CO. To improve the purity of InP films prepared by PRD it is important to modify our source and introduce a getter for C and O.

The vapor phase epitaxial (VPE) halide process operating at one atmosphere is the established and leading method of preparing high-purity InP thin films for microwave and millimeter-wave devices. The superior films prepared by the VPE halide process (see Table 7) is probably due to the ability of the halides to suppress C and O incorporation and purify In via halide transport. To achieve higher purity by vacuum processing it is necessary to incorporate halide chemistry.

Table 7. Highest Electron Room Temperature Mobility of InP Epitaxial Layers Prepared by Various Techniques

Method	Mobility, cm^2/Vsec
In/ PCl_3H_2 CVD	6,060 ^a
LPE	4,880 ^b
Metal-organic CVD	
Low Pressure	4,300 ^c
One Atmosphere	3,540 ^d
PRD	4,062 ^e
MBE	3,500 ^f
^a R.D., Fairman, M. Omori, and F.B. Frank, 1977 "Gallium Arsenide and Related Compounds," <u>Inst. Phys. Conf. Ser.</u> 33b, p. 45 ^b C.E.C. Wood, R.J. Tree, and D.H. Paxman, <u>Electron. Lett.</u> 8, 171 (1972). ^c J.P. Duchemin, M. Bonnet, G. Beuchet, and F. Koelsch, "GaAs and Related Compounds," 1978 <u>Inst. Phys. Conf. Ser.</u> 45, p. 10. ^d M. Tsai and R. Bube, <u>J. Appl. Phys.</u> 49, 3397 (1978) ^e K. Zanio, L. Fraas, F. Krajenbrink, and L. Hershenson, 21 st Electronic Materials Conference, Boulder, Colorado, June 27-29, p. 16 of Abstracts.	

The PRD and hybrid MBE processes are more promising approaches than LPMOCVD to prepare high purity InP films. There are several disadvantages of growing InP films by LPMOCVD. First the metal organic is a source of carbon. There is also a tendency for unwanted intermediate reactions to act as additional potential sources of carbon. Secondly, sources of high purity metal organic indium are not routinely available. Purity is more important in the preparation of InP than in the preparation of GaAs because the impurities tend to remain isolated and electrically active rather than form neutral complexes. Because of significant differences between the tetrahedral covalent radii of In and P, and because InP is more ionic than GaAs, the majority native defect is the phosphorous vacancy, a donor. Amphoteric impurities will not readily form neutral complexes. Instead, the Group IV atoms become incorporated on the In sublattice also as donors. This has the advantage that the solubility of Group IV atoms is not enhanced through neutral complex formation. Hence, we found C and O in concentrations of the order of 10^{17} cm^{-3} in our InP as compared to 10^{18} cm^{-3} for GaAs. However, there is a disadvantage when the neutral complex is not formed. The disadvantage is that most of the impurity atoms including C and Si are isolated and electrically active resulting in a high $N_A + N_D$ and $N_D - N_A$. The disadvantage outweighs the advantage. Therefore, in the preparation of InP as compared to GaAs, it is more important to avoid the presence of carbon. Therefore it is more promising to incorporate halide chemistry rather than metal organic chemistry in the growth of thin films of InP by vacuum technologies.

REFERENCES

1. J.D. Crowley, J.J. Sowers, B.A. Janis, and F.B. Frank, Electron. Lett. 16, 705(1980).
2. M. Armand, J. Chevrier, and Nuyen T. Linh, Electron. Lett. 16, 906(1980).
3. P. Moutou, J. Chevrier, A. Huber, and J. Montel, Proc. Inter. Sym. on GaAs and Related Comp., 1978 Inst. Phys. Conf., Ser. 45.
4. J.H. McFee, B.I. Miller, and K.J. Bachmann, J. Electrochem. Soc. 124, 259(1977).
5. R.D. Fairman, M. Omori, and F.B. Frank, "Gallium Arsenide and Related Compounds," Inst. Phys. Conf. Ser. 33b(1977) p.45.
6. J.P. Duchemin, M. Bonnet, G. Beuchet, and F. Koelsch, "Gallium Arsenide and Related Compounds." St. Louis, Mo., 1978. (Inst. Phys. Conf. Ser. 45, p. 10)
7. L. Fraas, and K. Zanio, J. of Electronic Materials 7, 211(1978).
8. L. Fraas, U.S. Patent No. 4,063,974.
9. K. Zanio, L. Fraas, F. Krajenbrink, and L. Hershenson, 21st Electronic Materials Conference, Boulder, Colorado, June 27-29, 1979. p. 16 of Abstract.
10. M.T. Norris, Appl. Phys. Lett. 36, 282(1980).
11. Y. Kawaniura, M. Ikeda, H. Asaki, and H. Okaruoto, Appl. Phys. Lett. 35, 481(1979).
12. R.F.C. Farrow, J. Phys. D8, 187(1975).
13. A.R. Calawa, Appl. Phys. Lett. 33, 1020(1978).
14. A.R. Calawa, 1980 Molecular Beam Epitaxy Workshop, Cornell U., Ithaca, N.Y., Oct. 21-22, 1980. To be published in Appl. Phys. Lett.
15. H.M. Manasevit, K.L. Hell, P.D. Dapkus, R.P. Ruth, J.J. Yang, A.G. Campbell, R.E. Johnson, L.A. Moudy, R.H. Bube, L.B. Fabick, A.L. Fahrenbruch, and M-J. Tsai, Proc. 13th IEEE Photovoltaic Specialists Conf. 164 (1978)

16. H. Renz, J. Weidlein, K.W. Benz, and M.H. Pilkuhn, *Electron. Lett.* 16, 228(1980).
17. R. Didchenko, J.E. Alix, and R.H. Toeniskoetter, *J. Inorg. Nucl. Chem.* 14, 35(1960).
18. K. Zanio, "Analysis of P-type GaAs Prepared by Low Pressure Metal Organic Chemical Vapor Deposition," Abstract of the Fifth International Conference on Vapor Growth and Epitaxy, July 19-24, 1981, Coronado, California.
19. F. Krajenbrink and K. Zanio, "Epitaxial Growth of InP, GaP, and InGaP by Planar Reactive Deposition," presented at Fourth Conference on Crystal Growth, Fallen Leaf Lake, California, May 1979.
20. K. Zanio, L. Fraas, and F. Krajenbrink, *J. Vac. Sci. Technol.* 15, 119(1978).
21. L. Fraas, K. Zanio and R. Knetchli, U.S. Patent No. 4,171,235.
22. M. Davis and R.F. Lever, *J. Appl. Phys.* 27, 835(1956).
23. B.A. Joyce and R.R. Bradley, *Phil. Mag.* 14, 289 (1966).
24. D.J. Schlyer and M.A. Ring, *J. Electrochem. Soc.* 124, 569(1977).
25. R.S. Rosler, *Solid State Technol.* 20, 63(1977).
26. J.P. Duchemin, M. Bonnet, F. Koelsch, and D. Huyghe, *J. Electrochem. Soc.* 126, 1134(1979).
27. Y. Seki, K. Tanno, K. Iida and E. Ichiki, *J. Electrochem. Soc.* 122, 1108 (1975).
28. M. Hegems and R. Dingle, *Inst. Phys. Conf. Ser. No. 24*(1975) p. 1.
29. G. Metze, R. Stall, C. Wood and L. Eastman, *Appl. Phys. Lett.* 37, 165(1980).
30. A.Y. Cho and J.R. Arthur, *Progress in Solid State Chemistry*, Vol. 10, pt. 3 (Pergamon Press, 1975, p. 157-191).
31. K. Ploog, A. Fischer and H. Künzel, *J. Electrochem. Soc.* 128, 400(1981).
32. S. Ito, T. Shinohara, and Y. Seki, *J. Electrochem. Soc.* 120, 1423(1973).

33. P. Rai-Choudhury, J. Electrochem. Soc. 116, 1745 (1969).
34. J.A. Van Vechten, J. Electrochem. Soc. 122, 423(1975)
35. B. Goldstein and N. Almeleh, Appl. Phys. Lett. 2, 130(1963)
36. J. Blanc, R.H. Bube and L.R. Weisberg, J. Phys. Chem. Solids 25, 225(1964)
37. C.M. Wolfe, G.E. Stillman and E.B. Owens, J. Electrochem. Soc. 117, 129(1970)
38. G. Stillman and C. Wolfe, Thin Solid Films, 31, 69(1976)

PUBLICATIONS, PATENTS, AND PRESENTATIONS

The following publications, patents, and presentations either resulted from this contract or were related to this contract during its period of performance.

Publications

L. Fraas and K. Zanio, "InP-on-CdS Heterostructures," J. Electronic Materials 7, 211 (1978). (Appendix A).

K. Zanio, L. Fraas, and F. Krajenbrink, "Deposition of Ge Epitaxial Layers on Ge and GaAs Substrates," J. Vac. Sci. Technol. 15, 119 (1978). (Appendix B).

L.M. Fraas and R.C. Knechtli, "Design of High Efficiency Monolithic Stacked Multijunction Solar Cells," 13th IEEE Photovoltaic Specialists Conference 886 (1978). (Appendix C).

L. Fraas and K. Zanio, "Electronic Structure of Grain Boundaries in Polycrystalline Semiconductor Thin Films," book chapter in Properties of Polycrystalline and Amorphous Thin Films and Devices edited by L. Kazmerski, Academic Press, p. 153 1979 (Appendix D).

K. Zanio, "Analysis of p-type GaAs Prepared by Low Pressure Metal Organic Chemical Vapor Deposition," to be published in Journal of Crystal Growth (Appendix E).

Patents

Kenneth Zanio and Lewis Fraas, U.S. Patent No. 4,108,684 "Large Grain Thin Film Polycrystalline p-InP/n-CdS Solar Cells."

Lewis Fraas, Kenneth Zanio, and Ronald Knechtli, U.S. Patent No. 4,17,235 "Process for Fabricating Heterojunction Structure Using a Double Chamber Vacuum Deposition System."

Presentations

L. Fraas and K. Zanio, "InP on CdS Thin Film Solar Cells," presented at 19th Electronic Materials Conference, Ithaca, NY, Cornell University, June 29 - July 1, 1977.

L.M. Fraas and K. Zanio, Invited Paper "Semiconductor Thin Films Prepared by Low Pressure Reactive Deposition Process," presented at American Vacuum Society, 11th Annual Symposium of the Southern California Chapter, April 18, 1978, Cockatoo Inn, Hawthorne, CA.

L.M. Fraas and K. Zanio, Invited Paper, "Semiconductor Thin Films Prepared by Low Pressure Reactive Deposition Process," presented at the International Conference on Metallurgical Coatings, 5-7 April 1978, San Francisco, CA.

F. Krajenbrink and Z. Zanio, "Epitaxial Growth of InP, InGaP, and InGaAsP by Planar Reactive Deposition," presented at Fourth Conference on Crystal Growth, Fallen Leaf Lake, CA, May 1979.

K. Zanio, L.M. Fraas, and F. Krajenbrink, "An Evaluation of InP Thin Films Prepared by Planar Reactive Deposition," presented at the Third Conference on Crystal Growth, 12-13 January 1978, U.S. Naval Postgraduate School, Monterey, CA.

K. Zanio, L. Fraas, F. Krajenbrink, and L. Hershenson, "Preparation of InP by Planar Reactive Deposition," presented at the 21st Electric Materials Conference, Boulder, CO, June 27 - 29 1979 (Appendix F).

K. Zanio, "An Analysis of p-type GaAs Prepared by Low Pressure Metal Organic Chemical Vapor Deposition," to be presented at the Fifth International Conference on Vapor Growth and Epitaxy, July 19 - 24, 1981, Coronado, CA.

APPENDIX A

INP-ON-CdS THIN FILM HETEROSTRUCTURES

InP-on-CdS Thin Film Heterostructures^{*}

L. Fraas and K. Zanio

Hughes Research Laboratories

3011 Malibu Canyon Road

Malibu, CA 90265

(Received August 10, 1977)

Thin films of InP were deposited on single crystals and thin films of CdS by the planar reactive deposition technique. Good local epitaxy was observed on single crystals of CdS as well as InP and GaAs. The electrical evaluation of unintentionally doped films on semi-insulating InP substrates show them to be n-type with room temperature electron concentrations ranging from $5 \times 10^{16} \text{ cm}^{-3}$ to $5 \times 10^{17} \text{ cm}^{-3}$ and mobilities up to $1350 \text{ cm}^2/\text{Vsec}$. For films intentionally doped with Mn and Be, p-type films were obtained. For Mn doping (deep acceptor level), room temperature mobilities as high as $140 \text{ cm}^2/\text{Vsec}$ and free carrier concentrations as low as $5 \times 10^{16} \text{ cm}^{-3}$ (with dopant level of $3 \times 10^{18} \text{ cm}^{-3}$) were obtained. For Be-doped films, free carrier concentrations of about $5 \times 10^{18} \text{ cm}^{-3}$ and mobilities of $20 \text{ cm}^2/\text{Vsec}$ were found. Scanning electron microscope and microprobe pictures show appreciable interdiffusion between the InP/CdS thin-film pair for InP deposited at 450°C . The loss of Cd from the CdS and the presence of an indium-cadmium-sulfur phase at the InP/CdS interface were observed. Interdiffusion is alleviated for InP deposition at lower temperatures.

^{*}Supported in part by ERDA and AFOSR.

Key Words: Heterostructures, planar reactive deposition, indium phosphide, cadmium sulfide.

Introduction

The InP/CdS heterojunction solar cell has been investigated by several workers. (1-6) Cells fabricated by depositing CdS thin films on InP single-crystal substrates have shown efficiencies as high as 15% at Air Mass 2. (1-3) However, the commercial viability of this cell for terrestrial applications hinges on the fabrication of an all-thin-film cell. This follows not only because of the high cost of growing single crystals, but also because indium is a relatively rare element. In fact, Hovel⁽⁷⁾ indicates that indium is so rare that an InP film thickness of only 2 μm is allowable if the InP/CdS cell without concentration were to be relied upon to supply 3% of the present US electrical energy need. Since large InP crystallites are desirable for high-efficiency cells and since, in general, the crystal grain size in a film on an amorphous substrate is no larger than the film thickness, the thin-film InP/CdS solar cell structure of Figure 1 appears desirable. Basically, the idea is to deposit the InP film on a CdS film; this CdS film will be relatively thick and have grains with dimensions of about 10 μm . If the InP grain structure can be made to replicate that of the CdS film and the InP film is about 1 μm thick, the lateral dimensions can be large compared to the InP film thickness. Since a method for producing large grain size CdS films by recrystallization has been described in the literature, (8) the successful fabrication of a high-efficiency all-thin-film InP/CdS cell of the type in Figure 1 will hinge on the answers to four basic questions: (1) Can a p-type InP film be deposited at temperatures high enough so that local epitaxy will occur but yet low enough so that the CdS film does not decompose? Would the electrical properties in the grains then be adequate for good cell performance? (2) Since the thin-film structure contains grain boundaries in the InP layer, what are the effects of these grain boundaries and how can they be controlled? (3) Since the recrystallized CdS film will have wurtzite-type crystals of varying orientations, (9) how will the heterojunction properties vary with crystal orientation? (4) Can the InP film be contacted with an ohmic contact without shorting to the CdS film?

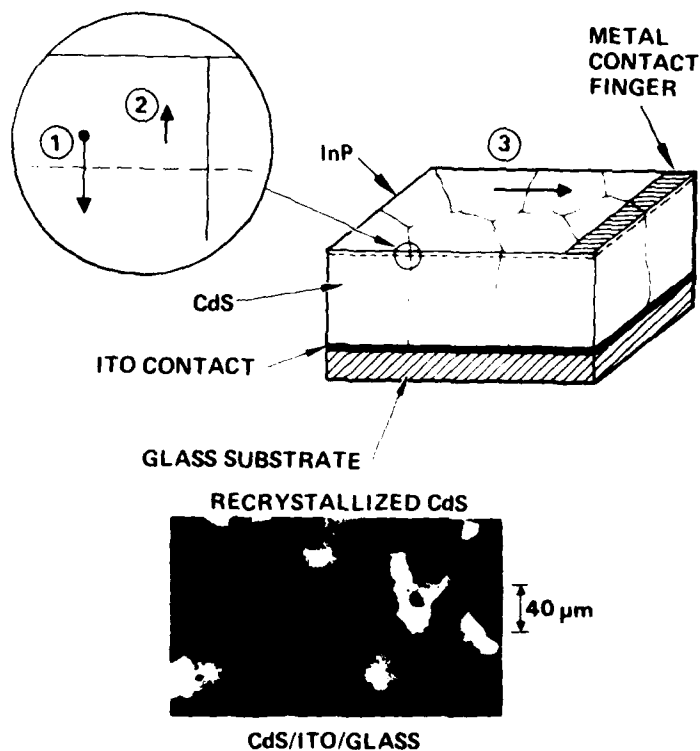


Figure 1. Schematic of a quasi-single-crystal InP/CdS all-thin-film solar cell. The insert at the lower left is a crossed polarizer photograph of recrystallized CdS on glass. In order to fabricate a good solar cell, one must (1) maximize the light generated current, (2) minimize diode leakage current, and (3) minimize thin film sheet resistance.

In this paper we present data relevant to problem areas 1 and 2. With regard to problem area 3, we simply note that Yoshikawa and Sakai⁽²⁾ and Shay et al.^(1,3) report high-efficiency cells prepared by the epitaxial deposition of CdS on (100) and (110) as well as (111) oriented substrates. With regard to problem area 4, we note that although the contact to InP is a problem for fabricating a CdS-on-InP thin-film cell,^(4,5,6) the problem is reduced for the cell in Figure 1 because a larger number of contacting options are available at the last processing step. In the next section, we consider low-temperature growth of semiconductor-quality InP thin films (problem No. 1).

The Structure and Electrical Properties of InP Thin Films Deposited by Planar Reactive Deposition

The deposition of InP films on CdS requires a low temperature process ($<400^{\circ}\text{C}$) to prevent decomposing the CdS. Molecular beam epitaxy (MBE) is such a process. Unfortunately, the MBE process is not scalable to the volumes required for commercial solar-cell applications. Chemical vapor deposition (CVD) processes are commercially viable. In an earlier publication,⁽¹¹⁾ we described a planar reactive deposition (PRD) process which potentially allows both low-temperature processing and scalability for film depositions over large substrate areas. The PRD process is a hybrid between MBE and CVD. Figure 2 shows a top view of the basic vacuum chamber used for the PRD technique. A substrate plate rides on the three bearings (not shown). Below the plate are two PRD deposition units which permit the deposition of films of different composition. A cross section through one of the two PRD positions is shown in Figure 3. The substrates, mounted above the source cavity, and the source cavity itself are enclosed by a liquid-nitrogen-cooled shroud. This effectively forms an inner CVD-type growth chamber. InP films are deposited by evaporating indium metal from an indium source cavity into which a $\text{PH}_3\text{-H}_2$ gas mixture is introduced. The PH_3 gas decomposes in the indium source cavity, and indium vapor, P_2 vapor, and H_2 gas are emitted, providing molecular beams incident on the substrates. The vapor pressure of the indium controls the film growth rate and is determined by the source temperature. Residual gases are exhausted at the pump port by a turbomolecular pump. Stoichiometric films

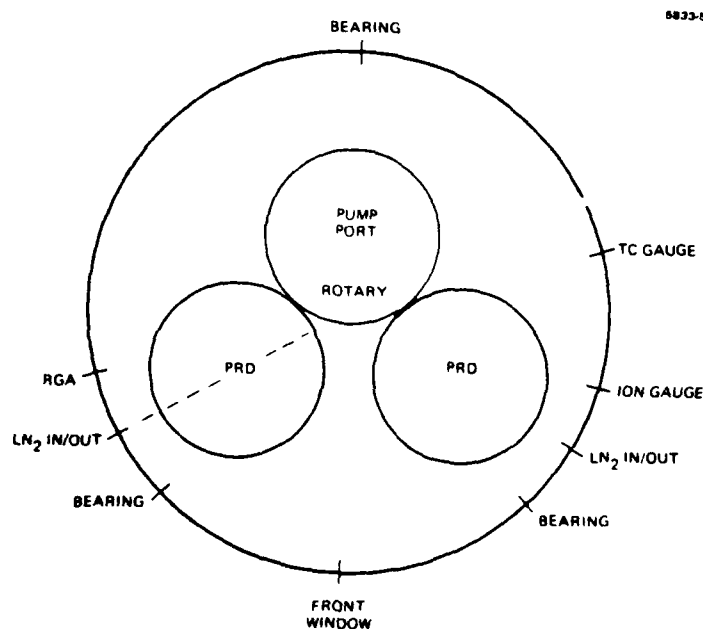


Figure 2. Schematic top view of the vacuum chamber in the PRD system.

are produced by adjusting the $\text{PH}_3\text{-H}_2$ gas inlet needle valve to allow an excess of P_2 vapor in the inner growth chamber. The heat shield in the chamber serves the additional function of confining the phosphorous vapor within the growth chamber. This reduces phosphorous film buildup in the vacuum chamber to well below that found in the MBE process. The phosphorous vapor which does escape is collected by the LN_2 shroud.

We have applied the PRD process to the growth of epitaxial InP films on InP, CdS, and GaAs single-crystal substrates. Figure 4 shows SEM photographs of InP epitaxial films on (100)-oriented InP and GaAs single-crystal substrates. These films were grown at 425°C . Figure 5 shows SEM photographs of an InP epitaxial film grown at 350°C on the Cd face of an (0001)-oriented CdS single-crystal

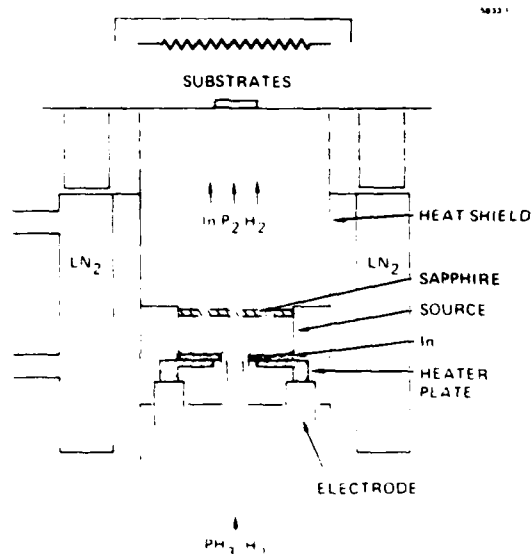


Figure 3. Sideview of a PRD deposition unit.

substrate. Growth procedures and substrate preparation are described briefly below.

All single-crystal samples were mounted on molybdenum blocks with indium solder, then polished and processed completely on these blocks. The InP and GaAs samples were polished and etched in Et methanol as described by McFee et al.⁽¹⁰⁾ The CdS samples were handled substantially as we described in an earlier publication.⁽¹¹⁾ However, they were heavily etched in a hot (85°C) 1:5 HCl:H₂O solution for 7 min just prior to loading. This procedure eliminated the mechanical polishing damage encountered in our earlier work. It produced samples with locally flat facets ($\approx 100 \mu\text{m}$) but with an orange-peel appearance. The deposition procedure was substantially the same for the InP and the CdS samples, differing only in the substrate temperature and thermal cleaning procedure. We will describe the process used for the InP substrates because most of the electrical data relates to these substrates. After loading the samples onto the rotary substrate plate,

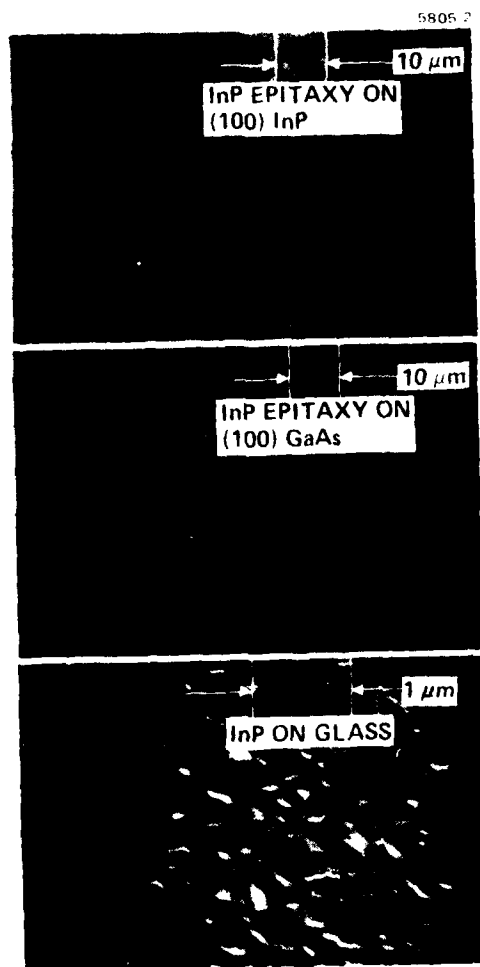


Figure 4.
Scanning electron microscope pictures
of InP epitaxially deposited onto
(100) InP and GaAs.

AD-A099 993

HUGHES RESEARCH LABS MALIBU CA

F/G 20/12

INP BY PLANAR REACTIVE DEPOSITION AND GAAS BY LOW PRESSURE META--ETC(U)

FEB 81 K ZANIO

F44620-76-C-0133

NL

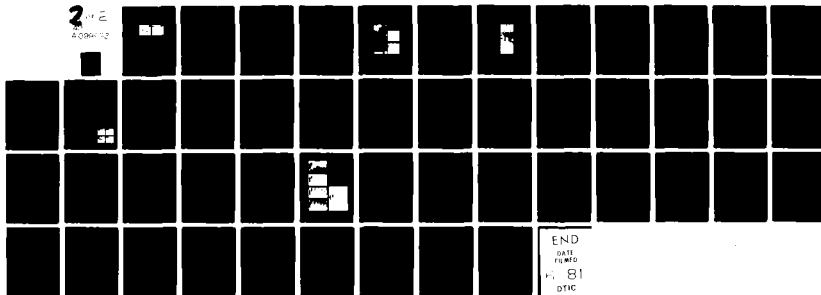
UNCLASSIFIED

AFOSR-TR-81-0474

2

20/12

20/12



END

DATE

FORMED

81

DTIC

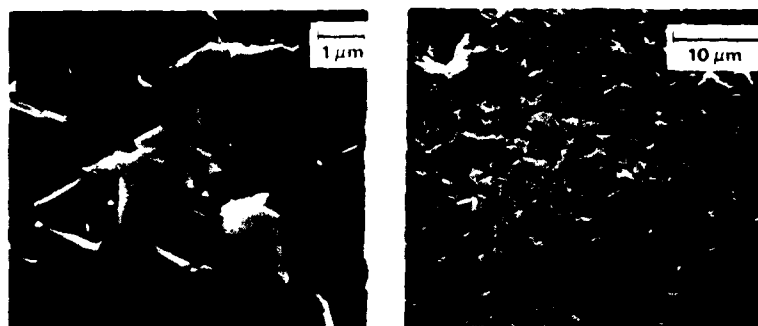


Figure 5. Scanning electron microscope pictures of InP epitaxy on the Cd face of (0001) CdS.

the vacuum chamber is pumped down to the 10^{-8} Torr scale. Then LN₂ is added to the shroud. The source is turned up to 800°C for outgassing while the substrates are being preheated to 350°C in an adjacent position not over the source. Then phosphine gas is introduced and the source turned up to 850°C for final getter cleaning. After getter cleaning for 60 min, the source is turned down to 700°C and the substrates are rotated into position above the source. The InP substrates are then heated to 425°C for thermal cleaning in the presence of phosphorus vapor. The phosphorus vapor stabilizes the InP surface against indium droplet formation⁽¹²⁾ and allows reproducible thermal cleaning. Finally, the source temperature is tuned up to 850°C for film deposition. After deposition, the source is turned down to 700°C and the substrates are allowed to cool to 350°C before rotating to the next deposition or turning off the phosphorus vapor flux.

The electrical properties of InP films prepared by PRD on Fe-doped semi-insulating InP single-crystal substrates are summarized in Table I. Unintentionally doped films are n-type with carrier concentrations in the 10^{17} cm⁻³ range

Table I. Electrical Properties and Growth Temperature of InP Films with PRD and Reference Solar Cell Materials

Material	Dopant	Type	Carrier Concentration, cm^{-3}	Mobility, $\text{cm}^2/\text{V-sec}$	Growth Temperature $^{\circ}\text{C}$
InP	Unintentional	n	5×10^{17}	1350	450
InP	Mn	p	5×10^{16}	140	450
InP	Be	p	5×10^{18}	20	450
Si^{c}	B	p	1×10^{16}	600	1450 ^a
Si^{c}	P	n	2×10^{17}	1300	1450 ^a
$\text{Cu}_2\text{S}^{\text{b}}$		p	1×10^{20}	10	100

^aSingle crystal growth
^bP.F. Lindquist and R.H. Bube, J. Electrochem. Soc. 119, 93b (1972).
^cRef. 7

and with mobilities as high as $1350 \text{ cm}^2/\text{Vsec}$. Mass spectrographic analysis of the impurities in a thick film of InP on a silicon substrate shows the predominant impurity to be sulfur at 6 ppm. Low-temperature Hall measurements show no carrier freeze-out down to 15 K, which is consistent with the possibility of sulfur as an impurity. Sulfur is not unexpected since CdS substrate experiments are undertaken in the same deposition chamber. Notably, no molybdenum was detected in the films. This indicates that the possible phosphorus transport reaction with the molybdenum heat shields is not of concern.

We have prepared p-type films by doping both with Mn⁽¹³⁾ and Be.⁽¹⁴⁾ Manganese doping is particularly convenient because manganese and indium have very similar vapor pressures. Adding $3 \times 10^{18} \text{ cm}^{-3}$ Mn to the indium melt produces a similar impurity content in the growing InP film. Since Mn is a deep acceptor (0.25 eV),⁽¹²⁾ only $5 \times 10^{16} \text{ cm}^{-3}$ holes are found at room temperature. The mobility (μ) of the manganese-doped film is about $140 \text{ cm}^2/\text{Vsec}$ at room temperature. Beryllium doping

allows a p^+ InP layer to be prepared. Beryllium metal placed with the indium melt⁽¹⁵⁾ produces layers with $5 \times 10^{18} \text{ cm}^{-3}$ free holes. Such a layer alleviates contact problems to the InP because most metals can potentially form a high-conductivity tunnel junction with p^+ InP.

In summary, we have shown that InP films can be deposited epitaxially by PRD on CdS substrates at low temperatures (350°C) and that such InP films deposited via PRD on InP substrates can be doped with p-type dopants as in MBE.

How good do transport properties of the reproduced grain have to be? Relative to the silicon solar cell, the transport properties can actually be quite poor and still allow good carrier collection efficiencies. The reason is that the allowable recombination center density N_r is proportional to the square of the optical absorption coefficient α . The condition that the carriers must diffuse a distance (L) comparable to the reciprocal of the absorption coefficient implies:

$$1/\alpha \approx L \quad (1)$$

If the diffusion length is given by

$$L = \sqrt{D\tau} = \sqrt{\frac{D}{qv_{th}N_R}} \quad (2)$$

with D , v_{th} , and σ , respectively, the diffusivity, thermal velocity, and capture cross section, and assuming D , v_{th} , and σ are comparable in both Si and InP, then

$$\frac{N_R(\text{InP})}{N_R(\text{Si})} = \left(\frac{\alpha_{\text{InP}}}{\alpha_{\text{Si}}} \right)^2 \approx 1000 \quad (3)$$

This assumes absorption coefficients of approximately $4 \times 10^4 \text{ cm}^{-1}$ and 10^3 cm^{-1} , respectively for InP⁽¹⁾ and Si.⁽⁷⁾ Assuming $\mu = 10^3 \text{ cm}^2/\text{Vsec}$ and $\sigma = 10^{-15} \text{ cm}^2$, Ref. 16, the allowable upper limit for N_r is $4 \times 10^{18} \text{ cm}^{-3}$. In this context, the purity of the unintentionally doped

and Mn-doped InP films of Table I is possibly good enough for solar cell applications. The final answer to the question of the quality of the transport properties will have to await actual cell fabrication.

Grain Boundary Problems Inherent in Thin-Film Heterojunction Solar Cells

When an InP film is deposited on a CdS film at 425°C, appreciable interdiffusion occurs. This is illustrated in scanning electron microscope (left) and microprobe (right) pictures of a cleaved all-thin-film InP/CdS structure (Figure 6). The upper SEM picture shows a top view of the structure near the cleavage; the bottom view shows an edge view of the cleavage. The microprobe data shows the composition of the top and base of the film relative to a pure CdS film. The original CdS film underneath the InP film apparently has been converted to indium sulfide. The deposition conditions of InP were such that a 6 μm film of InP should have formed (2 hr at 3 $\mu\text{m/hr}$). Apparently, as indium arrived on the CdS surface, the indium preferentially reacted with sulfur to release cadmium, thereby forming an indium cadmium sulfide compound. This interpretation is consistent with the fact that In_2S_3 is quite stable, (17,18) whereas Cd_2P_3 is quite volatile. (19) InP did not form until the cadmium had been largely depleted. This apparently occurred near the end of the deposition.

These results are important for two reasons. First, they suggest that the properties of the possible compounds formed by In, Cd, P, and S be investigated in more detail. Second, they allow us to develop a hypothesis regarding InP grain boundary passivation.

Besides InP and CdS, the compounds Cd_2P_3 , CdIn_2S_4 (Ref. 20) and $(\text{CdS})_{3x} - (\text{In}_2\text{S}_3)_{1-x}$ (Ref. 18) can be formed. The Cd_2P_3 is quite volatile even at low temperatures (10^{-3} Torr at 250°C), it will not form during InP/CdS heterojunction formation. The indium sulfide compounds, on the other hand, are more stable than either CdS or InP and require further comment. In_2S_3 has a defect sphalerite structure, is n type, and has a band gap of 2.1 eV at room temperature. (21) CdIn_2S_4 has the spinel structure, is n type, and has a band gap of 2.3 eV. Both the In_2S_3 and CdIn_2S_4 sulfur lattices are significantly smaller than the sulfur lattice for CdS.

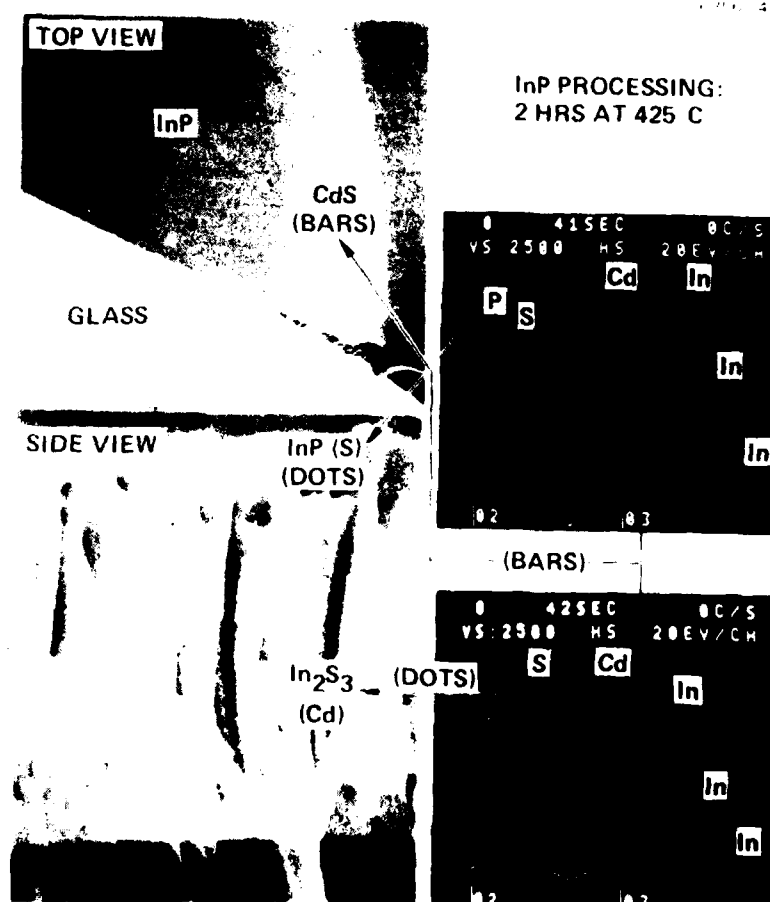


Figure 6. Scanning electron microscope (left) and microprobe (right) pictures of a cleaved all-thin-film InP/CdS structure. The upper SEM picture shows a top view of the structure near the cleavage; the bottom view shows an edge view of the cleavage. Both microprobe pictures include data taken from the top view on the CdS film (bars). The upper picture also shows edge view data where the InP has been deposited (dots). The bottom picture shows edge view data where the CdS had been deposited.

For the deposition of InP on CdS at reduced temperatures, interdiffusion is not apparent. Figure 7 shows the SEM edge view of a 2 μm InP film deposited onto a 2 μm CdS film at about 300°C. Markers at X_1 and X_3 correspond to positions where, respectively, InP and CdS had been deposited. The dots indicate data taken at these positions, and the bars reflect the CdS and InP standards. In the upper picture (X_1), the dots (as expected) overlay the InP standard and not the CdS standard. In the lower picture (X_3), the dots (as expected) overlay the CdS standard and not the InP standard. In contrast with Figure 6, Cd is present in stoichiometric proportions in region X_3 . In the region of $X_1(X_3)$ where InP(CdS) was deposited, there is some indication that CdS(InP) is present. However, it is not resolved as to whether this is due to interdiffusion or X-ray excitation outside of the region of the direct electron beam. Position X_2 corresponds to the CdS/InP interface and, as expected, all four elements are observed.

As lower deposition temperatures are employed, and when larger CdS grains are considered (recrystallized CdS), it is likely that interdiffusion will be restricted to the grain boundary region. Unquestionably, indium diffusion will occur into the CdS film, producing an n^+ grain boundary. However, the nature of the InP grain boundary is open to question.

For any elevated temperature used to form the InP/CdS thin-film structure, an indium cadmium sulfide transition region should be present. This is not necessarily an obstacle to the formation of the all-thin-film cell, since such a layer is obviously present in the high-efficiency CdS-on-InP single-crystal cell prepared at 600°C. However, it is apparent that the all-thin-film cell must be prepared at lower temperatures to minimize grain boundary interdiffusion.

Indium diffuses into CdS and replaces the Cd. Cadmium diffuses through the InP and tends to volatilize at the growing InP surface. For InP growth in the presence of excess P, we hypothesize that sulfur will determine the InP grain boundary properties. If an In_2S_3 phase actually forms (high-angle grain boundary), the grain boundary will be n type. If sulfur diffuses along the grain boundary and into the bulk of the InP lattice a short distance and occupies a phosphorus lattice site, the grain boundary will

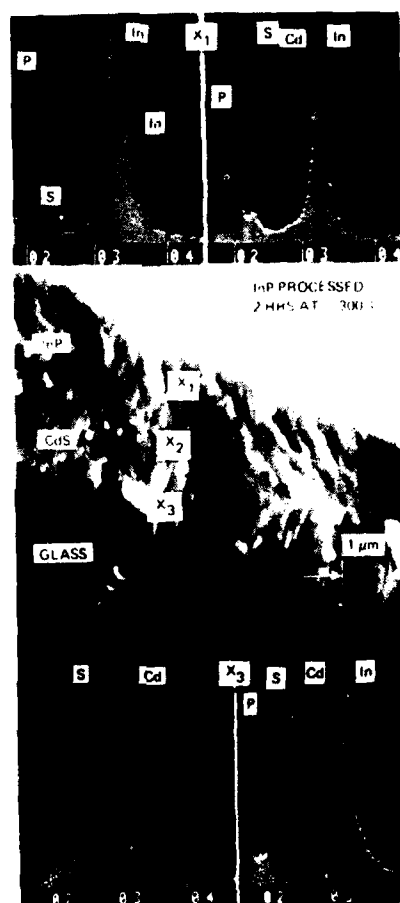


Figure 7.
Scanning electron microscope picture (middle) of a cleaved InP/CdS/Glass structure. Microprobe analysis of the CdS film (bottom) shows that Cd and S dominate. The dots refer to the actual data whereas the bars refer to stored standard of pure stoichiometric CdS and InP.

be n type. In a low-angle grain boundary consisting of equal numbers of indium and phosphorus edge dislocations, (22) we hypothesize that sulfur can diffuse into the edge dislocation with adjacent indium atoms. One sulfur per two indium atoms at the edge dislocation tends to neutralize that edge dislocation. The un-neutralized phosphorus-type dislocation then contributes electrons, and the grain boundary again will be n type.

Figure 8(a) describes, then, the predicted InP/CdS thin-film electrical structure after InP deposition and before contact formation. Unfortunately, the n-type grain boundary in the p-type InP film is a potential short. If not catastrophic, grain boundary leakage can degrade the open circuit voltage. The problem then is how to passivate the grain boundary. Basically, the answer lies in counter-diffusion from the InP contact. For example, if we assume that a second In_2S_3 phase does not form at the grain boundary, then a deep acceptor for bulk InP can compensate sulfur at the grain boundary, producing a semi-insulating grain boundary (Figure 8(b)). The final answer lies in device fabrication experiments.

Summary

Using PRD we have demonstrated the epitaxy of InP on CdS single crystals and have obtained p-type InP by intentionally doping with Mn and Be. We have evidence that an intermediate phase of indium cadmium sulfide can form between CdS and InP at higher temperatures. Finally, we have discussed the potential effects of interdiffusion at grain boundaries. An increased understanding of chemical impurity effects at grain boundaries may lead to methods of grain boundary passivation.

References

1. S. Wagner, J.L. Shay, K.J. Bachmann, E. Buehler and M. Bettini, J. Crystal Growth 39, 128 (1977).
2. Akihiko Yoshikawa and Yoshio Sakai, Solid State Electronics 20, 133 (1977).

6356-5 R1

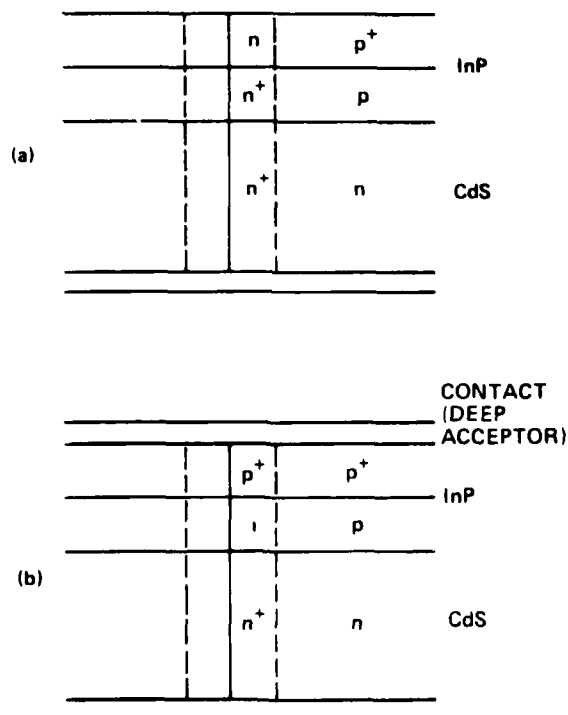


Figure 8.
Hypothetical electrical properties at the
InP/CdS thin film grain boundaries
(a) after InP deposition and (b) after InP
deposition and subsequent contact anneal
of deep acceptors.

3. J.L. Shay, M. Bettini, S. Wagner, K.J. Bachmann, and E. Buehler, 12th IEEE Photovoltaic Specialists Conference, p. 540 (1976).
4. K.J. Bachmann, E. Buehler, J.L. Shay, and S. Wagner, Appl. Phys. Lett. 29, 121 (1976).
5. Tadashi, Saitoh, Sunao Matsubara, and Shigekazu Minagawa, Jap. J. Appl. Phys. 16, 807 (1977).
6. L.L. Kazmerski, F.R. White, W.S. Ayyagari, Y.J. Juang, and R.P. Patterson, J. Vac. Sci. Technol. 14, 65 (1977).
7. Harold J. Hovel, Semiconductors and Semimetals, Vol. 11 - Solar Cells, Academic Press, N.Y. (1975).
8. L.M. Fraas, W.P. Bleha, and P. Braatz, J. Appl. Phys. 46, 491 (1975).
9. Evaporated CdS films usually have a (0001) texture whereas recrystallize films do not.
10. J.H. McFee, B.I. Miller, and K.J. Bachmann, J. Electrochem. Soc. 124, 259 (1977).
11. L.M. Fraas, K. Zanio, and M. Shibata, Appl. Phys. Lett 28, 415 (1976).
12. R.F.C. Farrow, J. Phys. D8, 187 (1975).
13. K.J. Bachmann, E. Buehler, B.I. Miller, J.H. McFee and F.A. Thiel, J. Crystal Growth 39, 137 (1977).
14. S.P. Starosel'tseva, V.S. Kulov, and S.G. Metreveli, Sov. Phys. -Semiconductors 5, 1603 (1972).
15. Beryllium foil placed with the indium melt turns to powder after several runs. Since beryllium powder is a health hazard, we are investigating placing an Al:Be alloy in a recess in the perforated top plate. Alternatively, zinc doping could be potentially accomplished by introducing diethylzinc in the gas stream.

16. The median value of 10^{-15} cm^2 is assumed for Si. This value is consistent with data presented by J.R. Davis, P. Rai-Choudhury, P.D. Blais, R.H. Hopkins and J.R. McCormick. Proceedings of "Twelfth IEEE Photovoltaic Specialists Conference" 1976, Baton Rouge.
17. R. Colin and J. Drawart, Trans. Faraday Soc. 64, 2611 (1968).
18. V.B. Ufimtzen and F.A. Gimelfarb Neorg. Mater. 9, 2073 (1973).
19. R. Schoonmaker and K. Robinson, J. Phys. Chem. 71, 3354 (1967).
20. W. Rehwald and G. Harbeke, J. Phys. Chem. Solids 26, 1309 (1965).
21. W. Czaja and L. Krausbauer, Phys. Stat. Sol. 33, 191 (1969).
22. H.F. Matere, Defect Electronics in Semiconductors, Wiley Interscience, N.Y. (1971).

APPENDIX B

DEPOSITION OF Ge EPITAXIAL LAYERS ON Ge AND GaAs
SUBSTRATES BY VACUUM PYROLYSIS

Deposition of Ge epitaxial layers on Ge and GaAs substrates by vacuum pyrolysis

Kenneth Zanio, Lewis Fraas, and Frans Krajenbrink

Hughes Research Laboratories, 3011 Malibu Canyon Road, Malibu, California 90265

(Received 23 August 1977; accepted 1 November 1977)

PACS numbers: 68.55.+b, 81.15.Gh

I. INTRODUCTION

C. E. Backus *et al.*¹ have noted that if a Ge cell and a GaAs cell are operated in tandem optically, the combined energy conversion efficiency can be as high as 33% without solar concentration. They also project that if these two cells are operated in combination with sunlight concentrated to 1000 suns (e.g., a power tower application), the limiting conversion efficiency will be 43%. These high conversion efficiencies have motivated us to study the epitaxial growth of Ge on GaAs and Ge substrates. Hopefully, these studies will lead to the fabrication of a Ge solar cell on the backside of a GaAs solar cell wafer. Fabricating such a device would require a Ge deposition process capable of producing semiconductor-quality Ge films at low temperatures and over large substrate areas.

Semiconductor-quality Ge layers have been epitaxially deposited on GaAs and Ge by the dihalide disproportionation reaction,² liquid epitaxy,³ vacuum deposition,⁴⁻⁶ and the decomposition of germane.^{7,8} Hydrogen reduction of tetrachloride has also been used to deposit Ge on GaAs.⁹ In the present study, Ge was epitaxially deposited onto Ge and GaAs substrates by the decomposition of germane. However, instead

of using a dilute germane in hydrogen mixture at 1 atm total pressure, germane was pumped through a decomposition chamber at low pressures by a turbomolecular pump.

II. THE DEPOSITION SYSTEM

A schematic of the deposition system used for the studies reported here is shown in Fig. 1(a). A decomposition chamber is contained within a vacuum chamber and germane is admitted into the decomposition chamber from an inlet located at the bottom of the chamber. Epitaxial growth occurs as the germane decomposes on the radiantly heated substrates. The residual H₂ and the unreacted GeH₄ are pumped out by the turbomolecular pump.

In the experimental system used, the decomposition chamber consisted of a quartz cup 7.5 cm in diameter and 10 cm in length with a 1-cm-diam gas inlet tube at the bottom. The top of this quartz cup was flared slightly and rested approximately 0.5 cm below the rotary plate. The turbopump was connected to an 18-in. (44.7 cm) stainless-steel chamber via a 6-in.-diam (15.2 cm) pump port.

The loading procedure is initiated by raising the top lid. Heater assemblies are mounted on the top lid and tilt up when

the lid is raised. After the substrates are loaded and the chamber is pumped down, a liquid nitrogen shroud (not shown) is filled and the substrates are thermally cleaned in a preheat position prior to deposition.

We have found that this GeH_4 vacuum deposition technique offers several advantages over other techniques. The vacuum-pyrolysis technique has the advantage of relatively low substrate temperature (525°C). This avoids the potential for degradation of the GaAs/GaAlAs substrate and the probable occurrence of interdiffusion and plastic deformation¹⁰ between the layers. The possibility of vapor back-etching, which is present in methods that utilize halogens, is eliminated. A notable advantage over standard hydrogen transport processes, which operate at 1 atm pressure, is that gas impurities can be routinely monitored with a residual gas analyzer. Residual gas pressures in the 10^{-8} Torr (10^{-6} Pa) range should then be routinely possible. In a later section, we provide a more detailed contrast between the vacuum pyrolysis and standard chemical vapor deposition (CVD) processes. When compared to vacuum-evaporation methods, the vacuum-pyrolysis technique has the advantage that contaminants originating from a hot Ge evaporation source are eliminated.

III. EXPERIMENTAL RESULTS

Layers $1\ \mu\text{m}$ thick were epitaxially deposited on (100) GaAs and Ge substrates. The GaAs wafers were purchased from and polished by Crystal Specialties, Inc. Before these wafers were loaded, they were given a light etch in methanol bromine and then spun dry. A 5.0-cm-diam, 1.5-mm-thick wafer of intrinsic high-purity Ge was obtained from John Ewins of the University of California, Lawrence Livermore Laboratory. Samples $1 \times 1\ \text{cm}$ were diced from this wafer and then lapped, etched in CP4, rinsed, and blown dry. After loading, the vacuum chamber was pumped down to 5×10^{-8} Torr (6.6×10^{-6} Pa). Before the deposition, the samples were given a thermal etch at approximately 550°C . For a substrate temperature of 525°C and a decomposition chamber pressure of about 5×10^{-3} Torr (6.6×10^{-1} Pa), (corresponding to a gas flow rate of $12\ \text{cm}^3/\text{min}$ at STP) the growth rate was $2.0\ \mu\text{m}/\text{h}$. Although epitaxy was achieved on both types of substrates, a smoother surface was obtained for Ge (Fig. 2). The deposition on GaAs was more faceted and illustrates the four-fold symmetry of the substrate.

Hall-effect measurements were made on layers deposited on the Ge substrates. Separate measurements on the substrates showed them to be n -type above 225 K (resulting from intrinsic conduction) and p -type below 150 K (resulting from a shallow level at a concentration of $6 \times 10^{10}\ \text{cm}^{-3}$). At room temperature, the substrate dominates the electrical properties of the film-substrate structure and the structure is n -type. However, just below room temperature, the substrate carrier concentration drops markedly (Fig. 3) with the result that the film dominates the substrate-film electrical properties between 100 and 250 K. Below 100 K, the electrical properties of the film are masked by the high mobility of holes from the high purity substrates, and the film appears to be p type. However, an analysis of the two-layer structure¹¹ shows that the film is actually n type. Raw experimental data for the

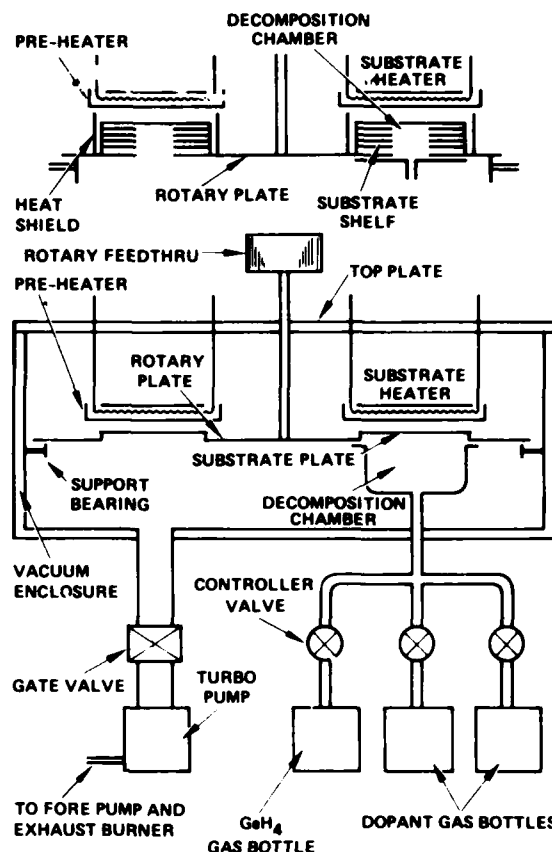


Fig. 1. Deposition system used in the vacuum pyrolysis technique for growing epitaxial layers of Ge by the decomposition of GeH_4 .

substrate only and calculated data for the film using the two-layer analyses are shown in Fig. 3. The free electron concentration (top) for the films is about $5 \times 10^{16}\ \text{cm}^{-3}$ at the lower temperatures. The mobility (bottom) of about $1500\ \text{cm}^2/\text{Vs}$ at lower temperature is also consistent with scattering by $10^{17}\ \text{cm}^{-3}$ ionized impurities¹² in single-crystal Ge. The germane gas may be the source of this n -type impurity since the gas used was only 99.99% pure (99.999% pure gas can be purchased).

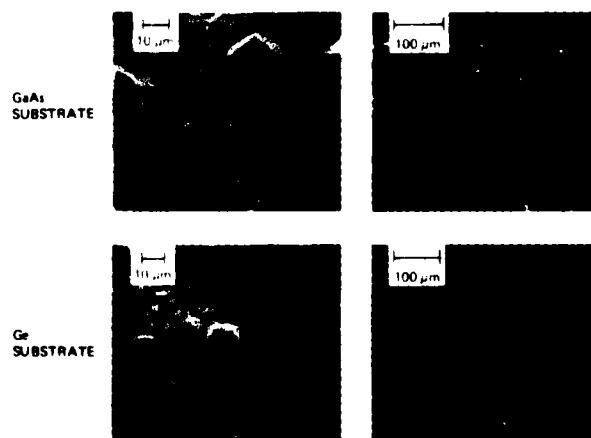


Fig. 2. SEM pictures of $1\text{-}\mu\text{m}$ -thick films of Ge epitaxially deposited on (100) GaAs (top) and Ge (bottom) substrates by the vacuum pyrolysis technique.

IV. DISCUSSION

In the system design shown in Fig. 1(a), the highest GeH_4 pressure obtainable in the pyrolysis chamber was 5 μm . Since for each surface collision there is a small probability that a GeH_4 molecule will react to form a Ge adsorbed atom, higher pyrolysis-chamber pressures are desirable. This can be done using the vacuum chamber and pyrolysis chamber design shown in Fig. 1(b). In this revised design, the pyrolysis chamber sits on top of a rotary plate. The gas bleed-in line terminates in the vacuum chamber with a flat top plate. This plate can be adjusted to within a small distance of the rotary plate. The hole in the bottom of the pyrolysis chamber is approximately 2.5 cm in diameter, which is small in comparison to the diameter of the pumping port. The small adjustable gap between the gas bleed-in top plate and the rotary plate allows a high pressure ratio to be established between the decomposition chamber and the outer vacuum chamber.

It is interesting to contrast the vacuum pyrolysis system described here with (1) the low-pressure CVD system^{13,14} used for polysilicon, in which SiH_4 is pumped through a hot-wall quartz reactor tube with a roughing pump, and (2) the standard 1-atm carrier gas CVD system. The key pressure parameters (i.e., system base pressure, reactant gas pressure, and carrier gas pressure) are summarized in Table I for these three systems. In the low-pressure CVD system, reducing the carrier gas pressure relative to the pressure in the standard CVD system, significantly reduces production cost for low film-purity coating requirements. The major reason for this cost breakthrough is the very high packing density available in low-pressure CVD systems resulting from stand-up, closely packed wafer loading. Basically, this close-packed loading capability results because of the small reaction probability per collision at the gas-solid interface. Thus, the gas-phase mass-transfer limitation on reaction rate in standard CVD does not apply. In a low-pressure system, the deposition-rate-limiting step is not the gas-transport step, but rather the surface chemical reaction step.

The problem with the low-pressure CVD system when applied to semiconductor-purity films is to assure high purity. Oil backstreaming and the inability to monitor impurities in the gas stream down to 1 ppm are well known disadvantages.

The vacuum CVD process described here overcomes these disadvantages. Referring to Table I, the vacuum CVD system operates much as the low-pressure CVD system in that the carrier gas pressure is markedly reduced. This potentially allows stacked wafer geometries. However, in vacuum CVD, the turbopump reduces the residual gas pressure four orders of magnitude below the residual gas pressure found in low-pressure CVD.

TABLE I. Key pressure parameter contrasting alternative CVD systems.

System	Base impurity pressure (Torr)	Reactant gas pressure (Torr)	Carrier gas pressure (Torr)
CVD	10^{-3}	10^{-1}	760
Low-pressure CVD	10^{-3}	10^{-1}	10^{-1}
Vacuum CVD	10^{-7}	10^{-1}	10^{-1}

V. CONCLUSION

These studies demonstrate that 1- μm -thick epitaxial films of Ge can be deposited onto both Ge and GaAs substrates at 525°C via a novel vacuum pyrolysis process. Additional studies to determine the nature of the impurity controlling the conductivity of the films are needed. If the vacuum pyrolysis technique proves capable of producing a variety of semiconductor-quality thin films, the technique should be capable of producing relatively large-area devices in high volume. This feature is particularly attractive for solar cell applications.

ACKNOWLEDGMENT

The authors are grateful for valuable discussions with R. Baron, R. Knechtli, P. Hilton, and J. Backus. We also ac-

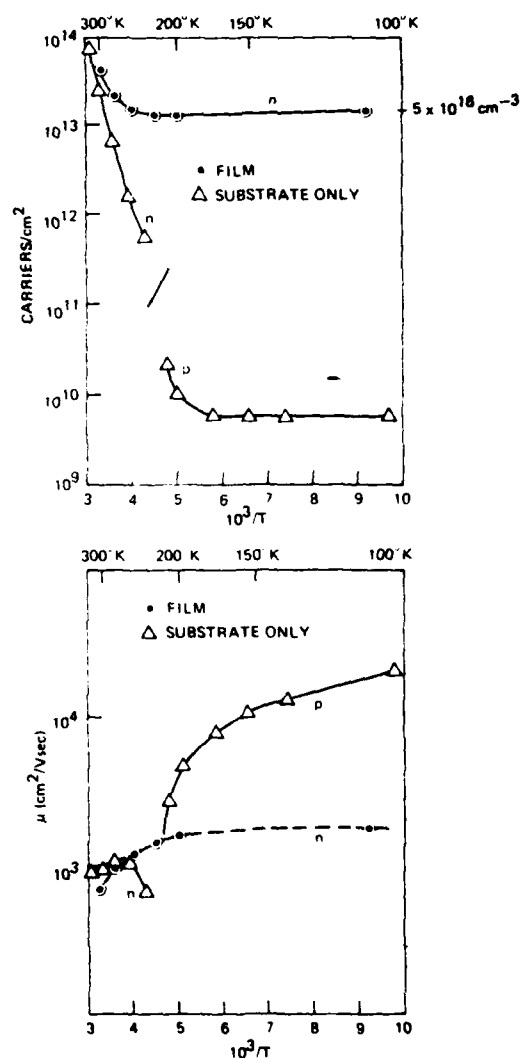


Fig. 3 (Top) free carrier concentration in units of cm^{-2} for a high-purity Ge substrate as determined by Hall analysis and for a 1- μm -thick Ge film on that substrate. The electron concentration for the film at the lowest temperature in units of cm^{-3} is $5 \times 10^{18} \text{ cm}^{-3}$ (Bottom) corresponding mobility data

knowledge the technical assistance of P. Hoberg and H. Montano.

¹N. S. Alvi, C. E. Backus, and C. W. Masden, *12th IEEE Photovoltaic Specialist Conference* (IEEE, New York, 1976) p. 948.

²M. Berkenblit, A. Reisman, and T. B. Light, *J. Electrochem. Soc.* **115**, 969 (1969).

³F. E. Rosztoczy and W. W. Stein, *J. Electrochem. Soc.* **119**, 1121 (1972).

⁴A. P. Klimenko, V. P. Klochkov, N. N. Soldaterko, N. M. Torchun, and Yu. A. Tkhorik, *Sov. Phys.-Crystall.* **13**, 303 (1968).

⁵V. Tybka, E. Dudrova, Z. Sevcik, and P. Krejci, *Thin Solid Films* **8**, R7 (1971).

⁶R. F. Lever and E. J. Huminski, *Appl. Phys.* **37**, 3638 (1966).

⁷S. A. Papasian and A. Reisman, *J. Electrochem. Soc.* **115**, 965 (1968).

⁸M. Davis and R. F. Lever, *J. Appl. Phys.* **27**, 835 (1956).

⁹G. O. Krause, and F. C. Teague, *Appl. Phys. Lett.* **11**, 251 (1967).

¹⁰T. B. Light, M. Berkenblit, and A. Reisman, *J. Electrochem. Soc.* **115**, 969 (1968).

¹¹R. L. Petritz, *Phys. Rev.* **110**, 1254 (1958).

¹²P. Debye and E. M. Conwell, *Phys. Rev.* **93**, 693 (1954).

¹³R. S. Rosler, *Solid State Technol.* **20**, 63, (1977).

¹⁴M. Ogirima, H. Saida, M. Suzuki, and M. Maki, *J. Electrochem. Soc.* **124**, 930 (1977).

APPENDIX C

DESIGN OF HIGH EFFICIENCY MONOLITHIC STACKED MULTIJUNCTION SOLAR CELLS

DESIGN OF HIGH EFFICIENCY MONOLITHIC STACKED
MULTIJUNCTION SOLAR CELLS

L. M. Fraas and R. C. Knechtli

Hughes Research Laboratories
Malibu, California 90265

ABSTRACT

An (AlGa)As-GaAs-Ge dual junction cell is an attractive implementation of the high efficiency stacked multijunction solar cell concept. Such a cell can be made monolithically by depositing GaAs and Ge layers epitaxially on the back side of a state-of-the-art AlGaAs/GaAs solar cell. This provides two photo-voltaically-active junctions, in the GaAs and in the Ge respectively. We note that the short circuit current available to the GaAs and to the Ge junction are nearly equal under space (AMO) illumination. This permits efficient operation of both junctions in series connection. We describe alternate means of series connecting these two junctions. We also note that Ge layers have been epitaxially deposited on GaAs by various methods at relatively low temperatures, so that the AlGaAs/GaAs cell is not expected to degrade as a result of the Ge layer growth. We briefly describe a low-temperature, low-pressure CVD method by which we have deposited epitaxial layers of Ge on GaAs substrates. We also describe a monolithic three-junction solar cell structure potentially capable of even higher conversion efficiencies.

1. INTRODUCTION

The idea of obtaining very high energy conversion efficiencies by optically stacking solar cells with different bandgaps is an old one. There is, however, increasing motivation to consider fabricating such a stack of solar cells monolithically on a single wafer. This follows for space applications because a single wafer is lighter than a multiple wafer stack, and for terrestrial applications using concentrator systems, because a single wafer is likely to be cheaper, simpler, and more easily cooled than is a multiple wafer stack. There are, however, major constraints on the design and fabrication of such a high efficiency monolithic stacked multijunction solar cell. Two design constraints are, first, that the different semiconductor materials making up the stack be nearly lattice matched so that crystal integrity can be maintained, and second, if the light sensitive junctions are to be series connected, that the material bandgaps be such that the light generated current be distributed approximately equally between the multiple junctions. A corollary problem is that of providing the desired series connection of the active junctions

without suffering unacceptable voltage losses at inactive junctions, in the stacked structures to be considered. In this paper, we first describe three monolithic multijunction solar cell structures which meet these design constraints (Section 2). We then make efficiency projections for these cells (Section 3), and finally, we comment on cell fabrication procedures and problems (Section 4).

2. ALTERNATIVE MULTIJUNCTION CELL STRUCTURES

The three monolithic multijunction structures to be described herein are shown schematically in Figure 1. In Figures 1(a) and 1(b), we show two monolithic AlGaAs/GaAs/Ge dual-junction cells. These cells differ in that they use fundamentally different electrical contacting schemes. In Figure 1(c), we show a monolithic CdZnS/InGaP/GaInAs/Ge three-junction cell.

High efficiencies can be projected if a GaAs cell is stacked with a Ge cell (see Section 3). We observe, furthermore, that Ge is lattice matched to GaAs to 0.1%. It should therefore be possible to fabricate a monolithic dual junction cell by simply fabricating a Ge booster cell on the backside of an existing already-developed AlGaAs/GaAs cell.

Turning now specifically to the cell structure of Figure 1(a), we envision first fabricating a shallow homojunction p AlGaAs/n GaAs solar cell on the frontside of a semi-insulating GaAs wafer followed by the fabrication of a shallow homojunction Ge solar cell on the backside of the same wafer. We propose using interdigitated p and n contact grids for each cell. For the grid to the buried layer, channels would be etched through the top p layer exposing the buried n layer for contacting. Since the buried layer can be made relatively thick, fewer contact fingers will be required in the grid for that layer and the shadow losses associated with this grid can be kept well below those shadow losses associated with the standard top layer grid.

The cell of Figure 1(b) differs from that of Figure 1(a) in that the interdigitated contact structure is no longer used. Instead, the p AlGaAs/n GaAs shallow homojunction cell is fabricated on the front side of an n-type GaAs wafer and a Ge shallow homojunction cell is fabricated on the back. The two cells are series connected through an n+/p+ GaAs tunnel junction fabricated on the backside of the wafer prior to the fabri-

cation of the p GaAs/n Ge cell. The tunnel junction functions qualitatively as a low series resistance interconnect because the n and p layers are doped to degeneracy and behave approximately like metallic contact layers. These contact layers are, however, special in that they are optically transparent single-crystal layers. More detail on the tunnel junction will be given in Section 4.

In terms of ease of fabrication, the dual junction cell of Figure 1(a) is probably the simplest possible monolithic multijunction cell, i.e., it builds on an existing cell, it uses the minimum number of additional epitaxial layers, and it builds with an elemental semiconductor. The dual-junction cell of Figure 1(b) is the next most complicated cell, but with the additional tunnel junction layers, the crucial building block required to go from a dual junction cell to a cell with three or more active junctions becomes apparent. This brings us to the three-junction cell of Figure 1(c). Each additional cell in this structure is formed with n/n/p building blocks. Specifically, the lowest bandgap cell is fabricated in the Ge wafer, the next cell is fabricated in GaInAs (with the n/n/p building block) and the last and highest bandgap cell is fabricated in GaInP. Finally, the whole structure is capped with an n CdZnS or indium tin oxide (ITO) transparent window layer. Because of the large number of layers involved in this structure, and because of the abrupt doping profiles required at the tunnel junctions, a new epitaxial crystal growth technology will, however, have to be developed. One possible approach is outlined in Section 4.

Now that we have described the structures of Figure 1, we note that the layers involved are all lattice matched to within 1%. We document this point in Table 1. In this context, the low mismatch between Ge and GaAs is again especially attractive. In the next section we shall show that the material bandgaps are also suitable for reasonably uniform current distribution among the junctions for each multijunction structure.

3. MULTIJUNCTION CELL EFFICIENCY PROJECTIONS

In this section, we begin by considering the current distribution in the active junctions of the cells of Figure 1. We then derive values for operating voltages, and finally, we conclude with cell efficiency projections.

a. Light Generated Current Optimization

In order to address the problem of light generated current distribution in a multijunction cell, in Figure 2 we present the cumulated photon flux (converted to short circuit current) versus wavelength for the AMO and AM1.5 solar spectra. The short-circuit current listed at each wavelength is the integrated short-circuit current from the long-wavelength end of the solar spectrum up to the listed wavelength. These curves were calculated from the AMO data of M. P. Thekarkara (1) and the AM1.5 data of Brandhorst (2).

In this paper, we shall study the AlGaAs/GaAs/Ge dual-junction cell under most conservative conditions, i.e., for the space application using the AMO spectrum. Alternately, we shall study the ITO/InGaP/GaInAs/Ge three-junction cell for the terrestrial application using the AM1.5 spectrum. In the AMO spectrum of Figure 2(a), we have noted the bandgap positions of AlGaAs, GaAs, and Ge, and similarly, in the AM1.5 spectrum of Figure 2(b), we have noted the bandgap positions of ITO, CdZnS, InGaP, GaInAs, and Ge. (The ternary layer compositions are those shown in Table 1.) From the curves of Figure 2, we extract the short-circuit currents available at each active junction under ideal conditions. Thus, for example, for the dual junction cell, 33 mA/cm² (107-74) are generated at the GaAs junction while 35 mA/cm² (74-39) are generated at the Ge junction (assuming direct gap absorption only). Similarly, 14 mA/cm² (41-27) are generated at the GaInAs junction in the three-junction cell. And so on. These available short circuit currents are given in Table 2.

In order to arrive at a value for the operating current for the multijunction cell, we observe that because of series interconnections, the current will be limited by the cell with the lowest short circuit current. For simplicity, we shall therefore operate that lowest current junction at its maximum power point. The other junctions in the stack then simply boost the output voltage. While this does not lead to an exact optimization for maximum power conversion efficiency, this is a good enough approximation for the present estimates. For the AlGaAs/GaAs/Ge dual junction cell, the AlGaAs/GaAs cell is the lowest current cell and therefore the GaAs/Ge cell is the booster cell. From our measurements, as well as from reference (3), we can estimate the optimum operating current of a good GaAs solar cell to be approximately 0.95 times its short circuit current. Taking $I_{sc} = 33 \text{ mA/cm}^2$ as per Table 2 leads to an optimum operating current of $0.95 \times 33 = 31.4 \text{ mA/cm}^2$.

For the three junction cell, the GaInAs junction limits the cell current and because its bandgap is near that of GaAs, the optimum operating current for this cell will again be approximately 0.95 times its short circuit current, i.e., $0.95 \times 14 = 13.3 \text{ mA/cm}^2$.

b. Cell Operating Voltages

Having arrived at values for junction short circuit currents and operating currents, the operating voltage at each junction can be calculated from the expression

$$V_{op} = \frac{kT}{q} \ln \left(\frac{I_{sc} - I_{op}}{I_{00}} \right) \quad (1)$$

This equation assumes that the junction dark current is diffusion limited in the calculated operating voltage region. For the dual junction cell, this assumption is reasonable because LPE GaAs is of high quality and because the Ge bandgap is low. For the three junction cell, this assumption is reasonable if it is used under concentrated sunlight

because diffusion currents dominate at the high current levels encountered under concentrated sunlight conditions.

In order to calculate operating voltages from Eq. 1, we need values for the diffusion limited dark current, I_{00} . For GaAs, an I_{00} value of 2×10^{-19} A/cm² is typical. We arrive at this value of I_{00} for GaAs by noting that our GaAs concentrator solar cells typically have an open circuit voltage of 1.1V when the short circuit current is 2 amps. Assuming the forward current is diffusion limited in this voltage and current range, we calculate an I_{00} from

$$V_{oc} = \frac{kT}{q} \ln \frac{I_{sc}}{I_{00}} \text{ of } 2 \times 10^{-19} \text{ A/cm}^2.$$

We verify the diffusion limited current assumption by noting that V_{oc} vs \ln (solar concentration ratio) graphs give a slope of kT/q . Since the diffusion current scales with bandgap as $1/E_g/kT$, we can calculate values of I_{00} for the different materials used for the relevant junctions. Then, from these values and the values of I_{sc} and I_{op} given in the last section, we can calculate junction operating voltages. In this calculation, we assume 1 sun at AMO for the AlGaAs/GaAs/Ge dual junction cell. For the three junction cell, we assume 1 sun and 300 suns concentration at AM1.5 (terrestrial applications). The corresponding operating voltages V_{op} are given in Table 3.

The calculated operating voltage for the dual junction cell is 1.1 V. The projected operating voltage for the three junction cell is 2.13 V and 2.55 V for 1 and 300 suns respectively. We observe that the operating voltage increases with concentration ratio (CR) as $3 \times (1/40 \text{ V}) \times \ln \text{CR}$, i.e., for three junctions, the voltage increases 3 times faster with solar concentration than for a single junction cell.

c. Projected Energy Conversion Efficiencies

From the operating voltage and current, the multijunction cell efficiency is readily calculated. Thus, for the dual junction cell, the conversion efficiency projected under space illumination and no solar concentration is:

$$\eta = \frac{31.4 \text{ mA/cm}^2 \times 1.1 \text{ V}}{135 \text{ mW/cm}^2} = 25.6\% \text{ at AMO, 1 sun}$$

For the three junction cell, the conversion efficiency projected under terrestrial illumination is:

$$\eta = \frac{13.3 \text{ mA/cm}^2 \times V_{op}}{84 \text{ mW/cm}^2} = \begin{cases} 33\% \text{ at 1 sun, AM1.5} \\ 40\% \text{ at 300 suns, AM1.5} \end{cases}$$

4. CELL FABRICATION

The severity of the fabrication problem for a multijunction cell will vary depending on its structure. The dual junction cell of Figure 1(a) builds on an existing cell and avoids the tunnel

junction fabrication problem. The successful fabrication of this cell will depend on the fabrication of the GaAs/Ge cell. In this regard, Ge epitaxial layers have been deposited on GaAs substrates by several groups. (4-12) Furthermore, spectral response (13) and open circuit voltages (14) have already been reported for the GaAs/Ge heterostructure. The structure of Figure 1(a) may therefore be the one which can most readily be implemented with the existing state-of-the-art.

The structure of Figure 1(b) does not only provide an alternative to the structure of Figure 1(a), it also addresses a key problem inherent in the highest efficiency multijunction cells of the type of Figure 1(c), i.e., cells with more than 2 active junctions. In these cells, one must fabricate tunnel junctions with abrupt dopant profiles and maintain those profiles throughout subsequent epitaxial layer processing. A key problem, then, is the development and application of low temperature epitaxial layer growth technologies. Herein, we first quantify this by examining the tunnel junction series resistivity problem. We then describe briefly two low temperature growth technologies, i.e., molecular beam epitaxy (MBE) and a variant of low pressure chemical vapor deposition (vacuum CVD).

a. Tunnel Junction Series Resistance

In the structures of Figures 1(b) and 1(c), the active junctions are coupled by tunnel junctions, and in the efficiency projection of Section 3, we assumed that the voltage drop across each n^+p^+ tunnel junction is zero. Here, we examine that assumption. At each n^+p^+ junction, carriers tunnel through a barrier of a certain height and width. The barrier height and width determine the resistivity at the tunnel junction.

Kane (15) has presented a theory of tunneling. For a direct gap semiconductor, one can write

$$\frac{J_t}{V} = \frac{q^2 \sqrt{2m^*}}{4 \hbar^2 w} E_g^{1/2} \exp\left[-\frac{4 \sqrt{2m^*} E_g^{1/2} w}{3 \hbar}\right] \quad (2)$$

where m^* is the tunneling particle mass, w is the barrier width, E_g is the material bandgap or barrier height, V is the voltage drop across the tunnel barrier, and, of course, J_t is the tunneling current density. Expressing m^* in electron masses, E_g in electron volts, and w in angstroms, this expression reduces to

$$\frac{J_t}{V} = 10^{11} \left(\frac{\text{amps}}{\text{cm}^2 \text{ V}} \right) \sqrt{m^* E_g} \frac{1}{w} \exp(-0.68 \sqrt{m^* E_g} w) \quad (3)$$

The resistivity curve calculated from this equation for GaAs is presented in Figure 3. Equation (3) is accurate with the proviso that the constant, 0.68, can vary slightly depending on the barrier shape (16). For this reason, the curve of Figure 3 was calculated assuming an E_g of 1.4 eV and an m^* such that the curve passes through the resistivity point reported by Hononyak for a GaAs tunnel diode (17). The resultant m^* value of 0.03

is quite reasonable. We have verified the validity of this curve by plotting on this same curve some experimental tunnel junction data points obtained on structures fabricated at our laboratories.

From the curve in Figure 3, we now make several observations. First, the junction resistivity is extremely sensitive to barrier width, W . In fact, the resistivity varies by one order of magnitude if W varies by 20 Å. Second, the doping density must be quite high. To quantify this, in Figure 3, we have plotted the equivalent doping density, $N^* = N_A N_D / (N_A + N_D)$, as well as w assuming step function dopant profiles. Third, we observe that the process temperature must be low enough to avoid chemical diffusion distances much in excess of approximately 20 Å, to keep W effectively small.

Equation 1 allows us to make one final observation. It is much easier to make a tunnel junction in a low bandgap material than in a high bandgap material. For this reason, we observe that for our proposed three junction cell, we place the tunnel junction coupling to the highest gap cell at the heterojunction interface between InGaP and GaInAs. The relevant barrier height is then the lower bandgap of GaInAs, e.g., 1.25 eV. However, in this case the n layer in GaInAs must be much thinner than an optical absorption length, typically < 1000 Å.

The data points in Figure 3 serve to verify Eq. 3. From Eq. 3, we can now look specifically at the voltage drops across the tunnel junctions for the structures of Figure 1(b) and 1(c). Thus, first, for the dual junction cell, in space, we calculate that for a N^* of $4 \times 10^{18}/\text{cm}^3$, $w = 141$ Å and

$$\begin{aligned} V &= \frac{J_t w}{8 \times 10^{10}} \exp(0.138 w) \\ &= \frac{31 \times 141}{8 \times 10^{10}} \exp(0.138 \times 141) \\ &= 15 \text{ mV.} \end{aligned}$$

This may be compared with a value of 50 mV recently measured at Hughes on an experimental structure. Turning to the three junction cell, the voltage drop will be highest across the highest bandgap tunnel junction (GaInAs). For a N^* of $7.5 \times 10^{18}/\text{cm}^3$, $w = 103$ Å and 300 suns, we calculate that

$$\begin{aligned} V &= \left[\frac{13 \times 103}{8 \times 10^{10}} \exp(0.130 \times 103) \right] \times 300 \\ &= 3.3 \text{ mV} \end{aligned}$$

b. Low Temperature Epitaxial Growth

Semiconductor quality epitaxial layers of GaAs, InP, InGaAs, GaAsP, Si, and Ge have been grown at low temperatures by molecular beam epitaxy (18). Furthermore, n^+ GaAs layers doped to $1 \times 10^{19}/\text{cm}^3$ and p^+ GaAs layers doped to $3 \times 10^{19}/\text{cm}^3$ have been prepared (18). These

dopant values could lead to a tunnel junction N^* of $7.5 \times 10^{18}/\text{cm}^3$. Therefore, this technique provides an excellent research tool for the investigation of multijunction solar cells.

Unfortunately, MBE will not allow device production in the volumes required for practical solar cell applications. CVD processes are commercially viable, but operate at high substrate temperatures. To illustrate this high temperature processing problem, we observe that metal organic CVD could readily be applied to the deposition of multiple III-V layers of varying compositions. However, for p^+ films grown by this process, a dopant like Zn diffuses much too fast and a dopant like Cd will diffuse 10 Å in 25 sec at 725°C, a typically required growth temperature. We have noted that, for Ge films prepared by GeH_4 pyrolysis the growth temperature can be lowered by lowering reactant gas pressures and residual gas pressures below those used in conventional CVD (4). The resultant vacuum CVD process may, then, be applicable to the production of multijunction solar cells (4). Returning to the MO-CVD example with Cd doping, if the process temperature can be lowered to 600°C via low pressure MO-CVD, Cd will take 1 hour to diffuse 10 Å.

5. CONCLUSIONS

We have shown that material combinations exist which potentially allow the fabrication of monolithic stacked multijunction solar cells. Lattice matching and equal current distributions are possible. For space applications, we calculate an efficiency for the AlGaAs/GaAs/Ge dual junction cell of 25.6%, and for terrestrial application with 300 suns concentration, we calculate an efficiency of 40.4% for the CdZnS/InGaP/GaInAs/Ge cell. We have noted that low epitaxial growth temperatures are required for device fabrication and that MBE should allow a means of making these cells a reality. The challenge will be to develop a scalable low temperature growth technology.

REFERENCES

1. M.P. Thekaekara, *Solar Energy* **14**, 109 (1973).
2. H.W. Brandhorst, Jr., "Terrestrial Photovoltaic Measurement Procedures," ERDA/NASA/1022-77/16, NASA TM 73702 (1977).
3. H.J. Hovel, *Solar Cells*, Vol. 11 of *Semiconductors and Semimetals*, (Academic Press, New York, 1975).
4. K.W. Zanio, L.M. Fraas and F.G. Krajenbrink, *J. Vac. Sci. Technol.* **15**, 119 (1978).
5. M. Berkenblit, A. Reisman, and T.B. Light, *J. Electrochem. Soc.* **115**, 969 (1969).
6. F.E. Rosztoczy and W.W. Stein, *J. Electrochem. Soc.* **119**, 1121 (1972).

7. A.P. Klimenko, V.P. Klochkov, N.N. Soldaterko, N.M. Torchun, and Yu. A. Tkhorik, *Sov. Phys-Crystall.* **13**, 303 (1968).
8. V. Rybka, E. Dudrova, Z. Sevcik, and P. Krejci, *Thin Solid Films* **8**, R7 (1971).
9. R.F. Lever and E.J. Huminski, *J. Appl. Phys.* **37**, 3638 (1966).
10. S.A. Papazian and A. Reisman, *J. Electrochem. Soc.* **115**, 965 (1968).
11. M. Davis and R.F. Lever, *J. Appl. Phys.* **27**, 835 (1956).
12. G.O. Krause and F.C. Teague, *Appl. Phys. Lett.* **11**, 251 (1967).
13. R.L. Anderson, *Solid State Electron.* **5**, 341 (1962).
14. A.S. Aseev, Y.N. Pogorelov, S.I. Stenin, and V.N. Shumsky, *Thin Solid Films* **32**, 351 (1976).
15. E. O. Kane, *J. Appl. Phys.* **32**, 83 (1961).
16. S.M. Sze, *Physics of Semiconductor Devices*, p. 163, Wiley-Interscience (1969).
17. N. Holonyak, Jr., and I.A. Lesk, *Proc. IRE* **48**, 1405 (1960).
18. P.E. Luscher, *Solid State Technology* **20**, 43 (1977).

Table 1
Lattice and Bandgap Characteristics
of Semiconductor Layers

7637.2

	MATERIAL	BANDGAP E_g	COMPOSITION x	LATTICE CONSTANT	MISMATCH %
DUAL JUNCTION	Ge	0.66 (0.8)		5.658	
	GaAs	1.43		5.654	0.1
	$Al_{1-x}Ga_xAs$	2.9	0.1	5.661	0.1
THREE JUNCTION	Ge	0.66 (0.8)		5.66	
	$Ga_{1-x}In_xAs$	1.25	0.15	5.7	0.7
	$Ga_{1-x}In_xP$	1.77	0.55	5.67	0.6
	$Cd_{1-x}Zn_xS$	2.8	0.3	5.7	0.6
	(ITO)	3.1			

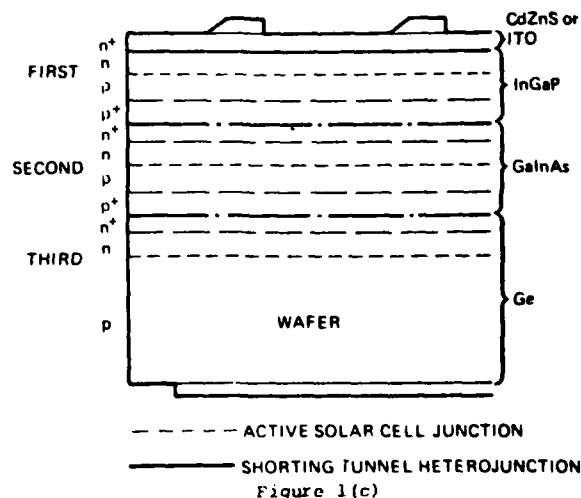
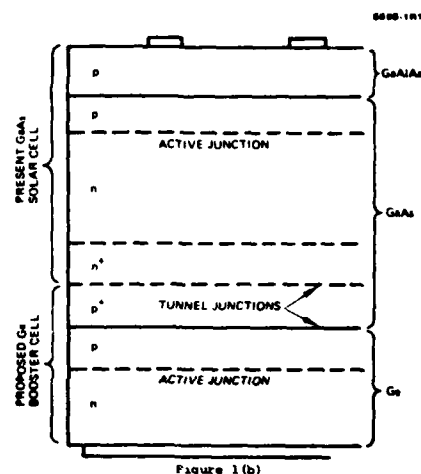
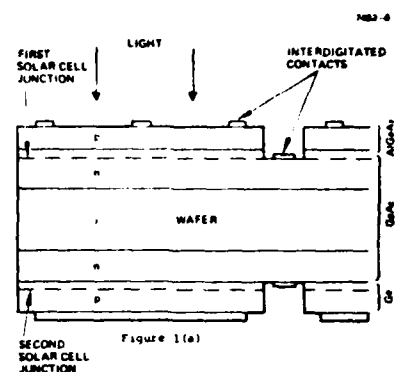


Figure 1. Alternate multijunction cell structures: (a) Dual junction cell with interdigitated electrical contacts; (b) Dual junction cell with tunnel junction series interconnect; and (c) stacked three junction cell.

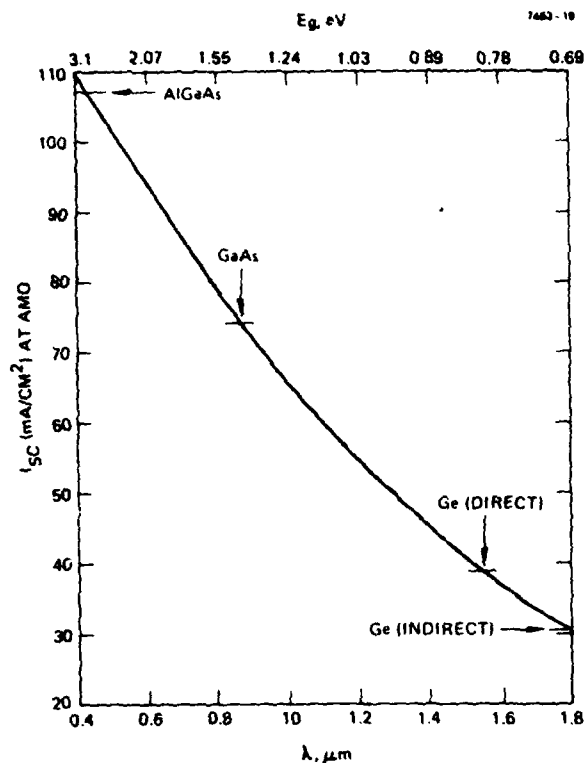


Figure 2(a)

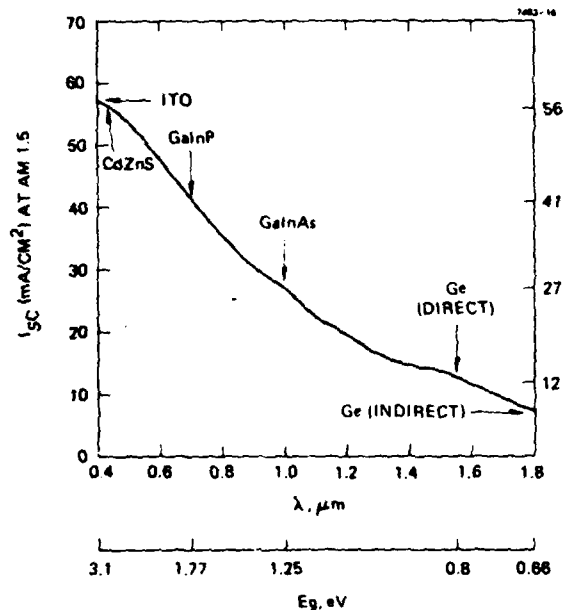


Figure 2(b)

Figure 2. Cumulated photon flux, converted to short circuit current as a function of wavelength for the (a) AMO and (b) AM1.5 solar spectra.

Table 2
Available Solar Cell Short Circuit Currents

DUAL JUNCTION CELL	I_{sc} (AMO)
AlGaAs/GaAs	33 mA/cm^2
GaAs/Ge	35 mA/cm^2
THREE JUNCTION CELL	I_{sc} (AM 1.5)
CdZnS/InGaP	15 mA/cm^2
InGaP/GaInAs	14 mA/cm^2
GaInAs/Ge	15 mA/cm^2

Table 3
Operating Characteristics for Solar Cell Junctions Discussed in Text

MATERIAL	I_{00}	V_{op} (AMO)	V_{op} (AM 1.5)	V_{op} (AM 1.5 300 suns)
GaAs	$2 \times 10^{-19} \text{ A}/\text{cm}^2$	0.9 V		
Ge	$1 \times 10^{-6} \text{ A}/\text{cm}^2$	0.2 V		
TOTAL		1.1 V		
InGaP	$6 \times 10^{-25} \text{ A}/\text{cm}^2$		1.23 V	1.38 V
GaInAs	$2 \times 10^{-16} \text{ A}/\text{cm}^2$		0.72 V	0.86 V
Ge	$1 \times 10^{-6} \text{ A}/\text{cm}^2$		0.17 V	0.31 V
TOTAL			2.13 V	2.55 V

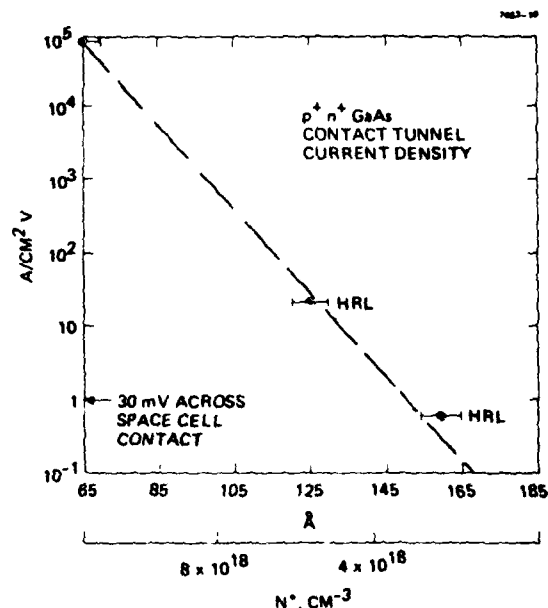


Figure 3. Gallium arsenide tunnel junction current density per volt as a function of barrier width.

5

The Electronic Structure of Grain Boundaries in Polycrystalline Semiconductor Thin Films

LEWIS M. FRAAS and KENNETH ZANIO

*Chevron Research Company
Richmond, California*

*Hughes Research Laboratories
Malibu, California*

5.1	Introduction	153
5.2	Internal Boundaries, Electronic Structure, and Electronic Transport	154
	1. Electronic Structure of a Dislocation	154
	2. Electronic Structure at a Free Surface	161
	3. Electronic Structure of a Grain Boundary	162
5.3	Grain Boundary Effects in Polycrystalline Thin-Film Devices	164
5.4	Measurement of Grain Boundary Structures	167
5.5	Grain Boundary Passivation	172
5.6	Conclusions	173
	References	174

5.1 INTRODUCTION

The revolution in solid-state electronics began with a theory of a perfect periodic lattice with donor or acceptor impurities. This theory allowed the development of bulk-effect devices such as junction diodes and bipolar transistors. Next, extension of the theory of the solid state to surfaces paralleled the development of surface-effect devices such as field-effect transistors (FETs) and charge-coupled devices (CCDs). In these two areas, semiconductor process development led to successful commercial devices because the solid-state theory provided predictability.

Polycrystalline semiconductor thin-film development, on the other hand, has proceeded by correlating process variables with device variables

APPENDIX E

ANALYSIS OF P-TYPE GaAs GROWN BY LOW PRESSURE
METAL ORGANIC CHEMICAL VAPOR DEPOSITION

ANALYSIS OF P-TYPE GaAs GROWN BY LOW PRESSURE METAL ORGANIC
CHEMICAL VAPOR DEPOSITION*

Ken Zanio
Hughes Research Laboratories
3011 Malibu Canyon Road
Malibu, CA 90265

ABSTRACT

Unintentionally doped p-type thin films of GaAs were grown by low pressure metal organic chemical vapor deposition. For growth near the Ga-rich three phase boundary, room temperature hole concentrations as high as $4 \times 10^{20} \text{ cm}^{-3}$ with corresponding mobilities of $30 \text{ cm}^2/\text{Vsec}$ were obtained. Carbon was the major impurity, but in concentrations less than the free hole concentrations. For growth away from the three phase boundary the hole concentration decreased, and an ionized impurity concentration ($N_A + N_D$) as low as $2 \times 10^{16} \text{ cm}^{-3}$ was obtained. Carbon and oxygen were the major impurities in concentrations much higher than $N_A + N_D$. When isolated antisite acceptors near the three phase boundary and neutral impurity complexes in near-stoichiometric material were considered to be the majority defects, a correlation between $N_A + N_D$ and the impurity content was found.

* Supported by AFOSR

1. INTRODUCTION

Metal organic chemical vapor deposition (MOCVD) is a well established technique for growing thin films of GaAs^{1,2,3}. Operating MOCVD systems at reduced pressure allows a lower substrate temperature and alleviates autodoping⁴. The characterization of GaAs thin films prepared by these MOCVD techniques has focused on n-type films for a variety of devices (e.g., FET's, Schottky diodes, TED's etc.). However, the characterization of p-type material is important for two reasons. First, p-type GaAs is becoming more important in devices such as solar cells, lasers, transistors and IMPATT's^{5,6}. Secondly, understanding the defect chemistry in p-type material should be helpful in reducing the total concentration of electrically active residual centers in GaAs. There is not a wealth of information in the literature regarding the characterization of p-type GaAs thin films prepared by MOCVD. Unintentionally doped GaAs prepared by vacuum technologies is predominantly p-type. In this paper we relate the impurity content of our p-type films to the electrical activity through an appropriate defect model.

2. THE MOCVD SYSTEM AND EXPERIMENTAL PROCEDURE

A schematic of the low pressure MOCVD system used to grow GaAs thin films is shown in Figure 1 (top). In this system, a 10% mixture of AsH₃ in H₂ from Scientific Gas Products and trimethylgallium (TMGa) from Alfa Ventron was bled into a vertical quartz reactor at a flow rate of about 50 cc/min. The gases impinged directly on the

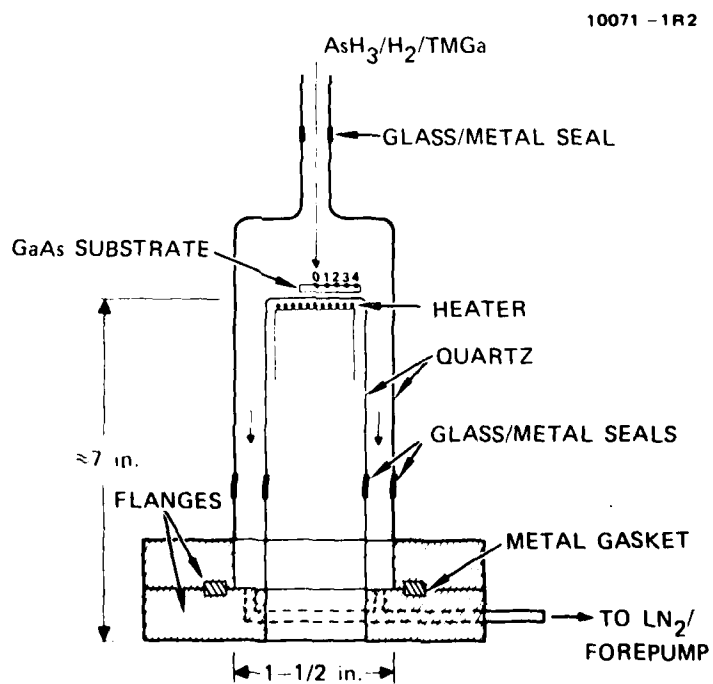
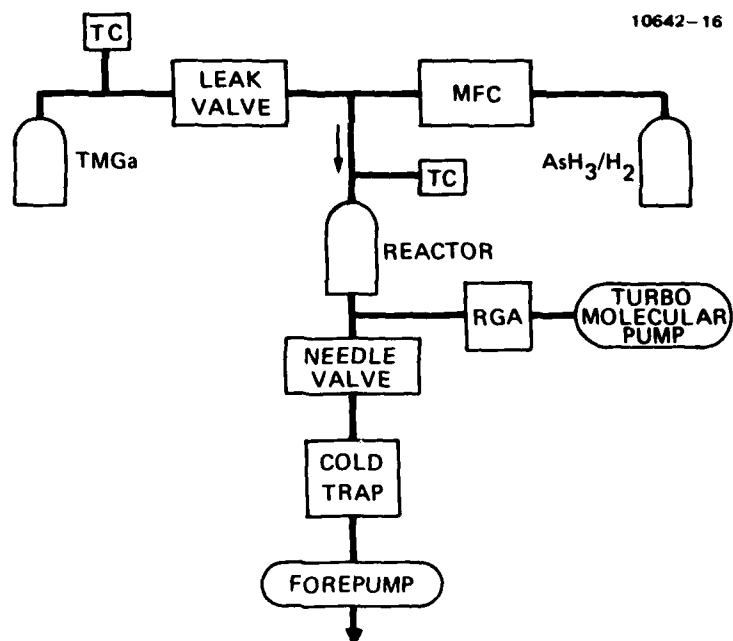


Figure 1. Schematic of LPMOCVD system (top) and reactor (bottom) used to grow GaAs films.

(100) semiinsulating GaAs and sapphire substrates. The substrates were radiatively heated by a coil located directly under the quartz pedestal. The coating of the sapphire could be observed during growth through the outer quartz wall. The H_2 and the gaseous by-products of the TMGa decomposition were pumped on by a Leybold Heraeus rotary vane pump. A working pressure of about 50 Torr, measured upstream from the reactor, was maintained by a needle valve located between the reactor and a cold trap. A residual gas analyzer pumped on by a Leybold Heraeus turbomolecular pump was used for leak checking. When the system was outgassed and leak checked the valve to the forepump was closed and the system was pumped on by the turbo-pump.

Before loading the GaAs substrates, the quartz pedestal was baked out in vacuum for 30 minutes at $550^{\circ}C$. The remainder of the system was baked out at about $100^{\circ}C$. After the reactor was cooled to room temperature, the system was backfilled with N_2 , and the outer quartz jacket was removed from the reactor. A wafer of GaAs approximately 2 cm by 1 cm and a sapphire disk approximately one centimeter on a side were placed on the quartz pedestal. Previous to loading, the GaAs wafers were given a 10 sec 0.1% bromine-in-methanol etch and blown dry in dry N_2 . After closing the reactor, the system was purged with AsH_3/H_2 and heated to the growth temperature. After about 20 min at $550^{\circ}C$, growth was initiated by introducing TMGa. After one to three hours, growth was terminated by stopping the TMGa flow. The substrate temperature was reduced to room temperature before turning off the AsH_3 .

Several preliminary runs were undertaken on sapphire substrates with large excess of Ga to locate the Ga-rich three phase boundary and establish growth conditions. After these preliminary runs the AsH₃-to-TMGa flow rate ratio ($F_{\text{AsH}_3}/F_{\text{TMGa}}$) was slightly increased to about 0.9. Using both (100) semi-insulating GaAs and sapphire substrates two runs were undertaken at $F_{\text{AsH}_3}/F_{\text{TMGa}} = 0.9$. Three runs were then taken at $F_{\text{AsH}_3}/F_{\text{TMGa}} = 3.7$. (For convenience we refer to growth at these conditions as flow rate ratios of one and four, respectively). To change $F_{\text{AsH}_3}/F_{\text{TMGa}}$, the TMGa flow was varied by about a factor of three. The exact ratio was established by adjusting the AsH₃ flow rate. Runs at low $F_{\text{AsH}_3}/F_{\text{TMGa}}$ lasted about one hour. To obtain the same film thickness, runs at higher $F_{\text{AsH}_3}/F_{\text{TMGa}}$ lasted about three hours. As expected, the film thickness was proportional to the TMGa flow rate. The films were examined by selective area electron diffraction (SAD), scanning electron microscope (SEM), x-ray Read, and x-ray topographs. The thickness of the layers was determined by SEM, staining cleaved sections, and sputter ion mass spectrometry (SIMS). The electrical properties were surveyed with a hot probe and Hall measurements. The impurity content of the films was examined by SIMS. Profiles were taken with a Cameca IMS-3f microanalyzer (Charles Evans and Associates, San Mateo, California). Samples were sputtered using Cs⁺ ion bombardment while monitoring negative secondary ions.

3. RESULTS

A. CRYSTAL PERFECTION AND MORPHOLOGY

Reactant gases entering the reactor impinged directly on the substrate and were not baffled. Therefore, gradients in the film thicknesses, especially at low ($F_{\text{AsH}_3}/F_{\text{TMGa}}$), were expected. The thicknesses of the films at $F_{\text{AsH}_3}/F_{\text{TMGa}}$ of four were about 3 μm and were tapered to about 2 μm at the edges. For the runs near the three-phase boundary (i.e., $F_{\text{AsH}_3}/F_{\text{TMGa}} \approx 1$), hillocks formed at the center of the wafer (Position 0 in Figure 1) where direct impingement of the reactive gases on the substrate occurred. Staining cleaved structures showed the hillocks to be about 30 μm thick. These films were about 6 μm thick near the periphery of the hillocks, tapering to about 3 μm at the edge of the wafer. Coverage also occurred on the bottom of the wafers because of a slight bow in the pedestal, and clearance between the pedestal and the wafer. Films on the bottom of the wafers were about 2 μm thick.

Scanning electron microscope pictures showed a variety of surface features for films prepared near the three-phase boundary. In the first run at the boundary, Ga balls and particulate matter, assumed to be carbon, were observed on the hillock. The presence of Ga balls in the first run established that growth occurred near the three phase boundary. The smoothness of the films improved at increasing distances away from the direct flow of the gases. Figure 2 shows SEM photographs of the films at different position. At Position 1 on the substrate the SEM shows only the crusty GaAs layer. Faceting is evident at Position 2. At Position 3 the onset of smooth layer growth was found. At Position 4 surfaces free from defects at

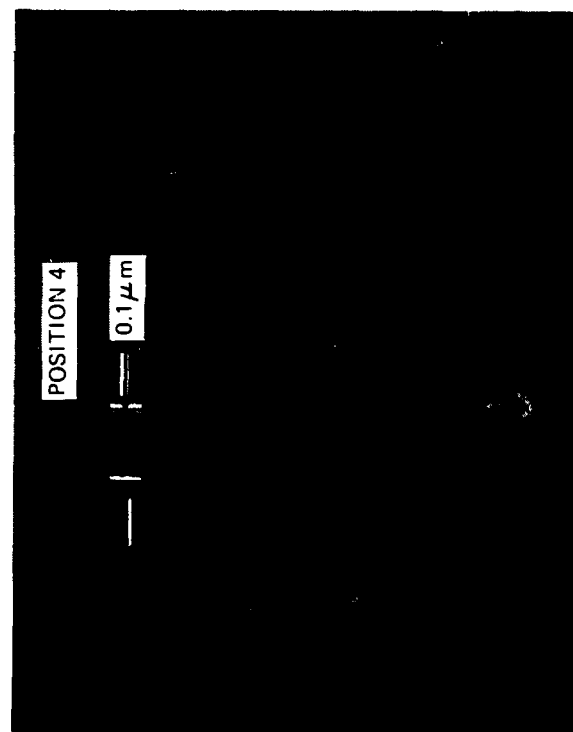
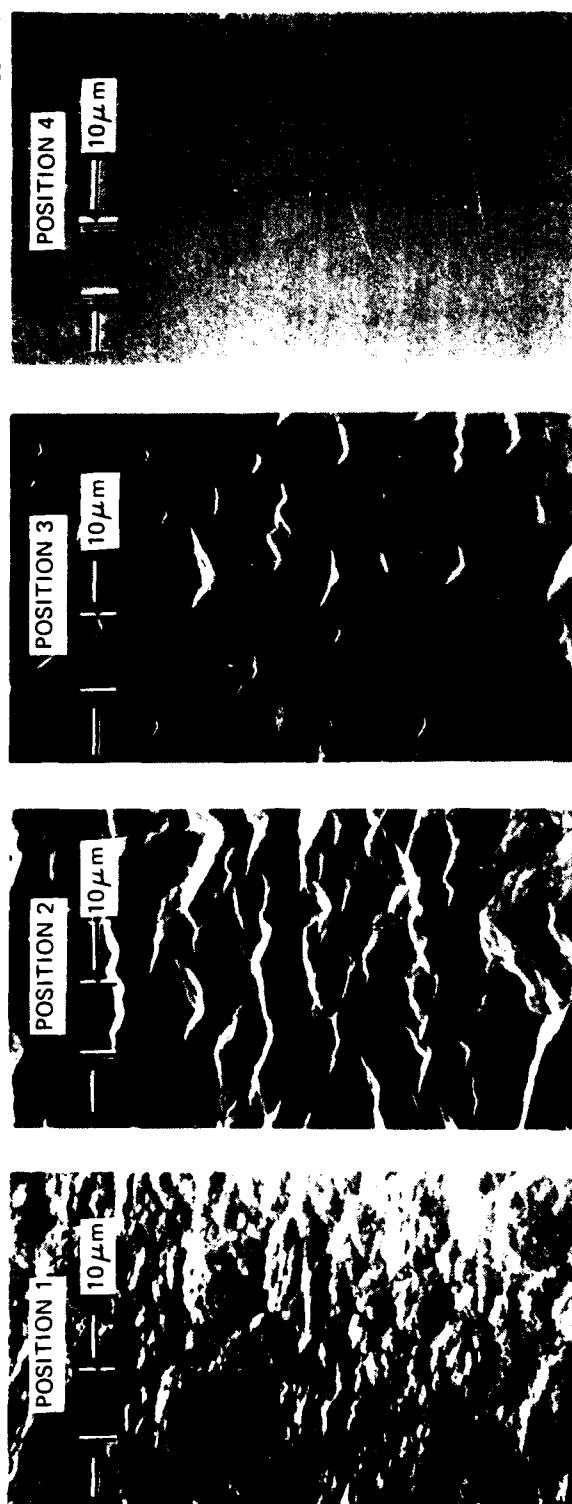


Figure 2.
SEM photographs at different positions of GaAs
film prepared on (100) substrate at $\text{F}_{\text{AsH}_3}/\text{F}_{\text{TNGa}}$
of one.

magnifications up to 100,000x were found. In Run 2 the distribution of surface features were the same but Ga balls and particulate matter were not found. The morphology of the backside of the wafers was most typical of Position 4. Films prepared at $F_{\text{AsH}_3}/F_{\text{TMGa}}$ of four were faceted. The surface morphology was most characteristic of Position 3.

A survey of all the films with SAD indicated single-crystal epitaxy. Except at the hillocks, SAD showed uniform channeling patterns. There was no difference in channeling patterns, either across a thin film, among the thin films, or between the thin films and a reference substrate. Although the channeling pattern is not a precise tool for evaluating the quality of the layers, it did show that except for the hillocks, epitaxy had been achieved over the entire wafer, and that an amorphous layer of significant thickness was not present.

X-ray Read pictures of regions characteristic of Position 2 showed both spots and rings characteristic of both single-crystal and polycrystalline materials. X-ray Read pictures at Position 4 and the bottom of the wafer showed only spots characteristic of single crystalline material. X-ray Read pictures of films prepared at $F_{\text{AsH}_3}/F_{\text{TMGa}}$ of four showed spots characteristic of single-crystal material. Defects were not apparent in an x-ray topograph of this material.

B. ELECTRICAL PROPERTIES

Van der Pauw measurements were made on 10 samples. These samples were characteristic of positions on the wafer having the best crystal perfection and as little faceting as possible. Hole concentrations at $F_{\text{AsH}_3}/F_{\text{TMGa}}$ of one ranged from 6×10^{19} to $4 \times 10^{20} \text{ cm}^{-3}$, with the highest concentrations found near the hillocks. Less scatter in the data was found at a $F_{\text{AsH}_3}/F_{\text{TMGa}}$ of four. The average hole concentration was plotted versus $F_{\text{AsH}_3}/F_{\text{TMGa}}$ at one and four (Fig. 3). Also, room temperature hole mobility was plotted versus the hole concentration (Figure 4). Each data point represents the highest mobility for each of the four runs. Data from the first run at $F_{\text{AsH}_3}/F_{\text{TMGa}}$ of four was not included because the system was not outgassed prior to growth, and the electrical data was atypical. P-type mobility data for GaAs prepared by MOCVD were not available in the literature, so MBE data were used for a comparison. Solid and open data points are characteristic of intentionally and unintentionally doped material, respectively. The dashed line represents the envelope of the highest mobilities of p-type GaAs prepared by vacuum technologies. The extrapolation of the mobility to $450 \text{ cm}^2/\text{Vsec}$ at a hole concentration of 10^{14} cm^{-3} represents the lowest $N_A + N_D$ in p-type GaAs.

Figure 5 and Figure 6 show, respectively, the hole concentration and mobility as a function of temperature for the highest mobility sample prepared at $F_{\text{AsH}_3}/F_{\text{TMGa}}$ of four. These results were obtained from a Van der Pauw sample 7 mm on a square (dashed curve). The sample was then slotted to form a cloverleaf (solid curve). The total concentration of electrically active centers ($N_A + N_D$) from the cloverleaf

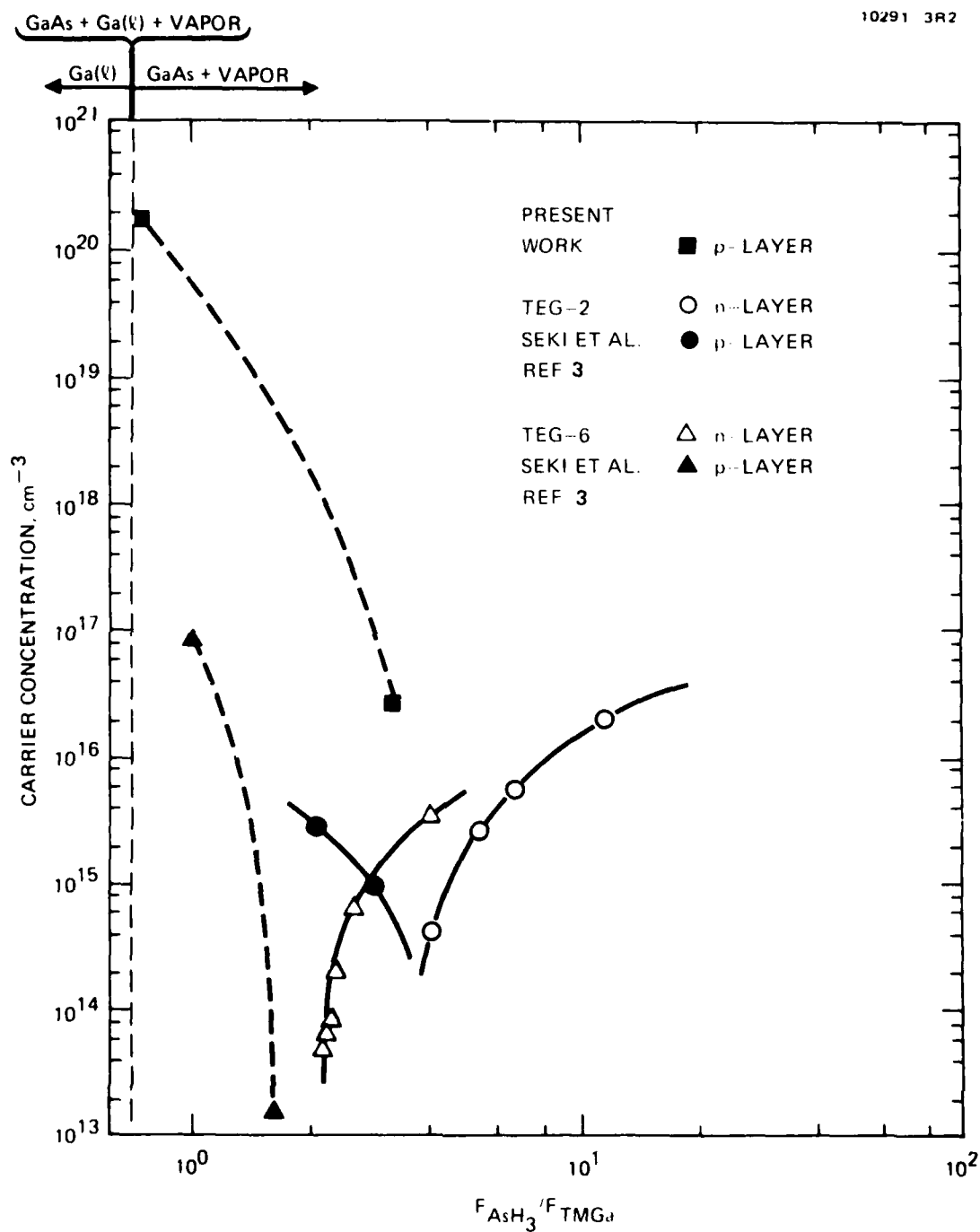


Figure 3. Dependence of type and carrier concentration on mole fraction ratio of Ga and As for GaAs prepared by MOCVD.

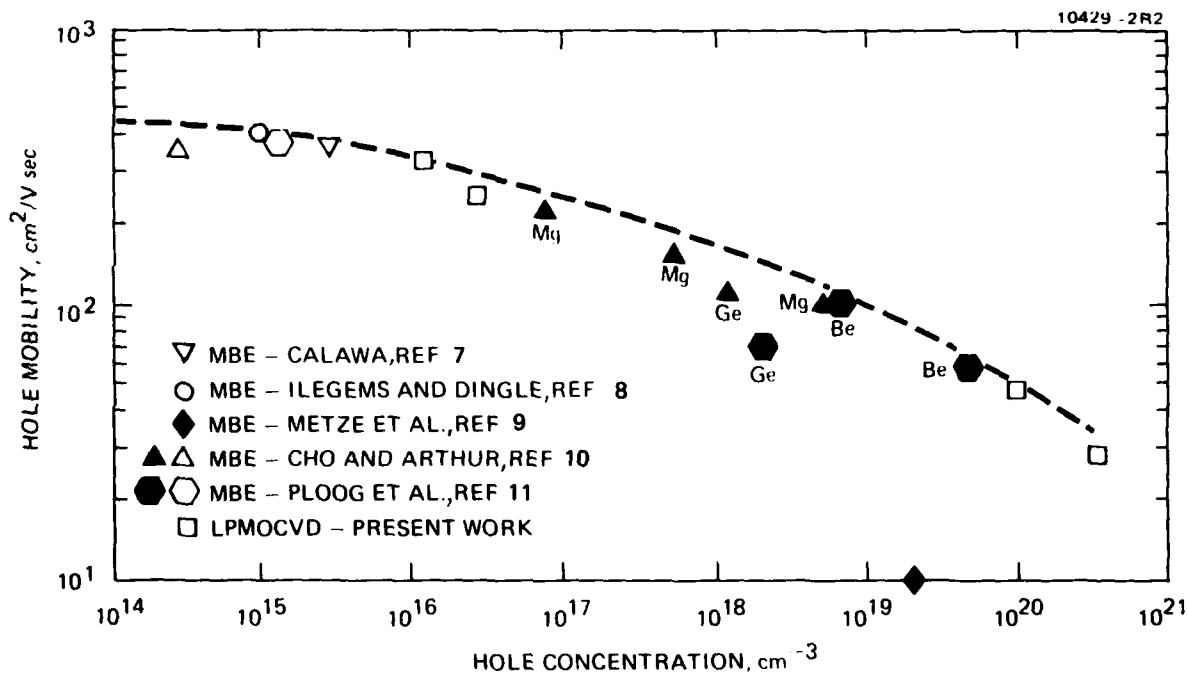


Figure 4. Room temperature hole mobility versus carrier concentration for unintentionally doped (open data points) and intentionally doped (solid data points) GaAs thin films prepared by vacuum technologies. These data and LPE data were used to construct an envelope (dashed line) of nearly uncompensated material.

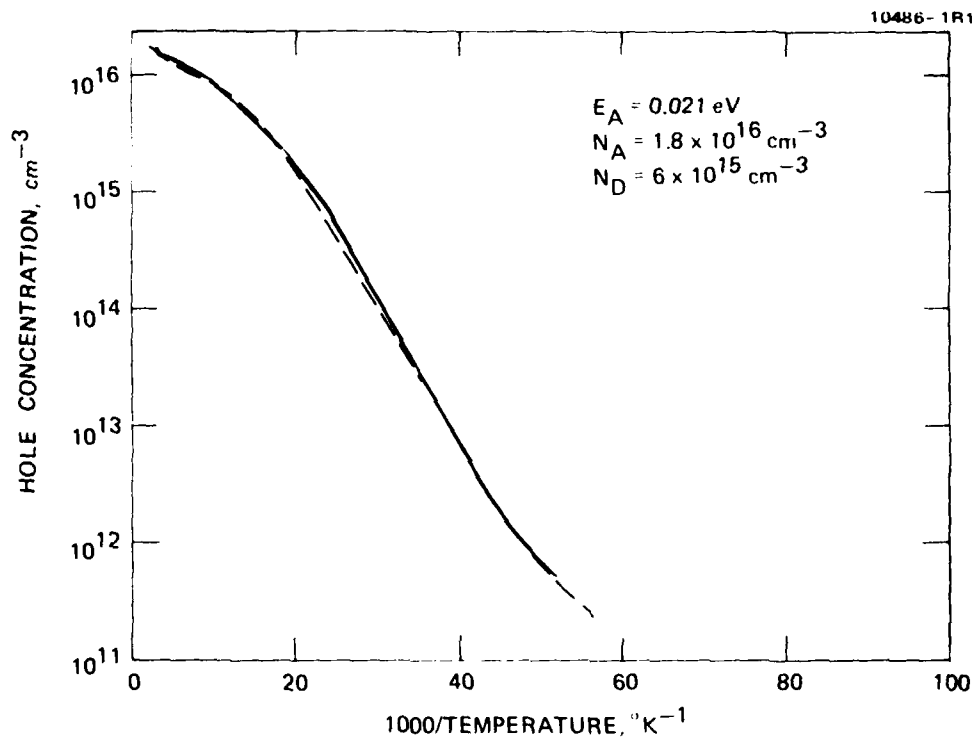


Figure 5. Hole concentration versus reciprocal temperature for square (dashed) and cloverleaf (solid) Van der Pauw samples of GaAs prepared by LPMOCVD at $F_{\text{AsH}_3}/F_{\text{TMGa}}$ of four.

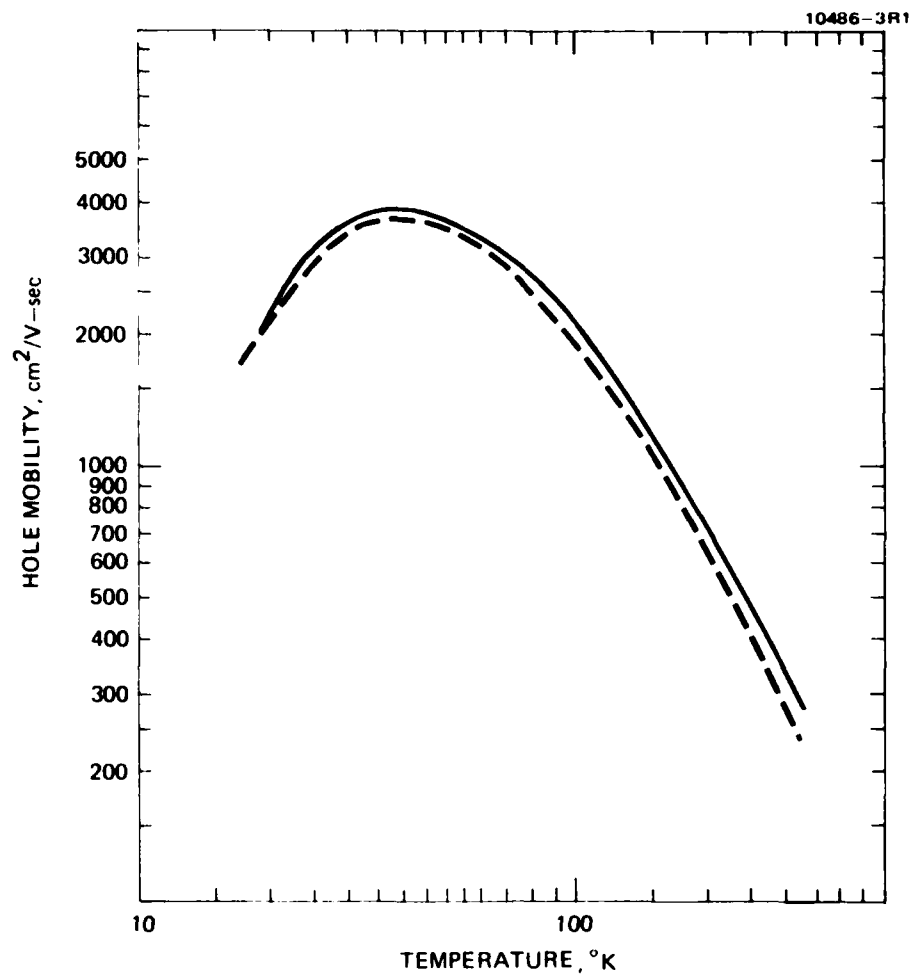


Figure 6. Hole mobility versus temperature for square (dashed) and cloverleaf (solid) Van der Pauw samples of GaAs prepared by LPMOCVD at $F_{\text{AsH}_3}/F_{\text{TMGa}}$ of four.

sample is $2.4 \times 10^{16} \text{ cm}^{-3}$. There is reasonable uniformity across the sample. If we compare the square sample with the cloverleaf sample there is little difference in the shape of the mobility and concentration curves. The electrical measurements sample areas of 40 mm^2 and 10 mm^2 for the square and cloverleaf samples, respectively.

C. IMPURITY ANALYSES

Figure 7 represents typical SIMS data taken at $F_{\text{AsH}_3}/F_{\text{TMGa}}$ of 1. Except for oxygen, there was not a significant difference between either the distributions of various impurities at a second position on the sample, or films prepared in different runs at $F_{\text{AsH}_3}/F_{\text{TMGa}} \approx 1$. The peaks are due either to spikes in the impurity profiles, or differences in the sputtering rate at the interface due to a transition region of different crystalline perfection. The ^1H distribution falls off rapidly from the surface. This is probably an instrumental effect and not characteristic of the sample. The carbon distribution is uniform, with a concentration of about 10^{19} cm^{-3} and well above background. The oxygen profiles vary, with the average concentration being about 10^{18} cm^{-3} . Up to $3 \times 10^{18} \text{ cm}^{-3}$ oxygen was found at the surface. In this particular sample, except for the higher surface concentration, there was no oxygen above the background level of $8 \times 10^{17} \text{ cm}^{-3}$. The mass 32 profiles are similar to the ^{16}O profiles, and most likely are $^{32}\text{O}_2$. The mass 28 profiles correspond to about 10^{16} cm^{-3} Si. This signal is most likely caused by $^{28}\text{N}_2$. Concentrations of other impurities significantly above background were

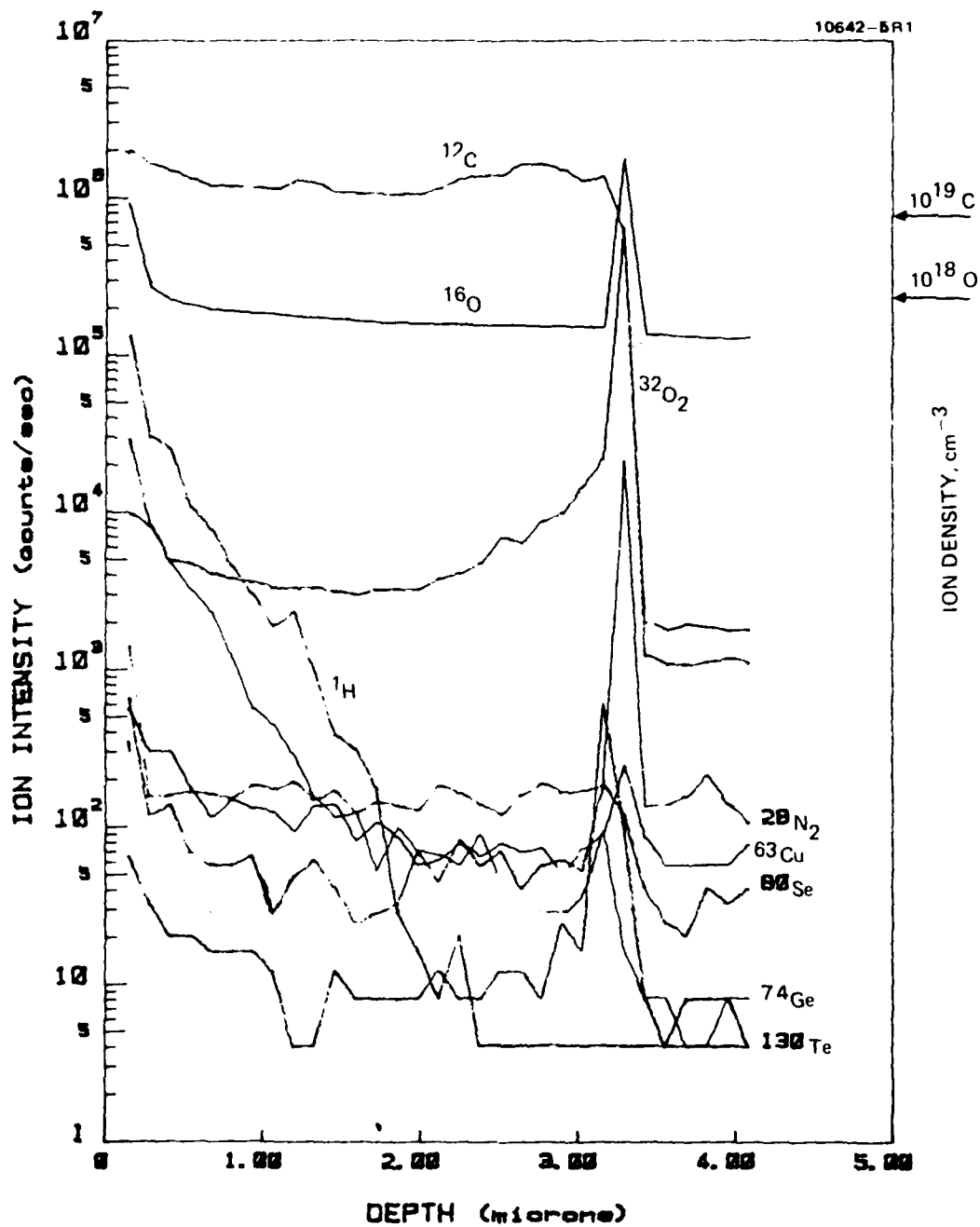


Figure 7. SIMS data taken on the GaAs thin film prepared in Run 1 at $F_{\text{AsH}_3}/F_{\text{TMGa}} \approx 1$.

not apparent. Figure 8 shows SIMS data at $F_{\text{AsH}_3}/F_{\text{TMGa}}$ of four. In this case, the peak in the carbon distribution is real and represents a high concentration of carbon at the interface.

4. DISCUSSION

High concentrations of carbon and oxygen are present in our films and are common in unintentionally doped GaAs films. Figure 9 shows a plot of the carbon and oxygen content of films prepared by MOCVD techniques^{2,3,12} versus N_A+N_D . An n-type VPE sample having a LN_2 mobility of $200,000 \text{ cm}^2/\text{Vsec}$ is included for comparison¹³. Where N_A+N_D was not available, it was estimated from mobility data¹⁴. The type of the material, either n or p, is indicated above each set of data. It is common for most of the oxygen and carbon to be electrically neutral. If all the impurities were active, then the data would lie close to the solid line which represents a one to one correspondence between electrical activity and impurity content. A smooth dashed line is drawn through the carbon data points. The carbon content increases with N_A+N_D and appears to saturate at about 10^{19} cm^{-3} , the assumed solubility limit.

Because the carbon concentration is generally higher than the oxygen concentration, it should be the component which dominates the defect chemistry. For reduced N_A+N_D , the carbon content is significantly higher than N_A+N_D . This is due in part to the uniqueness of the GaAs lattice. GaAs is highly covalent, and the tetrahedral covalent radii¹⁵ of Ga and As are identical. Because the sublattices are nearly equivalent, carbon has little preference for substituting on

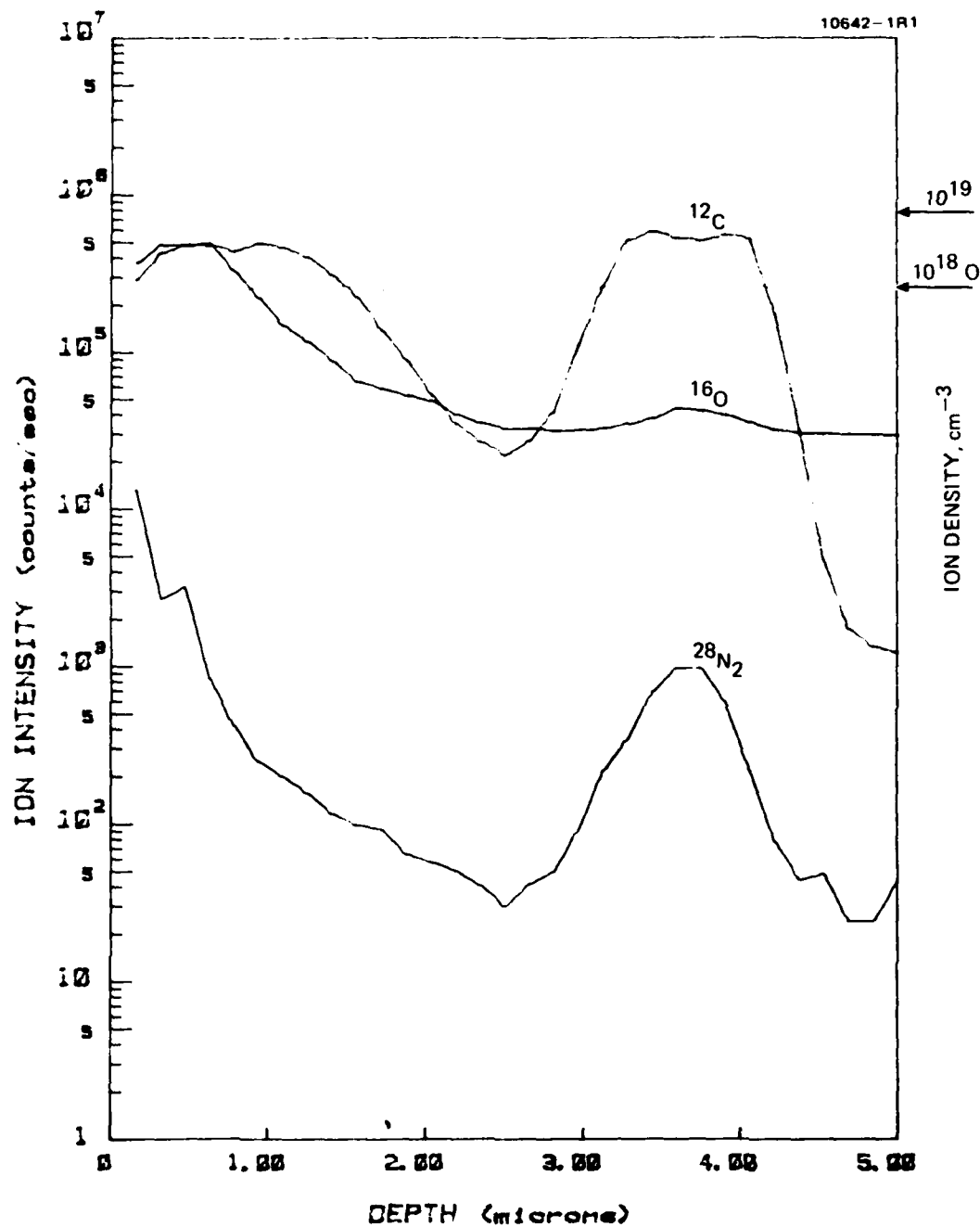


Figure 8. SIMS data taken of the GaAs sample prepared in Run 5 at $F_{\text{AsH}_3}/F_{\text{TMGa}} \approx 4$.

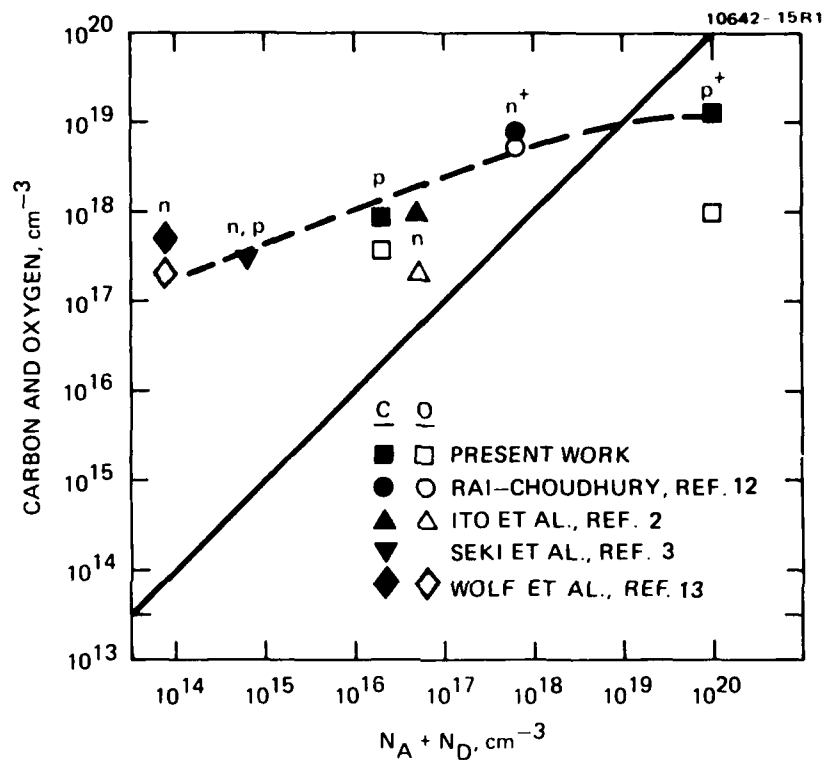


Figure 9. Carbon and oxygen content versus $N_A + N_D$ for GaAs thin films prepared by MOCVD techniques and for a high "purity" film prepared by VPE (Ref. 13).

either Ga sites (C_{Ga}) or As sites (C_{As}). When one of the carbon atoms is incorporated on one of the sublattices as a charged defect, for example C_{Ga}^+ as a donor on the Ga sublattice, an additional carbon atom is attracted to the As sublattice as an oppositely charged acceptor (C_{As}^-) to form the neutral complex (C_{Ga}, C_{As}). This complex should be present in high concentrations because C_{Ga} and C_{As} are oppositely charged, Ga and As sites are nearly equivalent, and C_{Ga} and C_{As} are nearest neighbors.

The carbon concentration is generally up to a factor of ten larger than the oxygen concentration in GaAs^{2,3,12,13}. For our material near the stoichiometric composition it is about a factor of three larger. A fraction of (C_{As}) compensates the oxygen which is presumed to also occupy As sites and form neutral complexes. A very small fraction of the carbon and oxygen atoms remain to form isolated electrically active defects. The concentrations of various native defects make small adjustments to further reduce the concentration of isolated electrically active impurities. The predominant native defects assumed here are the isolated antisite defects, Ga on an As site (Ga_{As}), As on a Ga site (As_{Ga}), and the neutral antistructure complex (Ga_{As}, As_{Ga}).¹⁶ Up to $4 \times 10^{19} \text{ cm}^{-3}$ antistructure defects have been tentatively identified in GaAs.^{17,18} We prefer involving an antisite native defect model rather than a vacancy model because the energy to form an isolated antisite defect¹⁶ ($\approx 1.6 \text{ eV}$) is substantially less than the energy to form a vacancy¹⁹ ($\approx 2.6 \text{ eV}$) in GaAs. The energy to form (Ga_{As}, As_{Ga}) is only 0.70 eV .

As a result of these interactions $N_A + N_D$ will be less than the total carbon and oxygen concentrations. Also, small decreases in the impurity content result in large decreases in $N_A + N_D$. As the impurity concentration decreases, the concentrations of neutral complexes and isolated carbon and oxygen atoms also decrease. As the concentrations of isolated carbon and oxygen atoms approach the equilibrium concentration of native defects, the native defects are more readily able to precisely compensate a greater fraction of the isolated impurity atoms. Because of the formation of neutral complexes, it is not clear as to whether either carbon, oxygen, or other impurities in significantly lower concentrations are the dominant residual acceptors or donors in GaAs. From Hall measurements on our p-type material prepared at a F_{AsH_3}/F_{TMGa} of four (Figure 5) we measured an activation energy of 0.021 eV. This value is similar to that found in unintentionally doped p-type material, and has been associated with carbon.

At large deviations from stoichiometry $N_A + N_D$ is much larger than the impurity concentration. Under these conditions, most of our carbon is probably electrically active and located on As sites. The isolated antisite defect becomes the majority native defect and dominates the electrical properties. Our concentration of antisite defects and holes are about 10^{20} cm^{-3} , and much larger than normally considered. Unusually higher concentration of native defects are possible if (1) we consider the antisite defect with its lower energy of formation rather than the vacancy as the majority native defect, and (2) if our growth process is kinetically limited, resulting in a concentration of native

defects which is significantly higher than expected at thermodynamic equilibrium. In support of our high hole concentrations, Metze et al.⁹ prepared Ga doped MBE material with hole concentrations of $3 \times 10^{20} \text{ cm}^{-3}$. Subsequent to the submission of the abstract, Ploog et al.¹¹ reported mobilities of about $50 \text{ cm}^2/\text{Vsec}$ for Be-doped material having a hole concentration of $5 \times 10^{19} \text{ cm}^{-3}$. The data of Ploog et al. fall near the envelope of high mobility material and lend support to our data. Our crystal perfection is remarkable for such high hole concentrations. Both our films and the films prepared by Metze et al. showed single-crystal channeling patterns when examined by SAD. X-ray Read pictures of our layers generally were composed of rings (polycrystalline material) and spots (single-crystal material). The latter feature may be primarily from the substrate. However, selected regions of our highly degenerate material showed only spots.

Our increase in $N_A + N_D$, with increases in the concentration of carbon and oxygen, is consistent with the amphoteric impurity share model³ in which the amphoteric impurity carbon is shared between Ga and As sites, and the carbon concentration is proportional to the concentration of available vacancies. In our electrical data, and the one atmosphere MOCVD work of Seki et al.³ (Figure 3), the carrier concentration $N_A - N_D$ increases with deviation from the stoichiometric composition. However, there is not a one to one correspondence between the impurity content and either $N_A - N_D$ or $N_A + N_D$, because near the stoichiometric composition a large fraction of the carbon and oxygen is electrically inactive and at extreme deviations from stoichiometry the electrical properties are determined by native defects.

5. SUMMARY

Unintentionally doped p-type films of GaAs were grown by LPMOCVD. Near the Ga-rich three phase boundary the hole concentration was significantly higher than the total concentration of impurities. For more stoichiometric material, the concentration of electrically active impurities was lower than the impurity content. If impurity complexes and antisite defects were considered, a correlation between the impurity concentration and the electrical properties exists. $N_A + N_D$ decreases and "purity" increases with a decrease in the concentration of carbon and oxygen, not directly, but indirectly, presumably because of the more exact formation of neutral complexes. It is important to reduce the total impurity content to decrease $N_A + N_D$ and improve the "purity." However $N_A + N_D$ and "purity" are more dependent on how the impurities are incorporated and their relative concentrations.

The author acknowledges helpful discussions with Dr. R. Wilson, Dr. R. Baron and K. Miller and thanks H. Montano for undertaking the Hall measurements and P. Hoberg for assisting in the assembly of the MOCVD system.

References

1. H.M. Manasevit and W.I. Simpson, J. Electrochem Soc. 116, 1725 (1969).
2. S. Ito, T. Shinohara, and Y. Seki, J. Electrochem. Soc. 120, 1423 (1973).
3. Y. Seki, K. Tanno, K. Iida and E. Ichiki, J. Electrochem, Soc. 122, 1108 (1975).
4. J.P. Duchemin, M. Bonnet, F. Koelsch, and D. Huyghe, J. Electrochem. Soc. 126, 1134 (1979).
5. R.R. Saxena, V. Aebi, C.B. Cooper III, M.J. Ludowise, H.A. Vander Plas B.R. Cairns, T.J. Maloney, D.G. Borden, and P.E. Gregory, J. Appl. Phys. 51, 4501 (1980).
6. J. Katz, N. Bar-Chaim, P.C. Chen, S. Margalit, I. Ury, D. Wilt, M. Yust and A. Yariv, Appl Phys. Lett. 37, 211 (1981).
7. A.R. Calawa, Appl Phys. Lett. 33, 1020 (1978).
8. M. Ilegemes and R. Dingle, Inst. Phys. Conf. Ser. No. 24 (1975) p.1.
9. G. Metze, R. Stall, C. Wood and L. Eastman, Appl. Phys. Lett. 37, 165 (1980).
10. A.Y. Cho and J.R. Arthur, Progress in Solid State Chemistry, Vol. 10, pt. 3, Pergamon Press, 1975, p. 157-191.
11. K. Ploog, A. Fischer and H. Kunzel, J. Electrochem. Soc. 128, 400 (1981).
12. P. Rai-Choudhury, J. Electrochem, Soc. 116, 1745 (1969)
13. C.M. Wolfe, G.E. Stillman and E.B. Owens, J. Electrochem. Soc 117, 129 (1970).
14. G.E. Stillman and C.M. Wolfe, Thin Solid Films, 31, 69 (1976).
15. J.A. Van Vechten and J.C. Phillips, Phys Rev. B, 2, 2160 (1970).
16. J.A. Van Vechten, J. Electrochem. Soc. 122, 423 (1975).
17. B. Goldstein and N. Almelch, Appl Phys. Lett. 2, 130 (1963).
18. J. Blanc, R.H. Bube and L.R. Weisberg, J. Phys Chem Solids. 25, 225 (1964)
19. J.A. Van Vechten, J. Electrochem. Soc., 122, 419 (1975).

APPENDIX F

21st ELECTRONICS MATERIALS CONFERENCE
University of Colorado at Boulder
Boulder, Colorado
June 27 - 29, 1979

ABSTRACT

C-5 (3:35-3:55)

Preparation of InP Thin Film Layers by Planar Reactive Deposition for InP/CdS Solar Cells:* K. Zanio, Hughes Research Laboratories, 3011 Malibu Canyon Road, Malibu, California 90265; L. Fraas, Chevron Research Co., Richmond, California 94802; F. Krajenbrink and L. Hershenson, Hughes Research Laboratories, 3011 Malibu Canyon Road, Malibu, California 90265

Indium phosphide was epitaxially deposited by the planar reactive deposition (PRD) technique onto InP and CdS single crystal substrates. Undoped single crystal thin films of InP deposited on semi-insulating InP substrates in the 320°C to 420°C temperature range are n-type with room temperature mobilities as high as 4062 cm²/Vsec and free electron concentrations as low as 10¹⁴ cm⁻³. Single crystal CdS-on-InP cells were prepared by depositing CdS onto single crystals of commercial p-type InP and onto intermediate micron thick layers of Be-doped p-type InP, the latter deposited earlier onto the commercial InP substrates over the 340°C-400°C range by the PRD approach. The efficiency of the best reference cells and the best cells using the intermediate PRD thin films as the light-absorbing layer were similar, being approximately 10% (Air mass 2 illumination with no anti-reflection coating). Cell efficiency was not found to depend on the temperature of preparation of the intermediate single crystal PRD layer. Studies on the polycrystalline solar cells prepared by the deposition of CdS onto intermediate polycrystalline InP layers showed reduced efficiencies, primarily through a decrease on the open circuit voltage. Approaches in passivating the grain boundaries will be discussed. Interdiffusion limited the deposition of InP on polycrystalline CdS substrates to temperatures below 350°C. The possibilities of preparing an all thin film InP-on-CdS-on-GLASS structure at temperatures below 350°C will also be discussed.

*Supported in part by the Department of Energy

DATE
FILMED
8